Epitaxial Growth and Optical Properties of Mg_3N_2, Zn_3N_2, and alloys

by

Peng Wu
B.Sc., Xinjiang Normal University, 2010
M.Sc., Xinjiang Normal University/University of Science and Technology of China (joint), 2013

A Dissertation Submitted in Partial Fulfillment
of the Requirements for the Degree of

DOCTOR OF PHILOSOPHY

in the Department of Electrical and Computer Engineering

Supervisory Committee

Epitaxial Growth and Physics Properties of Mg_3N_2, Zn_3N_2, and alloys

by

Peng Wu
B.Sc., Xinjiang Normal University, 2010
M.Sc., Xinjiang Normal University/University of Science and Technology of China (joint), 2013

Supervisory Committee

Thomas Tiedje, (Department of Electrical and Computer Engineering)
Supervisor

Reuven Gordon, (Department of Electrical and Computer Engineering)
Departmental Member

Frank Van Veggel, (Department of Chemistry)
Outside Member

Abstract

Supervisory Committee
Thomas Tiedje, (Department of Electrical and Computer Engineering)
Supervisor
Reuven Gordon, (Department of Electrical and Computer Engineering)
Departmental Member
Frank Van Veggel, (Department of Chemistry)
Outside Member

Zinc nitride and magnesium nitride are examples of the relatively unexplored II_3V_2 group of semiconductor materials. These materials have potential applications in the electronics industry due to their excellent optical and electrical properties. This study mainly focuses on the growth and characterization of the new semiconductor materials: zinc nitride, magnesium nitride, and their alloys.

The (100) oriented zinc nitride thin films were grown on both (110) sapphire substrates and (100) MgO substrates by plasma-assisted molecular beam epitaxy (MBE). The typical growth rate is in the range of 0.02-0.06 nm/s, the growth temperature is in the range of 140-180 ^oC, and background nitrogen pressure is around 10^{-5} Torr. The growth process was monitored by in-situ: reflection high energy electron diffraction (RHEED) and optical reflectivity. The RHEED and X-ray diffraction patterns of the zinc nitride indicates that the film is a single crystal material. The in-situ optical reflectivity pattern of the zinc nitride shows interference oscillations, and these oscillations are damped out as the thickness increases. The reflectivity as a function of time was accurately simulated by an optical equation. The optical constants of the thin films, the growth rate, and the thickness were derived from the simulation of the in-situ reflectance. The X-ray diffraction shows that (400) oriented zinc nitride thin films were grown on both A-plane

(110) sapphire substrates and (100) MgO substrates. Optical transmittance measurements were performed on the zinc nitride thin films. The spectrum of the zinc nitride transmittance indicates that zinc nitride has a high optical absorption in the visible light region. The absorption coefficient was calculated from the transmittance spectrum, and the optical band gap of the zinc nitride thin film was found to be 1.25-1.28 eV. Ellipsometry measurements suggested that the refractive index of zinc nitride is 2.3-2.7, and the extinction coefficient is ~0.5-0.7 in the energy range 1.5-3.0 eV. The electron transport measurement shows that the single crystal zinc nitride has a mobility as high as 395 cm^2 /Vs.

A plasma-assisted MBE system was employed for magnesium nitride growth. The growth temperature was in the range of 300-350 ^oC. RHEED and laser reflectivity were employed during growth. The RHEED and X-ray diffraction patterns indicated that the epilayers are single crystal films. The optical laser reflectivity was well fitted by a modified optical equation. The optical constants and growth rate were derived from the simulation. X-ray diffraction showed that (400) oriented single crystal magnesium nitride films were grown on (100) MgO substrates. The optical transmittance spectra show that the magnesium nitride has a high absorption below 500 nm. The calculated absorption coefficient is as high as 4×10^{-4} cm^{-1} in the range of ~2.5-3.0 eV. The optical band gap was estimated to be ~2.5 eV. Ellipsometry measurements showed that the refractive index of the magnesium nitride is 2.3-2.75 and the extinction coefficient is less than 0.3 in the energy range of 1.5-3.0 eV.

Zinc nitride-magnesium nitride ($Zn_{3-3x}Mg_{3x}N_2$) alloys were grown on (100) YSZ substrates by sputtering. The bandgap ranged from 1.2 eV to 2.1 eV for Mg content x in

the 0-0.59 range. One film with a bandgap of ~1.4 eV and Mg content of 0.18 has the relatively high mobility of 47 cm^2 /Vs which was expected for photovoltaics application.

Table of Contents

List of Tables

List of Figures

Acknowledgments

This work would not have been possible without the support from Dr. Thomas Tiedje. He supervised me from the English language to scientific research. Thanks to him for sharing his wisdom and distinguishing logic. Thanks to Dr. Cong Wang for providing me this chance to work with Dr. Tiedje. Thanks to Dr. Reuven Gordon and Dr. Frank van Veggel for serving on my committee. A special thanks to Dr. Naoomi Yamada from Chubu University for his generous help during my research trip in Japan.

I would like to express my deepest gratitude to my parents and my sister whose love, support and encouragement made all this possible.

I am grateful to Dr. Wei Li, Dr. Vahid Bahrami Yekta, and Dr. Mostafa Masnadi-Shirazi for the training and assistance, they provided regarding the various thin film characterization techniques used in this research. I am also grateful to Mohamed Alshal, Mahsa Mahtab, Helaleh Helimohammadi, and Silvia Penkova from MBE lab for their help and friendship during my time at University of Victoria (UVic).

I would like to acknowledge the support from the NSERC and SIAF Graduate Supplement Award of the UVic.

Chapter 1 Introduction

Being different from metals, semiconductor materials have an electrical conductivity value falling between that of a conductor, such as zinc, and an insulator, such as sapphire. Their resistance decreases as the temperature increases. Their conducting property may be altered in useful ways by the deliberate, controlled introduction of impurities into the crystal structure, which lowers its resistance but also permits the creation of semiconductor junctions between differently-doped regions of the extrinsic semiconductor crystal. The behavior of the charge carriers which include electrons and holes at junctions is a basic property of semiconductor materials used in all modern electronics [1].

Those properties make possible numerous technological wonders, including transistors, microchips, solar cells, and light emitting diode (LED) displays. Semiconductors were first used as transistors. Shortly after the first transistor (a point-contact transistor) was made, Shockley invented the more reliable junction transistor, a "sandwich" of two types of germanium (*n* and *p*) produced by adding a small amount of impurities. An integrated circuit (IC) contains many transistors and other devices on a single "chip" of silicon. In 1960, Dawon Kahng and Martin Alalla of Bell labs created the first metal oxide semiconductor (MOS) transistor, and this kind of transistor is widely used today. Meanwhile, some semiconductors respond to light by producing an electric current or becoming able to conduct current. Photovoltaic (solar) cells are used to provide electrical power in remote location, such as satellites, and in combination with storage

batteries for outdoor lighting [2]. Increasingly solar cells are used for electrical power generation.

1.1 Conventional Semiconductors

Semiconductor materials, germanium (Ge) and especially silicon (Si) are widely used in transistors. Si is the preferred material for making transistors; its ability to form a dioxide layer easily as well as made today's integrated circuits possible. Moreover, other semiconductors give off light when electrons and holes recombine. For example, gallium arsenide (GaAs), gallium phosphide (GaP), and aluminum phosphide (AlP) [3][4], which are made into the LEDs used as displays in digital devices. Those same materials can be shaped to form a reflecting cavity that directs the light it produces, creating a semiconductor laser. Semiconductor lasers are often paired with photoelectric cells in automatic doors, burglar alarms, bar-code readers, and fiber-optic communications systems.

Starting from 2000, GaN has become one of the most important semiconductors after Si [5]. It is no wonder that it finds ample application in LED lighting and displays of all kinds, lasers, detectors, and high-power amplifiers. These applications are made possible by the excellent optical and electrical properties of nitride semiconductors. These group III nitrides show variable crystalline structures: the AlN wurtzite, AlN rocksalt, and GaN and InN zincblende [6].

1.2 II_3V_2 Semiconductor

Compared to the ubiquitous and technologically important group III-nitride and II-VI systems, II_3V_2 semiconductors, especially group II nitrides, have received little attention.

General II_3V_2 semiconductors often display interesting transport properties [7][8][9][10]. Furthermore, the II_3V_2 semiconductor materials, (II=Zn, and Cd; V=P, As, and Sb) [7][11][12][13][14][15], were deeply investigated due to the potential applications in long-wavelength optoelectronic devices and solar cells, and that have motivated several recent studies. However, the anti-bixbyite structure II_3V_2 group material has not been deeply studied yet. Mg_3N_2 and Zn_3N_2, which are two of the group II-nitrides semiconductor materials attracted my attention.

1.2.1 Zn_3N_2 and Mg_3N_2

As is well known, magnesium is the ninth most abundant element in the universe. It makes up 13% of the planet's mantle as well as the third most abundant element dissolved in seawater, after sodium and chlorine. Magnesium is the eleventh most abundant element by mass in the human body and is essential to all cells and some 300 enzymes [16][17].

Zinc is an essential mineral perceived by the public today as being of "exceptional biologic and public health importance", especially regarding prenatal and postnatal development. Zinc makes up around 75 ppm of the earth's crust making it the 24th most abundant element [18]. The fact that these are inexpensive and non-toxic elements, is one of my motivations for applying semiconductors made from these elements.

Zn_3N_2 powders were first synthesized by Juza and Hahn [19] in 1940 and have remained relatively unstudied materials for over 50 years. In earlier times, Zn_3N_2 was known only as a black powder. It belongs to the cubic system and has an anti-bixbyite structure with a lattice constant of a=9.7691Å [20]. In 1993, polycrystalline zinc nitride films were prepared by Kuriyama et.al. [21] by direct reaction between ammonia and

zinc evaporated onto quartz substrates with large optical gap of 3.2 eV. Recent studies on Zn_3N_2 films, however, have gradually revealed their properties. To date Zn_3N_2 films have been grown by various methods such as reactive magnetron sputtering [22][23][24], vacuum arc deposition [25], potentiostatic electrolysis [26], metal organic chemical vapor deposition (MOCVD) [27], and molecular beam epitaxy (MBE) [28]. Growth has been performed on several substrates, for example, glass [22], fused quartz [29], amorphous quartz [24], Mo [25], Zn [26], sapphire [30], and GaN [31]. Zn_3N_2 has unique properties which can find wide applications in optoelectronics and nanophotonic areas. Zn_3N_2 has been investigated as a negative electrode in Li-ion batteries in compound form (LiZnN) [32], as material in renewable energy storage processes [33] and for the fabrication of p-type ZnO:N films through oxidation at temperatures up to 700 ◦C [23][27]. Zn_3N_2 has a high electron mobility (100 cm^2 /Vs) at room temperature [22] and high breakdown voltage [34]. However, the bandgap remains controversial (1.06-3.2 eV) [28] which is one of the motivations for research in this material. Furthermore, Zn_3N_2 has potential applications in solar cells, and thin film transistors. Because it is a moisture sensitive material, Núñez et al. used Zn_3N_2 thin films as humidity indicators and perspiration sensors [35].

After the first synthesis of cubic boron nitride [36], Mg_3N_2 is now widely used as a catalyst in the preparation of some nitrides and oxides, such as silicon nitride ceramic, AlN/Al alloys, Group IIIa metal nitrides, MgO nanostructures and p-type ZnO [37][38][39][40][41][42]. Moreover, the magnesium-containing nitrides have various applications such as potential high-temperature materials and substrates [43].

Hydrogen storage materials are being explored internationally as part of the search for future energy systems based on hydrogen fuels cells. Mg_3N_2 is used in combination with lithium-nitrogen or boron compounds for hydrogen storage [44][45][46][47][48][49]. Various combination materials systems, such as $Mg(NH_2)_2$-2LiH [50], LiMg-NH [45][51], and $Mg(NH_2)_2$-MgH_2 [52] can accomplish hydrogen-storage functions in which up to 10 mass % of hydrogen can be stored in the solid state.

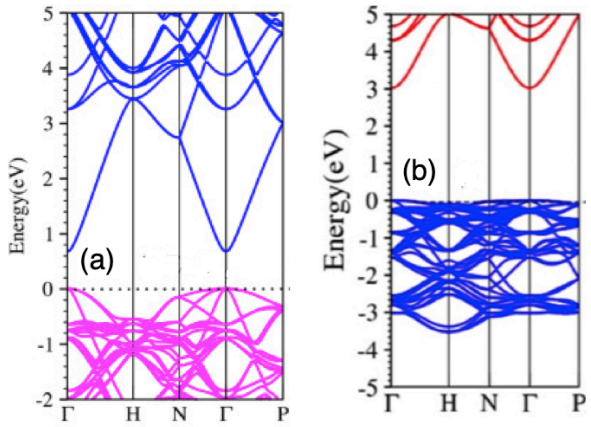

Figure 1-1. Band structures of (a) Zn_3N_2 and (b) Mg_3N_2.

Mg_3N_2 has an anti-bixbyite structure [53]with a direct bandgap of 1.1-2.8 eV from experiment and first-principle calculations [54][55][56]. To obtain reliable information on its features, high quality single crystals of Mg_3N_2 need to be examined. Although the single crystalline Mg_3N_2 nanowires [57] and the further product, Mg_3N_2-Ga, nanoscale semiconductor-liquid metal heterojunction have been investigated [58], unfortunately, single-crystalline Mg_3N_2 could not easily be synthesized, which prevents the scientists from performing precise properties measurements [59] because Mg_3N_2 is moisture

sensitive ($Mg_3N_2+6H_2O\rightarrow 3Mg(OH)_2+2NH_3$) [53]. Hence, high quality Mg_3N_2 thin films need to be grown in order to understand the physical properties of this materials.

Figure 1-1 shows the band structure of Zn_3N_2 and Mg_3N_2. Both materials show the direct bandgap, lager conduction band, and no upper valleys [60][61].

1.2.2 Zn_3N_2-Mg_3N_2 alloys

A direct bandgap semiconductors with a bandgap energy (E_g) of ~1.4 eV is desirable for use in both photovoltaic and photocatalytic energy conversion [62][63]. Among conventional III-V and II-VI binary semiconductors, only the binary compounds GaAs, InP, and CdTe are direct bandgap semiconductors with suitable $E_g \approx 1.4$ eV. Solar cells made from these compounds generally show excellent conversion efficiency. For instance, conversion efficiencies above 27% have been attained in GaAs-based single-junction solar cells [64][65]. For semiconductor alloys, $In_xGa_{1-x}N$ is a candidate material for photovoltaic absorbers because its bandgap is adjustable to 1.4 eV by varying indium content, x [66]. However, these compound semiconductors are composed of rare or toxic elements, and moreover crystal growth generally needs high temperature. These facts make it difficult to produce cost-effective solar cells based on these semiconductors on large-area less expensive substrates like glass. Hence, earth-abundant direct-gap semiconductors with E_g of 1.4 eV that can be grown at low temperature are eagerly anticipated.

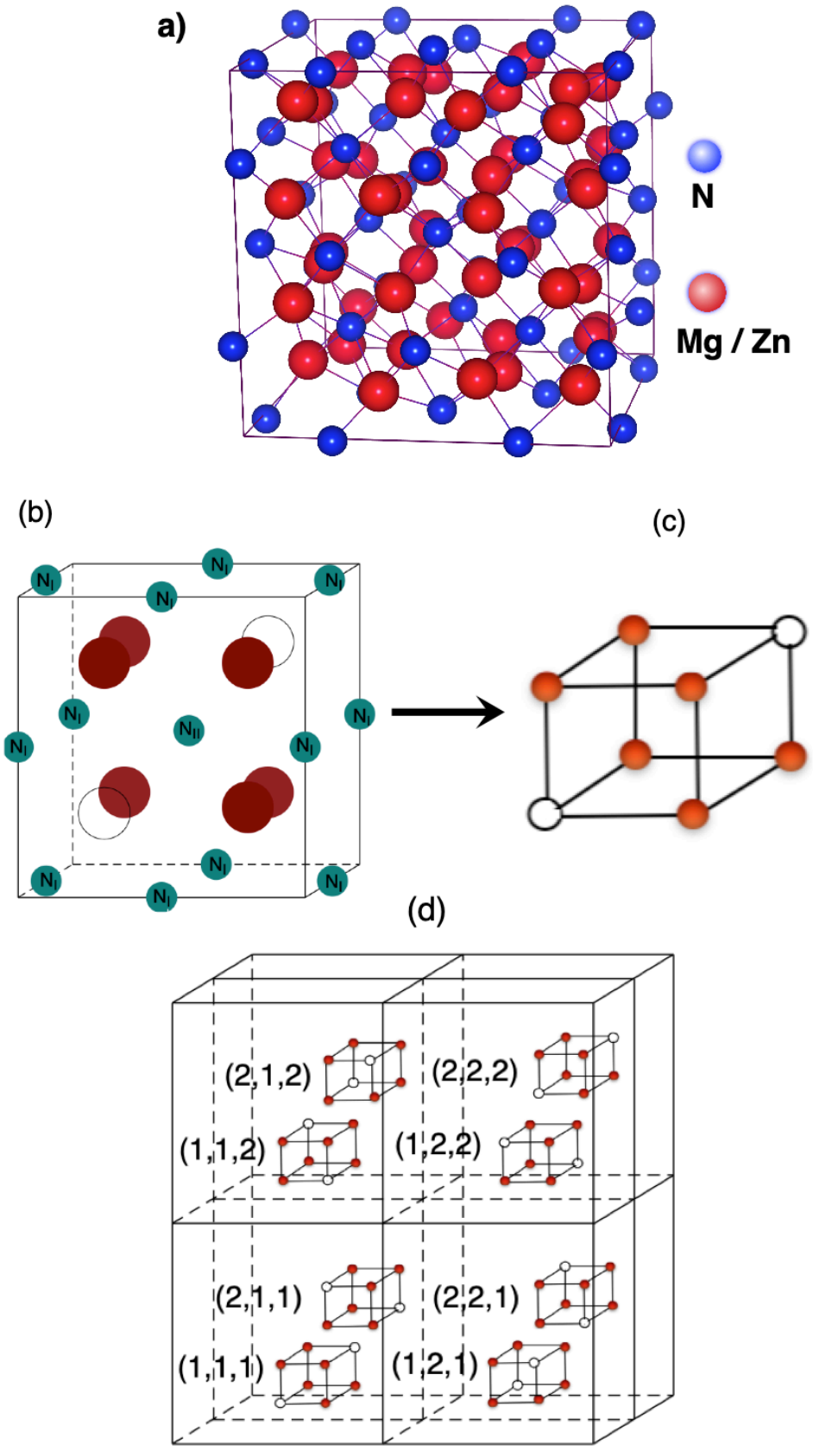
a)
N
Mg / Zn
(b)
(c)
(d)
(2,1,2)
(2,2,2)
(1,1,2)
(1,2,2)
(2,1,1)
(2,2,1)
(1,1,1)
(1,2,1)

Figure 1-2. (a) Crystal structure of Zn_3N_2 and Mg_3N_2 (cubic anti-bixbyite structure). The unit cell includes 48 metal atoms and 32 nitrogen atoms. The lattice parameters are 0.974 nm for Zn_3N_2 and 0.996 nm for Mg_3N_2. The 80 atoms unit cell composed by 8 basis cells. Each basis cell has 6 metal atoms and 4 nitrogen atoms, and these 6 metal atoms have different position configurations. (b) is the example configurations of basis cell. The black circles represent the metal vacancies. (c) is the simplified symbolic cell of (b). (f) shows the 8 basis cells arrangement in an 80 atoms unit cell.

Recent study revealed the intrinsic E_g value of Zn_3N_2 to be 0.8 eV [67], though widely scattered values ranging from 0.9-3.2 eV have been reported so far [68][69][70][71][72][73][74][75][76][77][78]. The scattered E_g values may have originated from oxygen contamination in the oxidation of Zn_3N_2 and carrier-induced blue-shift of E_g [67][79]. Furthermore, Zn_3N_2 shows high electron mobility (>100 $cm^2 V^{-1} s^{-1}$) even in polycrystalline films deposited at low temperature [74][77][79][80][81]. This contrasts sharply with InN, GaN, and $In_xGa_{1-x}N$: electron mobilities in those polycrystalline films are one or more orders of magnitude smaller than those in Zn_3N_2 polycrystalline films [82][83][84]. Therefore, Zn_3N_2 can be an excellent photovoltaic absorber, if the bandgap is close to or can be adjusted to ~1.4 eV. The bandgap engineering of Zn_3N_2 is one of the challenging issues required to be addressed to establish this material as a photovoltaic absorber or variable wavelength light emitter.

Therefore, I propose a novel nitride semiconductor alloy system, Zn_3N_2-Mg_3N_2 ($Zn_{3-3x}Mg_{3x}N_2$), for which the bandgap is adjustable to ~1.4 eV. Zn_3N_2 has a narrow bandgap semiconductor with E_g = 1.25 eV and Mg_3N_2 has been reported to be a direct bandgap

semiconductor with E_g = 2.9 eV [85][86]. Accordingly, the bandgap of $Zn_{3-3x}Mg_{3x}N_2$ can be adjusted to 1.4 eV by varying the Mg content (x). Both Zn_3N_2 and Mg_3N_2 crystals have the cubic anti-bixbyite crystal structure (Figure 1-2): the lattice constants are 0.974 nm for Zn_3N_2 and 0.996nm for Mg_3N_2 [20]. That is, the lattice mismatch is only 2%. Furthermore, the tetrahedral ionic radius of Mg^{2+} (57 pm) is close to that of Zn^{2+} (60 pm) [20]. Hence, good miscibility is expected in this system, and thus the bandgap should be tunable over a wide range. In contrast, $In_xGa_{1-x}N$ with a high In content (for E_g < ~2.5 eV) suffers from a miscibility gap due to the large lattice mismatch between InN and GaN (~10%). The miscibility gap causes fluctuations in the In content across the $In_xGa_{1-x}N$ layers. This makes it difficult to adjust the E_g value of $In_xGa_{1-x}N$ to ~1.4 eV without inhomogeneity and thus to produce highly efficient $In_xGa_{1-x}N$-based solar cells [87]. The expectation above motivated us to grow $Zn_{3-3x}Mg_{3x}N_2$ layers and examine the optical and electronic properties.

1.3 Thin Film Growth Techniques

A thin film is a layer of material ranging from fractions of a nanometer to several micrometers in thickness. Advances in thin film deposition techniques during the 20th century have enabled a wide range of technological breakthroughs in areas such as magnetic recording media, electronic semiconductor devices, LEDs, optical coatings (such as antireflective coatings), hard coatings on cutting tools, and for both energy generation (e.g. thin film solar cells) and storage (thin-film batteries). It is also being applied to pharmaceuticals, via thin-film drug delivery. In addition to their applied interest, thin films play an important role in the development and study of materials with new and unique properties. Examples include multiferroic materials, and superlattices

that allow the study of quantum confinement by creating two-dimensional electron states. Table 1 shows the popular methods for thin film deposition. In this thesis, the Mg_3N_2 and Zn_3N_2 thin films were grown by plasma assisted molecular beam epitaxy (MBE) and the Mg_3N_2-Zn_3N_2 alloy was deposited in a sputtering system. The research details are the subject of subsequent chapters.

Table 1-1. Popular methods for thin film growth.

Methods	Advantages	Disadvantages
Sol-Gel [88]	1. non-vacuum, low-cost, simple and versatile process 2. suitable for glasses or organic-inorganic hybrid materials	thickness limited by cracking during drying stage
Pulsed Laser Deposition (PLD) [89][90]	1. single-crystal films at growth rates up to 25μm/hr with precise thickness control 2. flexible choice of substrate and film material, but best if lattice-matched with similar thermal expansion coefficients. 3. growth temperature much lower than melting point. 4. exact transfer of complicated materials	1. unwanted phases form during growth of biaxial materials (e.g. orthorhombic $Mg_2Si_2O_6$) 2. effect of laser pulse rate on particulate formation depends on target material 3. film choice subject to availability of target sources 4. difficult to create graded composition layers in standard PLD system, prototypes with multiple lasers capable of simultaneous ablation required
Reactive	1. flexible choice of source materials 2. the roughness of the films is very low	1. low growth rate 2. growth rate is affected by target erosion (racetrack depth)

Magnetron Sputtering [22][23][24]	3. uniform films 4. good adhesion of film to substrate 5. the properties of the films are reproducible	3. the performance of sputtering is impeded by the effect of target poisoning. 4. the growth surface is continuously bombarded by electrons and ions, and thus it is highly energetic ion damage
Chemical Vapor Deposition (CVD) [27]	1. can deposit materials which are hard to evaporate, deposition can take place due to a chemical reaction between some reactants on substrate 2. high growth rates possible	1. toxic and corrosive gasses, the by-products need to be volatile 2. high temperature, the chemical reactions need to be thermodynamically predicted to result in a solid film
E-beam Evaporation [91]	1. growth rate can be as high as few micrometers per minute 2. it creates less surface damage 3. a chemical compound can be deposited by e-beam system with multiple sources	1. difficult to be controlled incapable of doing surface cleaning 2. harder to improve the step coverage
Molecular Beam Epitaxy (MBE) [28][30]	1. sophisticated process popular for the growth of single-crystal compound semiconductors 2. oxide MBE used for high-temperature superconductors, multiferroics, wide-bandgap semiconductors, etc. 3. clean environment and high-purity elemental sources lead to highly pure films	1. growth from atomic/molecular beams is slow 2. for overall perfect and pure film, it is necessary to maintain at an ultra-high vacuum (10^{-8}-10^{-10} Torr) 3. the process is expensive

	4. rapid shutter action enables changes to the film at the atomic layer scale and allows for precise thickness control 5. precise composition control over the entire film thickness important for complex multilayer structures such as waveguides with graded index layers or non-uniform doping profiles	

Chapter 2 Plasma Assisted Molecular Beam Epitaxy

MBE growth has the advantage of being capable of making both high quality material and advanced epitaxial structures where two-dimensional (2D) and three-dimensional (3D) confinement takes place; this is witnessed by the fact that most of the new semiconductor structures and devices were demonstrated by MBE.

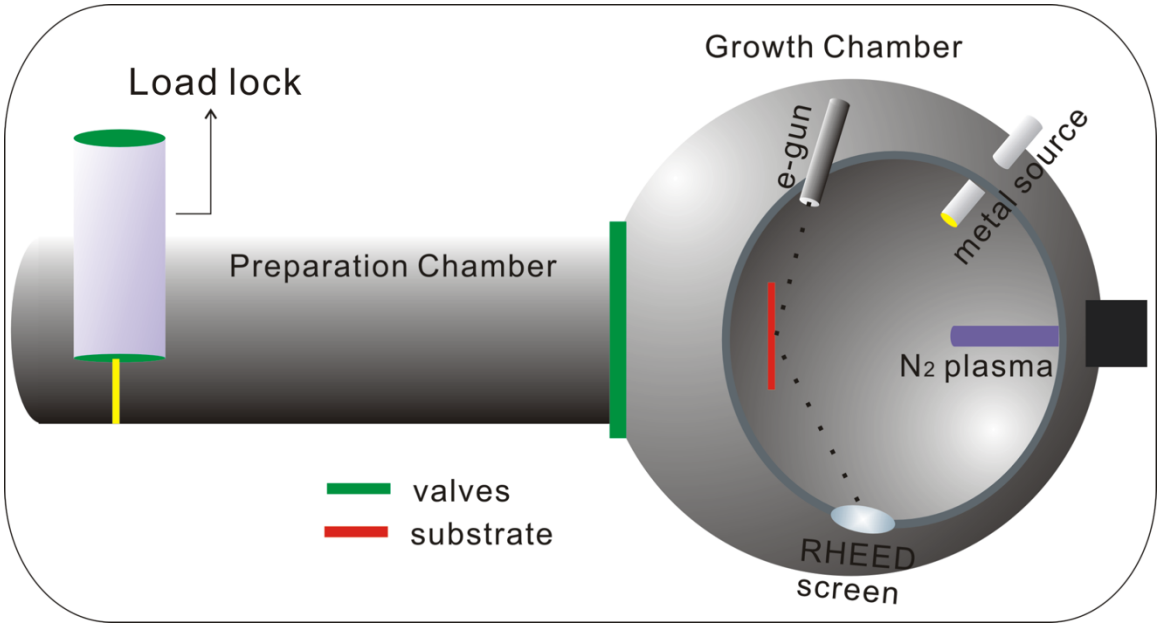

Figure 2-1. Schematic of VG V80 MBE system. Three chambers and a thermal effusion cell for metal are shown, along with a plasma source for nitrogen. An electron gun and fluorescent screen for RHEED are also shown.

2.1 MBE Growth

Many classes of semiconductors, such as II-VI, IV-VI, and IV-IV alloys, have been grown by MBE; however, most of the work has been done on III-V and II-VI

semiconductors where the most interesting results (eg. quantum well and quantum dot) have been obtained [92]. MBE is carried out under ultra-high vacuum (UHV) conditions which are required to minimize the incorporation of contaminants at the growth surface and in the epitaxial layer. Surface contaminants may affect the growth process. The kinetic theory of gases gives the number of atoms impinging on a unit surface area in a unit time at the background pressure *P*, namely $\Phi = P/(2\pi m k_B T)^{1/2}$ molecules cm^{-2} s^{-1}, where *m* is the atomic mass, k_B is Boltzmann's constant, and *T* is the absolute temperature of the gas [93]. Another constraint to the UHV requirement arises from the necessity of growing high-purity materials. Molecular beams are generated by effusion cells by evaporating high-purity materials contained in radiatively-heated crucibles. Figure 2-1 is the Schematic of the VG V80 MBE system. In the growth chamber, the flux per unit surface and time of the molecules or atoms impinging on a substrate placed at a distance *d* from the crucible aperture and perpendicular to the beam is given by $\Phi_{beam} = (AP/\pi d^2)(N_A/(2\pi M k_B T))^{1/2}$, where *P*, N_A, and *M* are the pressure in cells, Avogadro's number, and the molecular weight of the element, respectively. *A* is the cell aperture area, *T* is the absolute temperature. Moreover, the flux generated by real cells depends on a number of parameters of the cells that describe the details of its geometry and on how it is located with respect to the substrate.

2.2 Nitrogen plasma source

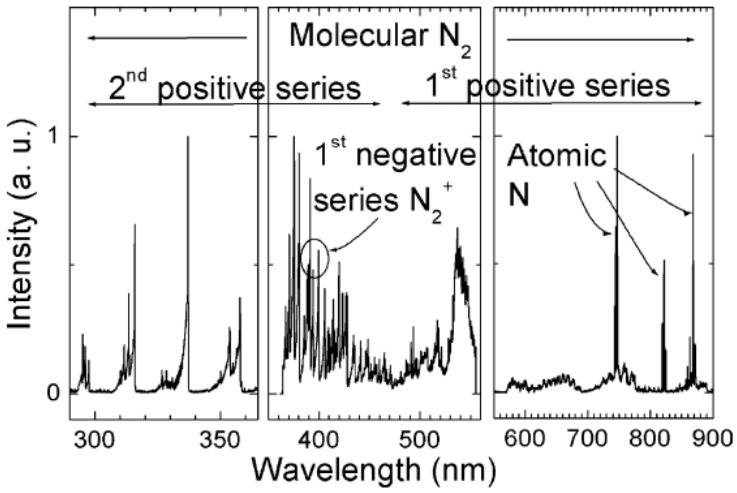

Figure 2-2. Nitrogen plasma emission spectrum in the 300-900 nm range. Each part of the spectrum is normalised to one at its maximum intensity [94].

As the MBE technique became more refined, interest spread from III-V semiconductor films to nanowires and other materials systems, including nitrides. Publications related to nitride MBE started with group III-nitride, especially, GaN. A knowledge of the composition of the nitrogen flux present in an MBE reactor is essential if the source operating conditions are to be optimized and the quality of the grown layers are to be as high as possible. Therefore, in recent years different radio frequency (RF) and electron cyclotron resonance (ECR) plasma sources have been intensively studied across the world.

In this thesis, a RF nitrogen plasma source was employed to grow the thin films. Once the cell temperatures/fluxes were finalized, nitrogen (oxygen may apply for encapsulation at the end of the Mg_3N_2 growth) gas was leaked into the growth chamber through the plasma source. The gas pressure was regulated by an external MKS 244

pressure/flow controller (PFC) positioned along the supply line. A PFC setting of 1 torr would establish a pressure of ~10^{-6} torr in the growth chamber, the drop occurring because of the ~1 mm^2 inlet and outlet orifices of the quartz discharge tube that the gas flowed through. The plasma was ignited by coupling ~300 W into a coil around the discharge tube. Plasma ignition changes the impedance as well as the quality factor of the resonator. Hence, for the ideal growth conditions, I keep forward powers upwards of 300 W and reflected powers < 10 W. The nitrogen plasma within the quartz tube glowed bright purple, as observed at either end of the tube. When the nitrogen flow feeds the RF plasma source, the N_2 molecules are cracked into atomic N and electronically excited N ions. Atom emission lines can be observed in the far visible and near infrared range. They are characterized by three strong emissions at about 745, 821 and 869 nm as shown in the figure 2-2. The strongest one, at 745 nm, is the three-line multiplet (742.4, 744.2 and 746.8 nm) of the ^4P-$^4S^0$ transitions. The first and second positive series of molecular nitrogen can be observed in the 600-900 nm range and 300-500 nm range, respectively. The strongest emission band of the first negative system of N_2^+ ion transitions was observed at 391.4 nm. No signal from N^+ ions was detected [94].

The RF-plasma source produces ionic species are accelerated by electric fields against the growing layer, thereby creating structural defects. Alternative method has been devised that do not involve ions which will induce the crystal damage during film growth, and use ammonia instead [95].

2.3 In-situ Monitoring System

There are two types of in-situ monitoring systems used in this thesis: reflection high energy electron diffraction (RHEED) and laser light scattering.

2.3.1 RHEED

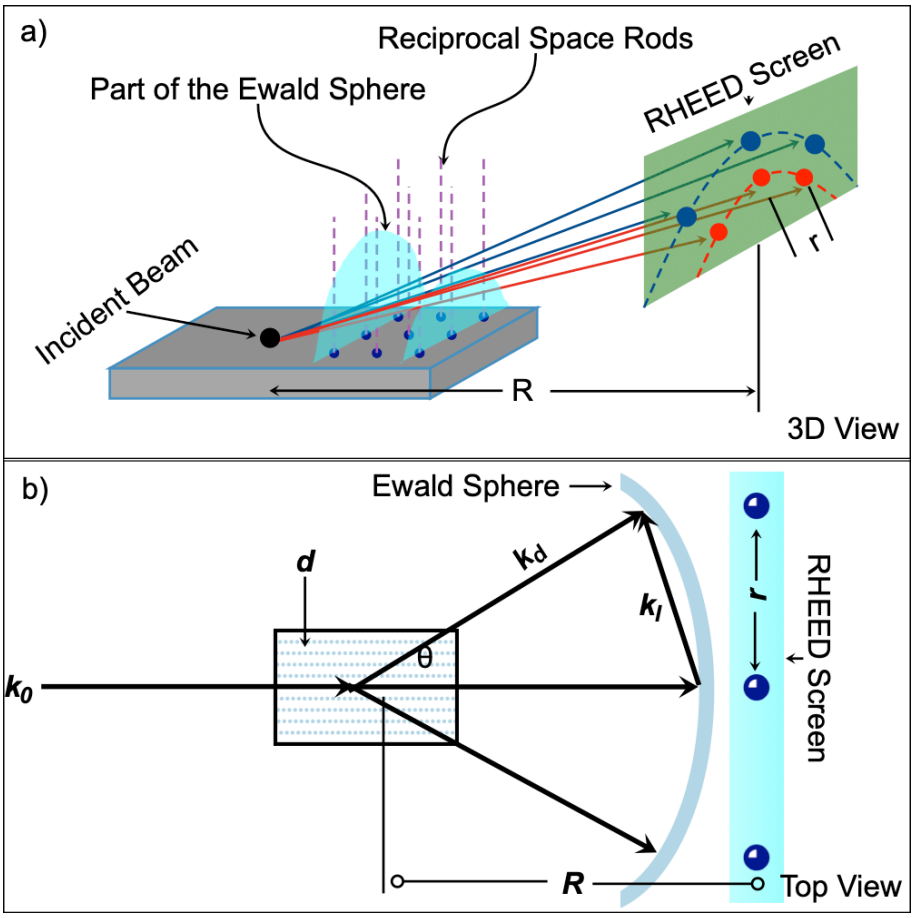

Figure 2-3. (a) 3D view of the electron diffraction geometry showing the effect of the lateral periodicity. (b) The Ewald construction of diffraction in the reciprocal lattice. k_0 and k_d are the wave vectors of the incident and diffracted beams, respectively, and k_l is the scattering vector. Diffraction occurs when a reciprocal lattice rods lies on the circumference of the Ewald circle, which has a radius inversely proportional to the X-ray wavelength.

RHEED is a technique used to characterize the surface of crystalline materials during film growth. This technique involves electrons from a hot filament which are accelerated

in the electron gun and focused on the substrate at a glancing angle of less than 3°, and the detected angle. Only the atoms on the surface of the substrate/film contribute to the RHEED pattern. Those incoming electrons are scattered from the atoms of the film surface and strike a fluorescent screen producing diffraction patterns (at detected angle of 12°) visible outside the MBE chamber. In the UVic MBE system, the photographs of the RHEED patterns were captured by a camera. Atoms at the sample surface diffract (scatter) the incident electrons due to the wavelike properties of electrons. The system was typically operated at 16 keV, and generating an electron wavelength of 0.078 nm known as the de Broglie wavelength [96]:

$$\lambda = \frac{h}{2m_0 eV}\left[\frac{1}{\sqrt{1+\frac{eV}{2m_0c^2}}}\right] \tag{2-1}$$

where c is speed of light, h is Planck's constant, m_0 is the electron rest mass, e is the elementary charge, and V is the voltage. The diffraction pattern at the screen relates to the Ewald sphere geometry. Being different from the bulk crystal diffraction, RHEED probes the crystal structure in the lateral direction (see figure 2-3). The Ewald sphere is centered on the surface of the sample with a radius equal to the reciprocal of the electron wavelength: $k_0=2\pi/\lambda$. So the Ewald's sphere can be constructed by

$$\vec{k}_l + \vec{k}_0 = \vec{k}_d \tag{2-2},$$

where $k_l = 2\pi / d$, d is the plane spacing, and $k_0 = k_d = 2\pi / \lambda$ are equal to the Ewald sphere radius. In figure 2-3 (b), since the Ewald sphere radius is much larger that the k_l, θ is very small and k_l is essentially $\perp k_0$, the relation between the plane spacing d of the reciprocal lattice rods and the spacing r of the RHEED streaks observed on the screen is given by

$$\sin\theta \approx \frac{k_l}{k_0} \approx \frac{r}{R} = \frac{\lambda}{d} \qquad (2\text{-}3),$$

where r is the lateral separation of the diffraction spots seen on the screen and R is the sample to screen distance.

The RHEED patterns differ depending on the sample orientation and the crystalline surface. With a well-ordered sample surface, the reflected electrons from a diffraction pattern consisting of bright spots and/or streaks observable on the fluorescent screen (in figure 2-4). Theoretically, the intersection of the reciprocal lattice with the Ewald sphere should form points. However, when the surface is composed of small domains whose size is smaller than the coherence length (the coherence length is determined by how monochromatic the energy of the electron beam is and how parallel the beam is) of the electron beam, the reciprocal rods are broader, and the width of the reciprocal rods is inversely proportional to the average size of the domains. Then, the intersections between the Ewald sphere and the reciprocal rods become large ellipses, resulting in elongated and broader diffraction spots(streaks) in the RHEED pattern.

However, RHEED required a high vacuum $<10^{-7}$ Torr, it is the challenge for RHEED working at the gas ambient growth condition as exists in plasma assisted MBE.

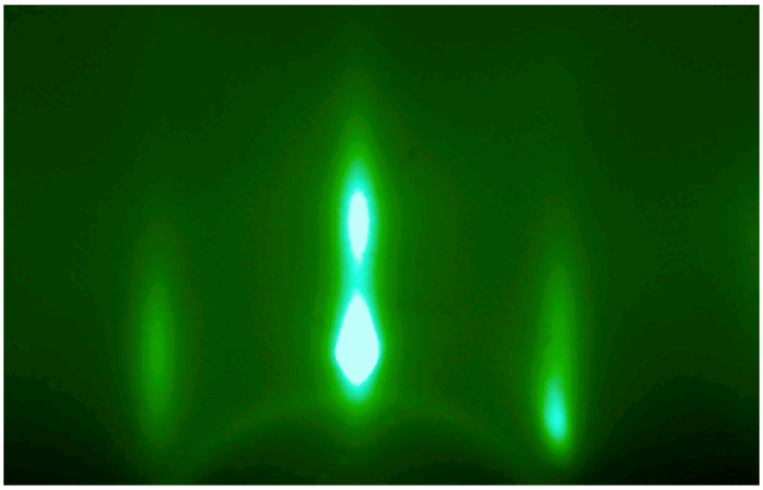

Figure 2-4. RHEED diffraction patterns of a smooth (100) oriented Mg_3N_2 surface under good conditions of diffraction.

2.3.2. Laser Light scattering

In contrast to RHEED, laser light scattering is equally effective in gas ambient or in vacuum, and relatively inexpensive.

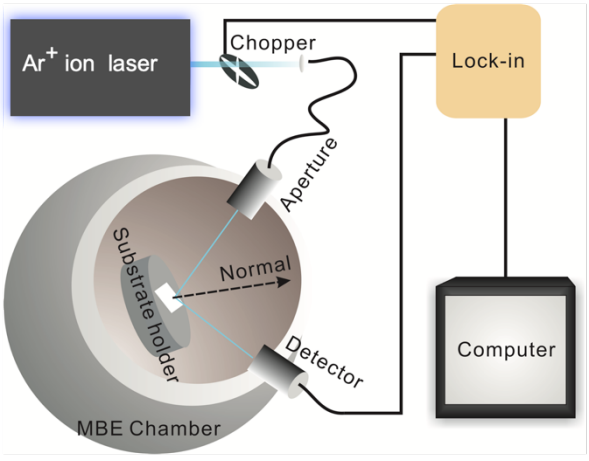

Figure 2-5. Schematic of the in-situ laser light scattering setup.

In figure 2-5, the mechanically chopped 488 nm line of an Ar^+ ion laser was used in the light scattering apparatus. During growth, the laser light passes through the fiber and is incident on the sample through a windowed source port θ=36.5° off the normal. The intensity of the specular reflection oscillates with the thickness of the deposited layer following the principle of thin film interference, which in this case applies to the optical contrast between the film and substrate. Detection was done at a symmetrically-opposing window port with a UV-enhanced Si photodiode (sensitive from 250-1100 nm) behind a laser line filter. The mechanically chopped laser allowed for the detection of the reflected signal by an SRS 830 lock-in-amplifier. In order to restrict the specular reflection signal to the multilayer comprising the film and film-substrate interface, single-side-polished substrates were used. Thin film interference oscillations in the specular reflectivity provide a convenient measure of the film thickness with an oscillation period, η:

$$\eta = \frac{\lambda}{2n\,cos\,(\theta_1)} \qquad \text{(2-4a)},$$

where θ_1 is the angle with respect to the normal of the beam inside the film, n is the refractive index, and λ is the laser wavelength. Substituting the equation (2-4a) with Snell's law, $\frac{sin(\theta_1)}{sin(\theta_0)} = \frac{1}{n}$, where θ_0 is the angle of incidence of the laser beam on the film, the oscillation period can be written as

$$\eta = \frac{\lambda}{2n\,cos\left[\arcsin\left(\frac{\sin\theta_0}{n}\right)\right]} \qquad \text{(2-4b)}.$$

Figure 2-6 is an example of reflectivity oscillations of a ZnO film during growth. The oscillation period of the ZnO film $\eta \approx 124$ nm (the thickness of the ZnO film was found to be ~248 nm), was well predicted by using the following parameters: $\lambda = 488$ nm, $\theta = 36.5^{o}$, and $n = 2.06$.

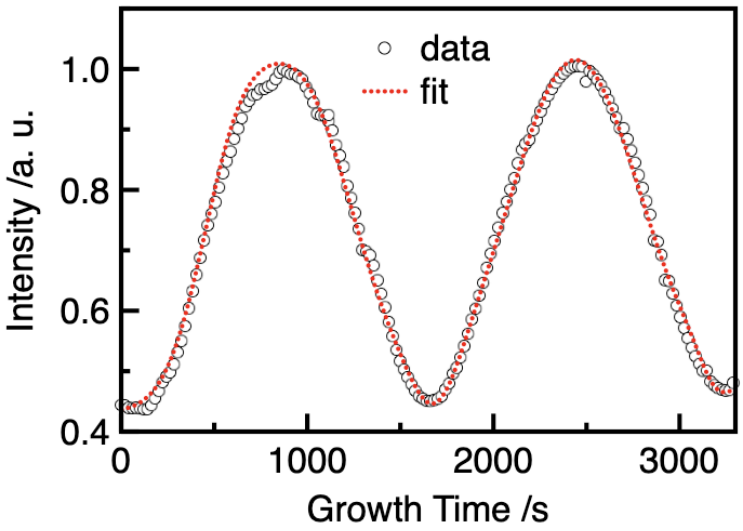

Figure 2-6. In-situ specular reflectivity at 488 nm of a ZnO film during growth. The calculated reflectivity (red dots) is the best fit to the experimental spectrum (black circles) as discussed in the text.

In addition to the thickness prediction, the in-situ laser reflectivity as a function of time can also provide the optical constants $\tilde{n}$ and growth rate g from a theoretical model of the reflectivity.

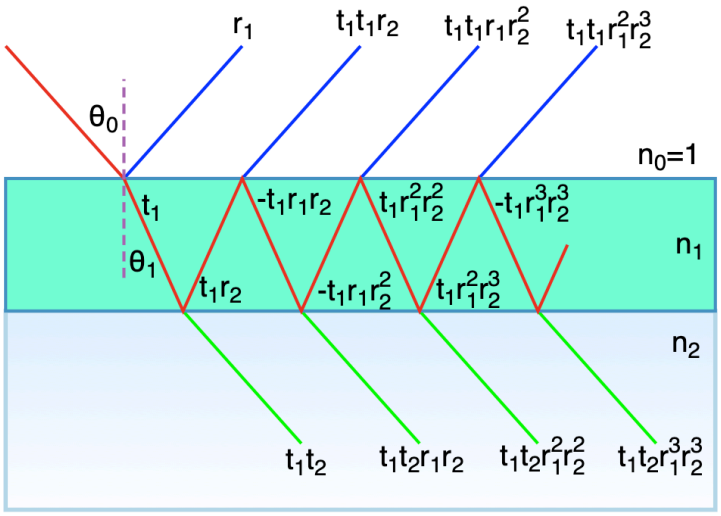

Figure 2-7. Schematic showing the multiple beam interference when growing an epilayer with optical properties different from the underlying substrate.

Figure 2-7 shows the light paths in the growing film. By using the notation of vacuum = 0, film = 1 and substrate = 2, the change in phase of the beam on traversing the film was given by [97]

$$\Delta = \frac{2\pi}{\lambda}\tilde{n}_1 d\, cos\theta_1 \qquad (2\text{-}5),$$

where $d = gt$ is the thickness of the film. If the film is absorbing, or if it is bounded by absorbing media, then the value of n_1 is replaced by the corresponding complex quantities $\tilde{n}_1 = n_1 + ik_1$, where k_1 represents the energy absorption. Considering Snell's Law: $n_0 sin\theta_0 = n_1 sin\theta_1$, equation (2-5) can be written as

$$\Delta = \frac{2\pi}{\lambda} n_1 gt \left[1 - \left(\frac{sin\theta_0}{n_1}\right)^2\right]^{1/2} - i\frac{2\pi}{\lambda} k_1 gt \left[1 - \left(\frac{sin\theta_0}{n_1}\right)^2\right]^{1/2} \qquad (2\text{-}6),$$

and the real part and the imaginary part can be expressed as

$$\delta(t) = \frac{2\pi}{\lambda} n_1 g t \left[1 - \left(\frac{sin\theta_0}{n_1}\right)^2\right]^{1/2} \text{ and } \alpha(t) = \frac{2\pi}{\lambda} k_1 g t \left[1 - \left(\frac{sin\theta_0}{n_1}\right)^2\right]^{1/2} \quad (2\text{-}7),$$

respectively. The reflected amplitude is given by the sum of the terms in figure 2-7 (more detail in reference [97][98])

$$R = \frac{r_1 + r_2 e^{-i2\delta(t)} e^{-2\alpha(t)}}{1 + r_1 r_2 e^{-i2\delta(t)} e^{-2\alpha(t)}} \quad (2\text{-}8).$$

Thus, the reflectivity of the laser scattering system as a function of the growth time is given by

$$\mathcal{R}(t) = RR^* = \frac{r_1^2 + r_2^2 e^{-4\alpha(t)} + 2r_1 r_2 e^{-2\alpha(t)} \cos(2\delta(t))}{1 + r_1^2 r_2^2 e^{-4\alpha(t)} + 2r_1 r_2 e^{-2\alpha(t)} \cos(2\delta(t))} \quad (2\text{-}9),$$

where $r_1 = \frac{n_0 - n_1}{n_0 + n_1} = \frac{1 - n_1}{1 + n_1}$, and $r_2 = \frac{n_1 - n_2}{n_1 + n_2}$ are the Fresnel coefficients. Figure 2-6 is the reflectivity simulation of ZnO film growth with equation (2-9). The experimental data (blue circle) was well simulated by equation (2-9) with the growth rate g = 0.075 nm/s, and index of refraction $\tilde{n}_1$ = 2.04 + 0.01i. $n_1 = 2.04$ is close to the 2.05 in reference [99]. Furthermore, the film's thickness d can be calculated by $d = gt$, where t is growth time.

2.4 Effusion cell

Molecular beams are generally produced by thermal evaporation of suitable materials from effusion cells which are among the most critical components of an MBE growth chamber. The design and manufacture of MBE effusion cells must fulfill some basic conditions such as high purity, good time stability, and the highest uniformity attainable over the whole substrate area. The cell assembly is mounted on a UHV flange with feedthroughs for electrical connections. Remotely controlled mechanical shutters located inside the growth chamber in front of each cell operate as on/off switches for beam fluxes with typical actuation times of tenths of seconds. Closed-loop control systems enable both to achieve stable operating cell temperatures, and then, beam fluxes, or to accurately drive rapid temperature changes, required for the growth of structures consisting of semiconductors with complex composition or doping profiles along the growth direction. In the VG V80 system, two effusion cells were used for the evaporation of Zn and Mg. Molecular beams are provided by evaporating or sublimating source materials in high-purity crucibles of pyrolytic boron nitride (PBN), radiatively-heated by Ta heaters. Radiation shields surrounding the crucible are used to improve the heating efficiency and to minimize the thermal cross-talk between adjacent cells, which can be relevant for cells operating at very different temperatures. The temperature of the cells determines the flux of molecular beams and is accurately measured by a thermocouple (TC) in direct contact with the crucible; the TC provides the feedback signal to the temperature controller for the power supply regulation [100]. Once a cell reached a suitably high temperature, further adjustments were made using measurements of the elemental flux by a quartz crystal microbalance as feedback.

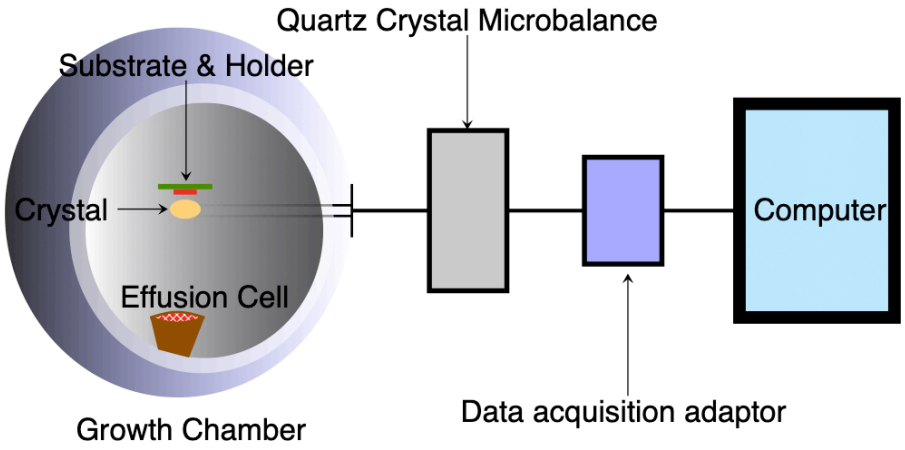

Figure 2-8. Schematic of the quartz crystal microbalance system in growth chamber.

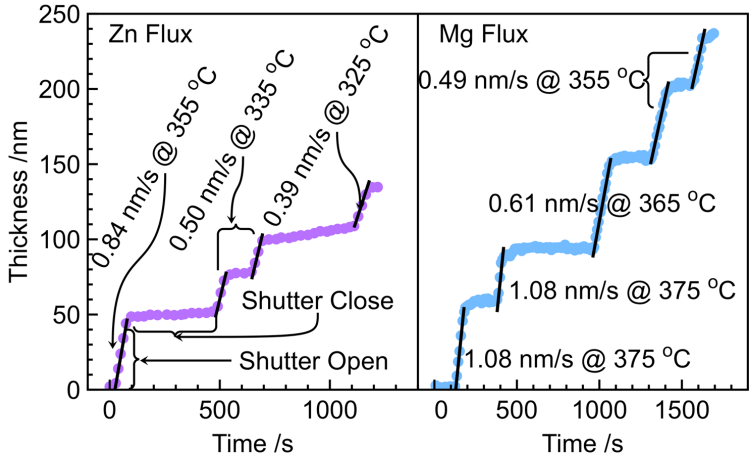

Figure 2-9. Deposition rate of Zn and Mg metal onto a QCM placed in front of the substrate at various cell temperatures. The growth rate was calculated from the slope.

The quartz crystal microbalance (QCM) system in figure 2-8 is employed for measuring the metal flux. The sensor is a retractable quartz crystal whose resonant frequency depends on the amount of mass deposited on it. The QCM system converts its internal measurement of mass to a thickness based on the elemental density input by the

user (ρ_{Zn} = 7.14 g/cm^3, ρ_{Mg} = 1.74 g/cm^3). This QCM deposition rate was calculated from the slope of the measured thickness over a few minutes which is shown in figure 2-9 and is proportional to the elemental flux.

Figure 2-10 shows the metal flux as the function of the temperature of the effusion cells. As expected, higher cell temperatures produce higher fluxes, as demonstrated by the Zn and Mg cells in the figure. The straight lines in figure 2-10 (b) are fits to the measured temperature dependence of the fluxes. The fits have the form $Flux = A\ exp(-B/kT)$ and the fitting parameters (A, B) are (8.5×10^{17} nm/s, 2.3 eV) and (1.3×10^{15} nm/s, 1.9 eV) for the Mg and Zn sources, respectively. The flux approximately doubles with each 10 °C and 12 °C increase in the effusion cell temperature for Mg and Zn respectively. Both Zn and Mg are evaporated below the melting point. The melting points are 420°C and 650°C for Zn and Mg, respectively [101].

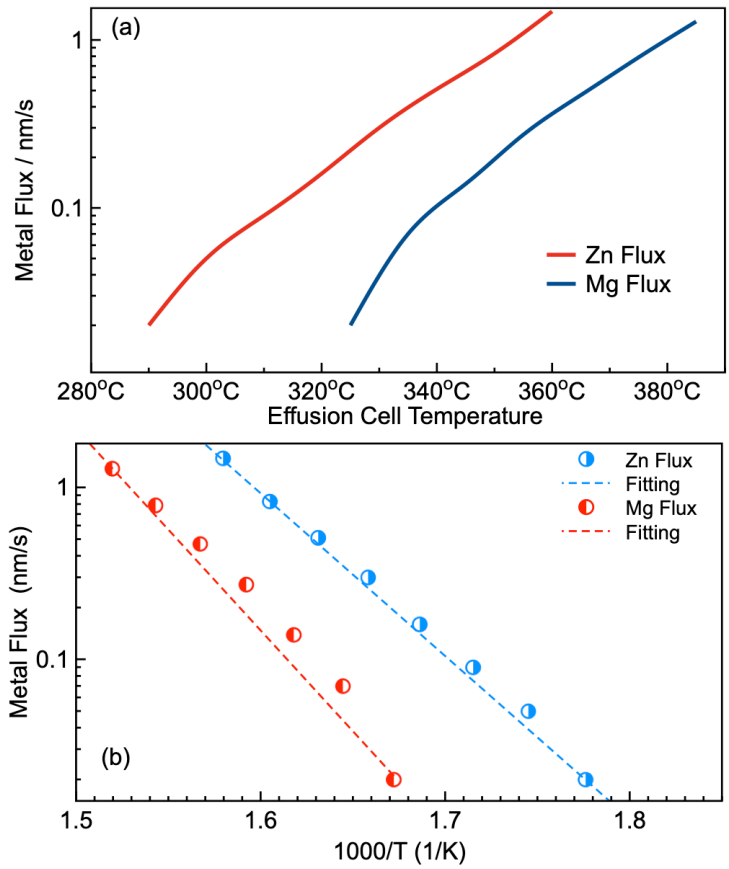

Figure 2-10. The metal flux as a function of the effusion cell temperature (a and b). (b) The dashed lines are fits to the temperature dependence of the metal fluxes using an Arrhenius relation as discussed in the text.

2.5 Electron Beam Evaporation

In addition to the MBE system, an electron beam evaporation system was used for growth of the radiation absorbing layer on the sapphire substrates and for Mg_3N_2 thin film encapsulation. For the purpose of good thermal contact during the MBE growth, I usually deposited 100nm Cr and 200 nm Mo on the back of the sapphire substrate. This type of thermal layer is easy to remove with sandpaper before optical measurements. As shown in figure 2-11, the electron beam is given off by a hot tungsten filament and then

accelerated by a high voltage. The electron beam is directed by the magnetic field and then incident on the target material in the crucible. The target material is bombarded with the electron beam which heats it to a high temperature and causes atoms from the target to transform into the gaseous phase. These atoms then precipitate into solid form on contact with a surface, coating everything in the vacuum chamber in line of sight with a thin layer of the anode material [102]. The thickness of the thermal layer and capping layer were measured with a QCM.

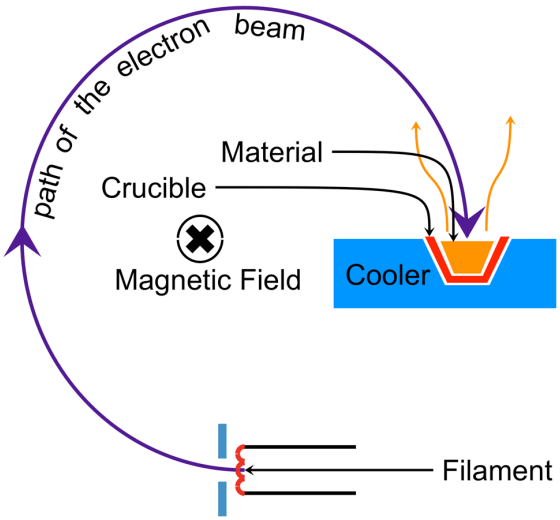

Figure 2-11. Schematic of the electron beam evaporation system.

2.6 Reactive Magnetron Sputtering

Reactive magnetron sputtering has emerged as an attractive method for thin film deposition [103]. In this thesis, I used a sputtering system to deposit Zn_3N_2-Mg_3N_2 alloys for the purpose of the bandgap tuning engineering. Figure 2-12 is a schematic of the co-

sputtering system. By applying a voltage at a frequency of 13.56 MHz, ions gain sufficient energy in the electric field to break down the Ar/N_2 gas mixture and bombard the target with sufficient energy to initiate sputtering. To obtain sputtering as a useful coating process a number of criteria must be met. Firstly, ions of sufficient energy must be created and directed towards the surface of a target to eject atoms from the material. Secondly, ejected atoms must be able to move freely towards the object to be coated with little impedance to their movement. These criteria can be accomplished in vacuum system: low pressures are required to maintain high ion energies and to prevent too many atom-gas collisions after ejection from the target. The concept of the mean free path (MFP) is useful here. This is the average distance that atoms can travel without colliding with another gas atom. The magnetron source immerses the cathode surface in a magnetic field such that electrons are confined by the $\boldsymbol{E} \times \boldsymbol{B}$ drift currents close to the cathode. In essence, the operation of a magnetron source relies on the fact that primary and secondary electrons are trapped in a localized region close to the cathode into an endless 'racetrack'. In this manner, their chance of experiencing an ionizing collision with a gas atom is vastly increased and so the ionization efficiency is increased too. This causes the impedance of the plasma to drop and the magnetron source operates at much lower RF power. This greater ionization efficiency leads directly to an increase in ion current density onto the target which is proportional to the erosion rate of the target. The growth rate was controlled by regulating the RF power on the target [104].

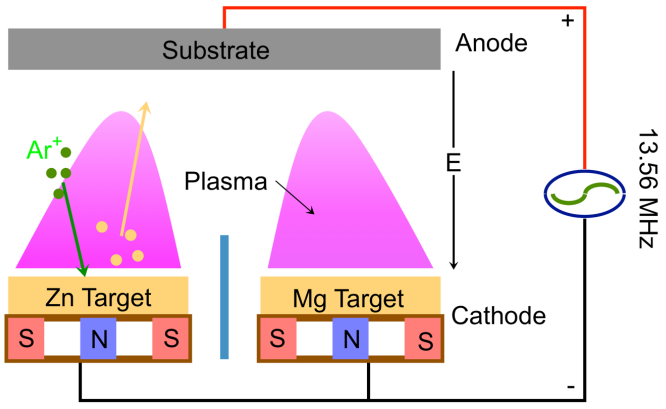

Figure 2-12. Schematic of the co-sputtering system.

Table 2-1. Source material purity.

Materials		Purity
Zn	MBE	99.9999%
	Sputtering	99.99%
Mg	MBE	99.9999%
	Sputtering	99.99%
N_2	MBE	99.9995%
	Sputtering	99.9995%
Ar	MBE	N/A
	Sputtering	99.9999%

2.7 Sources

The high purity metal sources (table 2-1) were employed for both MBE and sputtering growth. Commercial Zn and Mg shot were purchased from Alfa Aesar. A variety of substrates, (100) MgO, (100) YSZ and c-plane sapphire which are good for

optical measurements, were obtained from several vendors and on receipt were annealed at 1000°C for 9 hours in air. The substrates were placed on a sapphire wafer before being loaded into a tube furnace for annealing. Annealing sapphire is known to produce an ordered surface with atomic steps on the surface [105]. Figure 2-13 shows the crystal structure of the substrates. Table 2-2 summarizes the physical properties of the substrates, I used for epitaxial thin film growth.

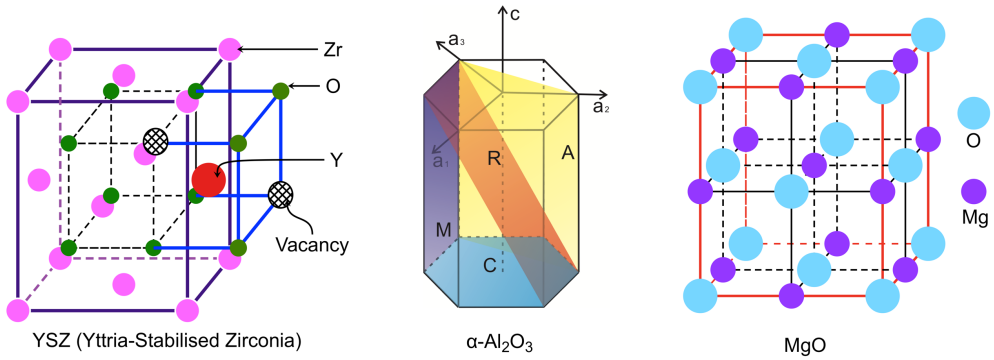

Figure 2-13. The crystal structure of the three substrates: YSZ, α-Al_3O_2, and MgO (from left to right).

Table 2-2. Substrates used in thin film growth.

Substrates	YSZ	MgO	α-Al_2O_3
Crystal Structure	Fluorite	Rocksalt	Corundum
Lattice Constant	a = 0.512 nm	a = 0.421 nm	a = 0.479, b = 1.299nm
Optical Bandgap	5.6 eV	7.8 eV	9 eV
Refractive Index @488 nm	2.182	1.747	1.775
Weight Percentage	Zirconium: 68.1 % Yttrium: 3.2 % Oxygen: 28.7 %	___	___

2.8 X-ray Diffraction

After growing the sample in the MBE with all the in-situ monitoring, the sample optical, structural and electrical properties can be investigated with ex-situ measurement techniques. The crystal structure of the films was analyzed post-growth by high-resolution x-ray diffraction (XRD) using a Bruker D8 Discover Diffractometer with ACC Ge004 monochromator. X-rays are electromagnetic radiation with wavelengths between about 0.01 and 10 nm. By using x-rays with wavelengths on the same order as the interatomic spacings in a crystal, around 0.1nm, diffraction experiments can be performed, probing the periodic nature of the crystal lattice. Constructive interference of elastic scattering of x-rays by electrons in the crystal leads to strong diffraction under conditions given by Bragg's law:

$$n\lambda = 2dsin\,\theta \qquad (2\text{-}10),$$

when n is an integer, λ is the x-ray wavelength, d is the atomic plane spacing, and θ is the angle between the crystal planes and the x-rays [106]. Figure 2-14 shows an x-ray beam and its diffraction from a crystal. ω and θ are the x-ray source and detector angles with the sample surface, respectively. For crystal planes parallel to the sample surface ω is equal to θ. By using a fixed-wavelength source and mounting the sample on a goniometer, the ω/θ angles could be adjusted to gather information about the crystal planes present in the sample. There are many types of scans. The simplest type of measurement is to vary the ω/θ angle systematically with Δω=Δθ while recording the

diffracted intensity. The plane spacing *d* can be determined by Bragg' law. These parameters can also be calculated from dynamical diffraction theory [107].

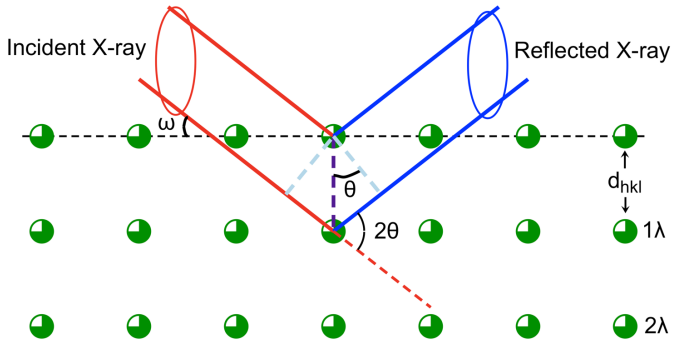

Figure 2-14. Diffraction of x-rays from atomic planes, assumed to be parallel to the sample surface. ω is the angle between the incident beam and the sample surface.

The Bruker D8 Discover Diffractometer generates x-rays by accelerating electrons at 40 kV potential toward a copper target in a vacuum tube. The emitted x-rays go through collimating and monochromator optics and a K_α x-ray beam at 0.154051 nm wavelength hits the sample. The sample is loaded on a goniometer with a resolution of 0.0001° that can change any of the three rotational or three translational degrees of freedom of the sample independently. The diffracted beam goes through a slit and is detected by an analyzer crystal with the best resolution of 16 arcsec.

2.9 Reciprocal Space Mapping (RSM)

Figure 2-15 is a section through reciprocal space for a (001)-oriented epitaxial Zn_3N_2 film on a (001)-oriented MgO substrate. This figure shows the volume of the probe in reciprocal space (magnification box) depends on the divergence of the incident beam k_i

(Δω) and the divergence of the diffracted beam k_s. Regions of reciprocal space where the sample surface blocks the incident or diffracted beam are shown in dark (inaccessible). The vectors k_i and k_s have the length $2\pi/\lambda$ (where $\lambda = 0.154$ nm); the vector k has a length of $2\pi/d_{002}$ and is perpendicular to the (002) plane. The Ewald sphere is shown in figure 2-15 as a red dashed circle, cutting the 002 reciprocal lattice spot.

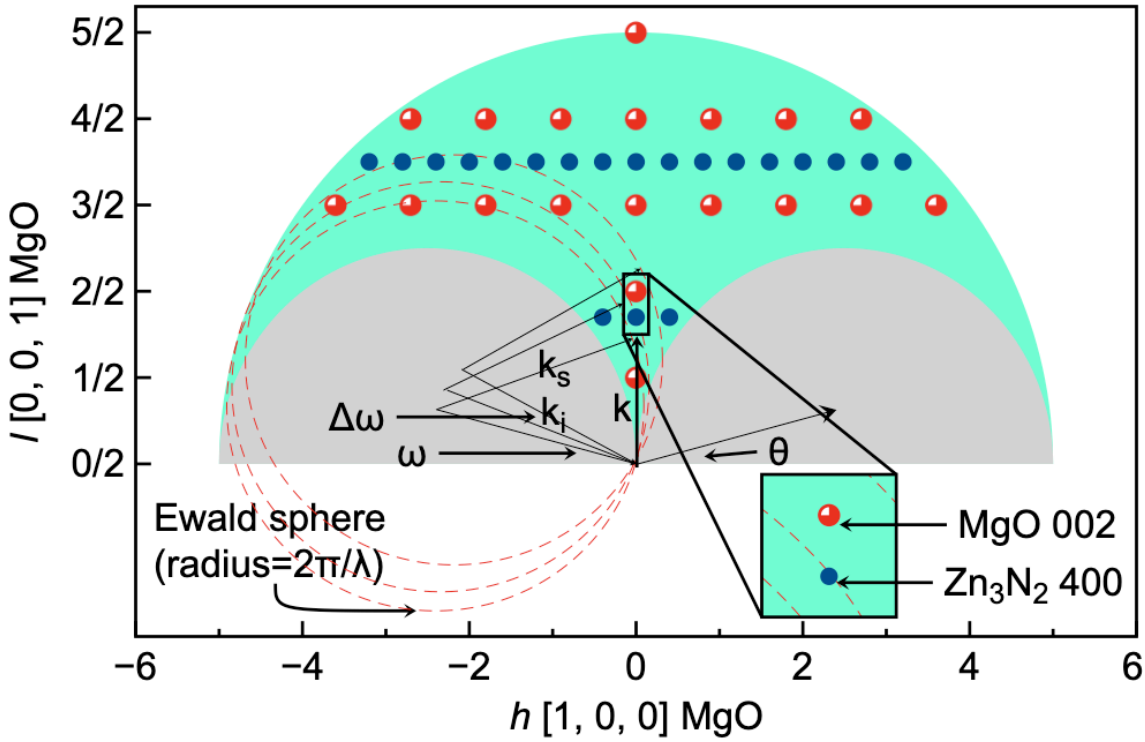

Figure 2-15. Reciprocal space map containing the {100} family of peaks of MgO and Zn_3N_2. Peaks are specified in units of Miller indices.

The typical scan is a ω-2θ scan in which the diffracted intensity is plotted as a function of angle. This scan essentially measures a single vertical line through reciprocal space. Diffraction can also be illustrated in the context of the reciprocal lattice. If the incident k_i and scattered k_s beam vector make an appropriate angle with respect to the

crystal, the momentum transfer *k* will end at a reciprocal lattice point as shown in figure 2-15. The momentum transfer *k* is the 'probe' used to investigate the reciprocal lattice and its length can be altered by changing the angles ω/2θ. The direction of *k* is scanned by changing ω, the angle at which the incident beam meets the sample surface [108]. Therefore, to investigate different areas of the reciprocal space, either the crystal orientation or length of the *k* can be changed by changing the angle ω and 2θ. As figure 2-15 shows, the Ewald sphere can be constructed by using the radius 2π/λ. This sphere shows which part of reciprocal space I can explore with *k*, and the *k* can be increased to the maximum wavevector 2π/λ. A diffraction peak occurs when the sphere touches a reciprocal lattice point.

High resolution diffractometers contain an x-ray source and a detector along with incident and/or diffracted beam conditioners. Much information regarding interplanar spacings and defect-related broadening can be obtained from reciprocal space maps (RSMs), which show the scattered intensity for a 2D section through reciprocal space. RSMs can be obtained by taking a series of ω-2θ scans at successive ω values (or vice versa) and presenting the results in the map form. In order to plot such maps, the angles made by the incident beam with respect to the sample surface (ω) and the angle made by the scattered beam with respect to the 'straight-through' incident beam (2θ) are usually converted into reciprocal lattice units (RLU), *s* (1 RLU = $1Å^{-1}$ = 2(sin θ)/λ) using the following formula [109]:

$$k_x = \frac{1}{\lambda}[cos\omega - \cos(2\theta - \omega)], \quad Q_x = 2\pi k_x \qquad (2\text{-}11),$$

$$k_z = \frac{1}{\lambda}[\sin\omega - \sin(2\theta - \omega)], \quad Q_z = 2\pi k_z \qquad (2\text{-}12).$$

This allows direct conversion of the angles used in measurements to coordinates in reciprocal space. However, it is common in solid state physics to use the units Q_x and Q_z. The physical size and shape of the sample and instrumental broadening can affect scans as well as microstructural features; these factors are convoluted together in a complex manner and the separation of the broadening due to each factor is difficult. There are two types of significate broadenings in reciprocal space: vertical broadening and horizontal broadening. The vertical direction of broadenings may be caused by a small layer thickness, the small vertical thickness of coherently diffracting domains, vertical strain, or composition fluctuations. Correspondingly, the small lateral width of coherently diffracting domains or lateral strain, or composition fluctuations may cause a broadening in the horizontal direction.

2.10 Optical Property Measurement

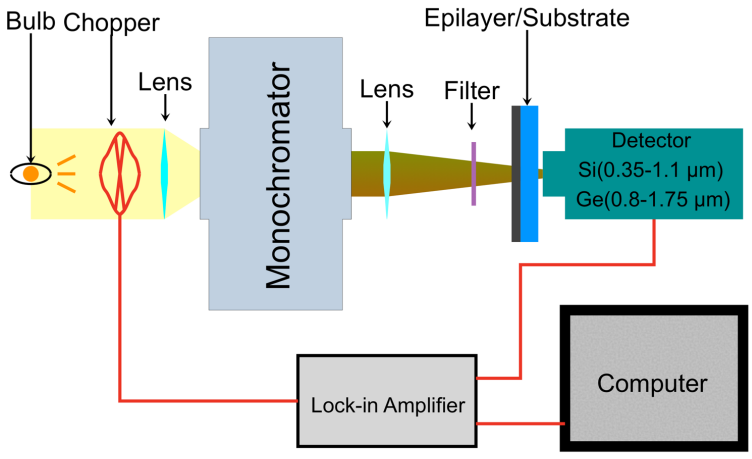

Figure 2-16. Schematic of the optical transmission spectroscopy setup.

2.10.1 Transmittance Measurement

Absorbance and transmittance are two related, but different quantities used in spectrometry. The main difference between absorbance and transmittance is that absorbance measures how much incident light is absorbed when it travels in material while transmittance measures how much of the light is transmitted. Transmittance is defined as the ratio of the intensity of the transmitted light to the intensity of the incident light:

$$T = \frac{I}{I_0} \tag{2-13}$$

Even if in common usage the term "absorption spectroscopy" is employed, usually it is the transmittance T that is measured [110]. The transmittance is always presented as a percentage ($\%T$).

Figure 2-16 shows the optical transmittance spectroscopy setup. In this thesis, white light from a halogen bulb was chopped at 199 Hz and focused on the entry slit of a monochromator. The samples were illuminated at normal incidence with monochromatic light and the transmitted light was detected using un-cooled 2 mm Si (350-1100 nm) and 1mm Ge (800-1750 nm) photodetectors, connected to a lock-in amplifier, and a combination of optical long-pass filters. In the experiment, the radiation absorber layer of the sapphire substrate was polished off by sandpaper. The matter back surface of the substrate was placed close to the detector to maximize collection of the transmitted specular and scattered light. The specular transmittance of the epilayer was isolated by

dividing the spectra of the epilayer/substrate heterostructure sample by that of an uncoated substrate reference sample (T_{sample} / $T_{substrate}$). The epilayer sample and a reference substrate were measured immediately after each other to minimize any possible drift in optical power.

The transmittance *T* through a slab of a material or a solution is converted into the absorption coefficient α by the well-known formula [111][112][113]:

$$T = (1 - R)e^{-\alpha d} \quad \text{or} \quad T \propto e^{-\alpha d} \qquad (2\text{-}14),$$

$$\alpha = \frac{1}{d} ln(\frac{1-R}{T}) \quad \text{or} \quad \alpha \propto \frac{1}{d} ln(\frac{1}{T}) \qquad (2\text{-}15),$$

where *d* is the thickness of the sample, and *R* is reflectance. For optical measurements of Mg_3N_2 and Zn_3N_2 thin films in this thesis, *R* is assumed to be zero. This means the measurements of α are not reliable at low absorption.

The bandgap of the material can be derived from the absorption coefficient, α. The bandgap is the energy difference between the bottom of the conduction band and top of the valence band in a semiconductor or insulator. In this energy range no electron band states exist. Each material has a unique energy-band structure which controls its electrical attributes. The relationship between permittivity (known as complex dielectric constant), $\tilde{\varepsilon}$, and the complex index of refraction, $\tilde{n}$, is needed to relate the absorption coefficient to the bandgap energy:

$$\tilde{\varepsilon} = \varepsilon_1 + i\varepsilon_2 = \tilde{n}^2 \qquad (2\text{-}16).$$

The complex index of refraction can be written as: $\tilde{n} = n + ik$, where n is the refractive index indicating the phase velocity, and k is the extinction coefficient, indicating the amount of attenuation of electromagnetic waves propagating through a material. The attenuation of light passing through an absorbing medium is described by the absorption coefficient α where

$$\alpha = \frac{2\omega k}{c} = \frac{4\pi k}{\lambda} \quad (2\text{-}17).$$

The absorption coefficient can be related to the imaginary part of the permittivity using equation (2-16) [114]

$$\varepsilon_2 = 2nk \quad (2\text{-}18a).$$

Take into account the equation (2-17), (2-18a) can be written as

$$\varepsilon_2 = 2nk = \frac{\alpha n\lambda}{2\pi} = \frac{\alpha nhc}{2\pi h\nu} \propto \frac{\alpha n}{h\nu} \quad (2\text{-}18b),$$

where $h\nu$ is the photon energy.

The imaginary part of the permittivity of a semiconductor close to and above the bandgap is also given by [114]

$$\varepsilon_2 \propto \frac{1}{(h\nu)^2}(h\nu - E_g)^p \quad (2\text{-}19).$$

By using equations (2-18b) and (2-19), an expression for absorption coefficient in terms of the bandgap energy is found by [115]

$$\alpha h\nu \propto (h\nu - E_g)^p \qquad (2\text{-}20),$$

where p is a bandgap transition dependent exponent with the possible values listed in table 2-3. Therefore, a plot of $\alpha^{1/p}$ v.s. $h\nu$ should demonstrate a linear relation as a function of photon energy and provide an estimate of E_g from the $h\nu$-intercept [116].

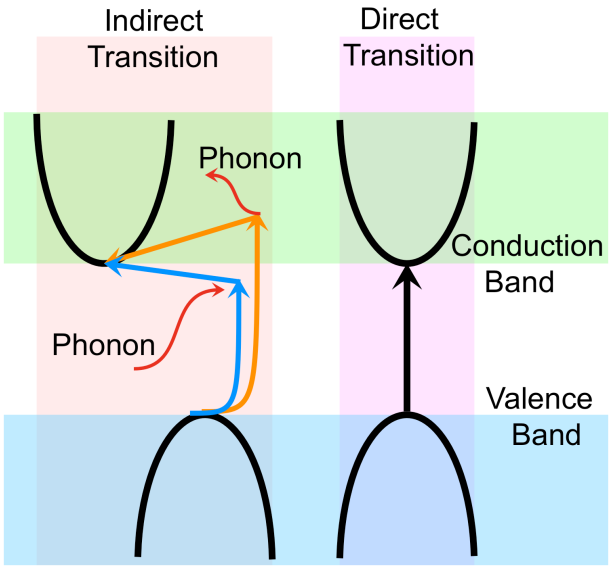

Figure 2-17. Schematic of the direct and indirect bandgap.

Table 2-3. Absorption edge parameter p values for different bandgap types.

Bandgap Type	Direct		Indirect	
	allowed	forbidden	allowed	forbidden
p [117]	1/2	3/2	2	3

The bandgap transition exponent is dependent on whether the bandgap transition is direct or indirect, shown in figure 2-17, and if the transition is allowed or forbidden [118]. A direct bandgap transition is where the energy changes, but the momentum is conserved. It is formed when the lowest energy point of the conduction band and the highest energy point of valence band has the same value in *k*-space. An indirect bandgap transition is one where both the energy and the momentum change and is formed when the lowest energy point of the conduction band and the highest energy point of the valance band that have different locations in *k*-space. Transitions are allowed if the matrix element characterizing the transition is non-zero. The transitions and coefficients are derived through quantum perturbation theory of optical transitions.

2.10.2 Spectroscopic Ellipsometry (SE)

As an optical technique, SE is non-destructive and contactless. It is based on the change in the polarization state of light as it is reflected obliquely from a thin film sample (see figure2-18). SE is a versatile thin film characterization technique that has applications in many different fields. This sensitive measurement technique provides unequaled capabilities for thin film metrology and provides thin film thickness with angstrom resolution.

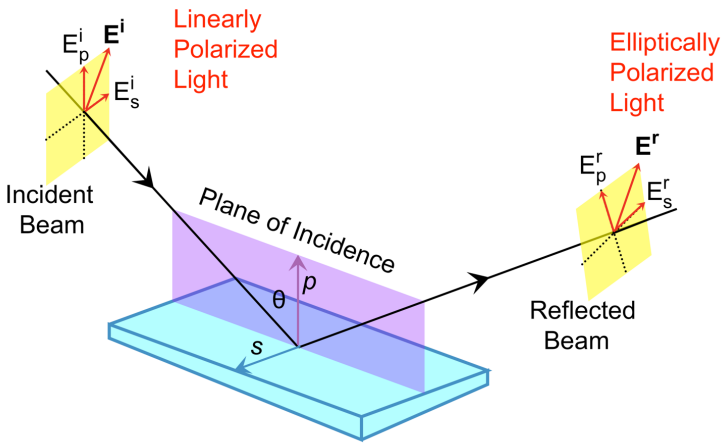

Figure 2-18. Schematic of the elliptically polarized light.

If the polarization is considered in figure 2-18, the reflectivity (figure 2-18) can be expressed as [97][119] [120]

$$r_p = \frac{\tilde{n}_1 \cos\theta - \cos\theta_1}{\tilde{n}_1 \cos\theta + \cos\theta_1} = \frac{E_p^r}{E_p^i} \quad \text{(2-21a)},$$

$$r_s = \frac{\cos\theta - \tilde{n}_1 \cos\theta_1}{\cos\theta + \tilde{n}_1 \cos\theta_1} = \frac{E_s^r}{E_s^i} \quad \text{(2-21b)}.$$

By using the Jones Vector:

$$\mathrm{E} = \begin{bmatrix} E_s \\ E_p \end{bmatrix} = \begin{bmatrix} A_s e^{j\phi_s} \\ A_p e^{j\phi_p} \end{bmatrix} \quad \text{(2-22)},$$

where A_s and A_p are complex constants that must be nonzero, define a new term, ρ , which is the ratio between the two components in the reflectivity:

$$\rho = \frac{r_p}{r_s} = \frac{\frac{E_p^r}{E_p^i}}{\frac{E_s^r}{E_s^i}} = \frac{E_p^r E_s^i}{E_p^i E_s^r} = \frac{A_s^i}{A_p^i} e^{j(\phi_s^i - \phi_p^i)} \frac{A_p^r}{A_s^r} e^{j(\phi_p^r - \phi_s^r)} \quad (2\text{-}23),$$

if the incident light is linearly polarized with ϕ^i=0 and $A_s^i = A_p^i$, then (2-23) is given as

$$\rho = \frac{A_p^r}{A_s^r} e^{j(\phi_p^r - \phi_s^r)} \quad (2\text{-}24),$$

which only contains information for the polarized reflected light. For the reflected light, the amplitude ratio Ψ is defined in order to satisfy the following:

$$\tan \Psi = \frac{A_p^r}{A_s^r} \quad (2\text{-}25).$$

Furthermore, the phase difference Δ is defined as

$$\Delta = \phi_p^r - \phi_s^r \quad (2\text{-}26).$$

Using (2-25) and (2-26), (2-24) can be expressed as

$$\rho = \tan \Psi \, e^{j\Delta} \quad (2\text{-}27),$$

which is a general ellipsometry equation.

The dielectric function is given as [121]

$$\tilde{\varepsilon} = sin^2(\theta)\left[1 + tan^2(\theta)\left(\frac{1-\rho}{1+\rho}\right)^2\right] \quad (2\text{-}28),$$

where θ is the incident angle.

Using equation (2-16), (2-28) can be written as

$$(n + ik)^2 = sin^2(\theta)\left[1 + tan^2(\theta)\left(\frac{1-\rho}{1+\rho}\right)^2\right] \quad (2\text{-}29).$$

Thus, optical constants were determined from fitting the amplitude ratio, Ψ, and the phase difference, Δ in equation (2-29).

2.11 Electron Transport Measurement

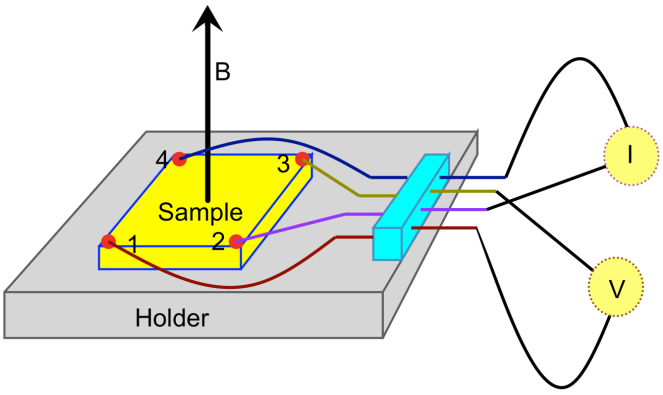

Figure 2-19. van der Pauw configuration for Hall measurements.

Electrical resistivity is a key physical property of all materials. It is often necessary to accurately measure the resistivity of a given material. The van der Pauw method is the standard technique for measuring the resistivity as well as Hall effect on a sample with arbitrary shape [122][123]. In this thesis, square shape samples with small corner-side contacts are used, as shown schematically in Figure 2-19. Before gluing the sample on the holder, I used silver epoxy to make the four small electrical contacts. The holder can be either a glass slab or a copper plate in the case of the temperature dependence measurement. The glass holder is used to perform the measurement at room temperature and the copper holder is used for low temperature measurements. In the four-probe technique the current source and voltage measurement contacts are separated. A current source drives a certain current between two corners on one side of the square sample and a voltmeter measures the voltage on the other two corners. The current source and voltmeter can be connected to the sample in four different configurations which result in four resistances, $R_{12,34}$, $R_{34,21}$, $R_{21,43}$, $R_{43,21}$, measured in between the sample four corners. The average horizontal resistance is

$$R_H = \frac{R_{12,34}+R_{34,21}+R_{21,43}+R_{43,21}}{4} \quad (2\text{-}30).$$

Similarly, the vertical resistance is

$$R_V = \frac{R_{14,23}+R_{41,32}+R_{23,14}+R_{32,41}}{4} \quad (2\text{-}31).$$

The sheet resistance, R_s, of the sample is calculated from the van der Pauw's formula:

$$e^{-\pi\frac{R_V}{R_S}} + e^{-\pi\frac{R_H}{R_S}} = 1 \quad \text{(2-32).}$$

The resistance $R_{12,34}$ is determined by dividing the horizontal potential difference V_{12} by the horizontal current I_{34} and resistance $R_{14,23}$ is defined similarly.

If a magnetic field is applied to the film and the current source puts a diagonal current in the sample and the voltage on the other diagonal is measured (see figure 2-19), this voltage is referred to as the Hall voltage V_H. It is the result of the equilibrium between magnetic and electric forces. In this thesis, the magnetic field can be applied in two directions (+B, -B), so eight Hall voltages are measured. The sum of all Hall voltages is used to calculate the carrier concentration of the sample,

$$n_s \; or \; p_s = \frac{IB}{qV_H} \quad \text{(2-33a),}$$

$$n = \frac{n_s}{d} = \frac{IB}{dqV_H} \quad \text{(2-33b),}$$

where the sign of the Hall voltage, V_H, indicates the type of the majority carriers (electrons or holes) [124], and d is the sample thickness.

The carrier mobility μ is the proportionality constant between the drift velocity $\vec{v}_d$ and the applied electric field $\vec{E}$ and indicates how fast the carriers are moving in response to the electric field

$$\vec{v}_d = \mu\vec{E} \quad \text{(2-34).}$$

As both sides of equation (2-34) can be expressed in terms of current density:

$$\vec{J} = \frac{\vec{E}}{R_s} = qn\vec{v}_d \quad (2\text{-}35),$$

where R_s is the sheet resistance.

The carrier mobility becomes

$$\mu = \frac{1}{qnR_s} \quad (2\text{-}36),$$

where q is the fundamental unit of charge.

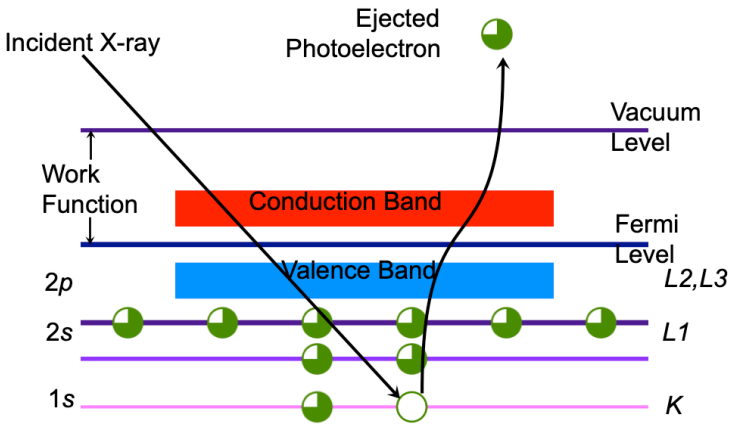

Figure 2-20. Energy level diagram with a schematic view of the photoemission process.

2.12 X-ray Photoelectron Spectroscopy

X-ray photoelectron spectroscopy (XPS) is a surface analysis technique capable of determining the chemical composition of the first few atomic layers at the surface of a

solid sample. It is generally estimated that the depth of analysis ranges from 2-10 nm [125]. Subject to the irradiation of the $h\nu$ -energy x-ray beam, the surface of the sample emits electrons into the vacuum with energy ranging from 0 to $h\nu$, called photoelectrons. Measuring the kinetic energy of the electrons (E_K) emitted enables one to determine the binding energy (E_B) of the photoelectrons detected. The binding energy $E_B = h\nu - E_K - \varphi_A$, where φ_A is the work function of the analyzer, which is the distance between the Fermi level and the vacuum level (see figure 2-20). In a semiconductor the binding energy is normally referenced to the top of the valence band. Chemical analysis is possible by knowing the electron binding energies associated with the various atoms [126]. In the XPS spectrum, the photoelectron intensity is plotted as a function of the binding energies. This spectrum comprises two sets of information: peak position and peak intensity. The position of the peaks in binding energy enables one to determine the chemical elements making up the surface. Table 2-4 shows the binding energy of the elements which are considered in the following chapter.

Table 2-4. Photoemission binding energy for various elements.

Elements		Zn		Mg *2p*	N *1s*	O*1s*
		2p 3/2	*2p 1/2*			
Binding Energy (eV)	peak	1021.8	1045	49.8	398.1	531
	range	1020.5-1023.1	1043-1047	49.1 - 51.1	396 - 408	528.2 - 533.7

The intensity of each of these peaks enables us to determine the concentration of these chemical elements. The relative sensitivity factor (RSF) method [127] was employed to estimate the Mg concentration *x* which can be defined by

$$x = \left(1 + \frac{I_{Zn}}{I_{Mg}} \frac{S_{Mg}}{S_{Zn}}\right)^{-1} \quad \text{(2-37)},$$

where I_{Mg} and I_{Zn} are the integral intensities of the Mg peak and the Zn peak, respectively, and the elemental sensitivity factor S_{Mg} = 0.12 and S_{Zn} = 3.72 are provided by PHI [126]. The quantitative and qualitative analysis turns XPS into a technique that is well suited for measuring the chemical composition of the surface of thin films.

Chapter 3 Single crystal Zn_3N_2 thin film growth and optical properties characterization

Recently, Zn_3N_2 films have been fabricated by the sputtering technique by researchers all over the world: Núñez et al. in Spain [35][77][128], Trapalis et al. in United Kingdom [79][130], Yamada et al. in Japan [69][80][81], and Ayouchi et al. in Portugal [71], Yamada et. al developed the Zn_3N_2 epitaxial growth by sputtering, and Sinha et al. and Maria et al. both grew Zn_3N_2 films for TFT application by using atomic layer deposition (ALD) and pulsed laser deposition (PLD), respectively [73]. In 2006, Oshima et al. grew the Zn_3N_2 films on the sapphire substrate by MBE [30]. Unfortunately, the films showed polycrystalline texture patterns in the RHEED investigation. To optimize the growth conditions and get high-quality material, the plasma assisted MBE system and high purity sources were applied (see table 2-1) for thin film growth in this thesis.

3.1 Zn_3N_2 Thin Film Growth

Commercial MgO and A-plane α-Al_2O_3 substrates were placed on a sapphire wafer before being loaded into a tube furnace for 9 hours annealing in air (1000°C). The substrates are heated at high temperature in order to remove carbon contamination from the surface and to improve the crystalline order in the substrate surface. Different from the MgO substrate, the back surface of the A-plane α-Al_2O_3 substrate was coated with 100 nm Cr and 200 nm Mo by electron beam evaporation in order to improve radiative coupling between the heater and the substrate. The substrates were cleaned by boiling in acetone and then blown dry with nitrogen. The substrates were loaded into the MBE preparation chamber and thermally cleaned at 400°C for 5 hours and then moved to the

growth chamber where they were heated to 800°C for 30 min. During growth, high purity (99.9995%) nitrogen gas at a constant flow rate of 3 sccm was introduced into the growth chamber through a plasma source energized with 300 W of RF (13.56 Mhz) power. The Zn source consisted of an effusion cell containing high purity Zn (99.9999%) in a pyrolytic boron nitride crucible maintained at a constant temperature between 300°C and 340°C depending on the desired Zn flux in the 0.1-0.6 nm/s range.

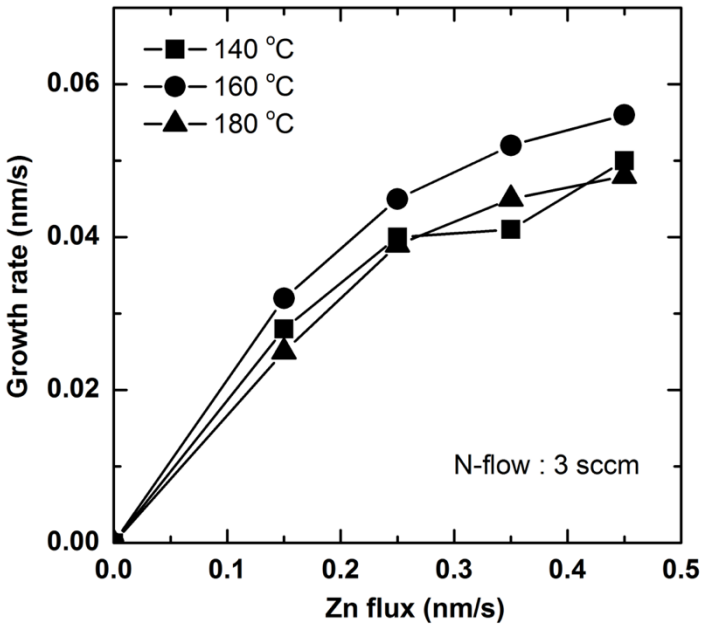

Figure 3-1. Growth rate of Zn_3N_2 films at three substrate temperatures.

Samples were grown at substrate temperatures of 140°C, 160°C, and 180°C. The substrate temperature was measured with a thermocouple located in the vacuum space between the substrate holder and heater, therefore the substrate temperature measurement must be considered to be approximate. The as-grown samples had a dark metallic appearance, which faded to a blue color and finally whitish color over a period of a

month in summer and a week in winter in room air as the sample oxidized, presumably depending on humidity. Figure 3-1 shows the growth rate as a function of the zinc flux for three different substrate temperatures. The shape of the growth rate curve as a function of the Zn-flux is explained as follows. When the Zn flux is low, the surface is nitrogen rich and the growth rate is limited by Zn availability. At high Zn fluxes, above approximately 0.25 nm/s, the growth rate saturates and is limited by the N-flux which is constant. The growth rate does not depend on the substrate temperature in this range although above 270^{o}C no growth was observed. The thin film's growth rate at 160 ^{o}C higher than that is at 180 ^{o}C due to the surface desorption rate increasing as the temperature increases.

Figure 3-2 shows the specular reflectance at 488 nm as a function of time during film deposition together with the calculated reflectance as a function of time. The measured reflectance *R* shows interference oscillations during growth which damp out as the film thickness increases, indicating that the film is absorbing at the laser wavelength. In the simulated reflectance the growth rate and absorption coefficient have been adjusted to give a best fit to the data as explained below.

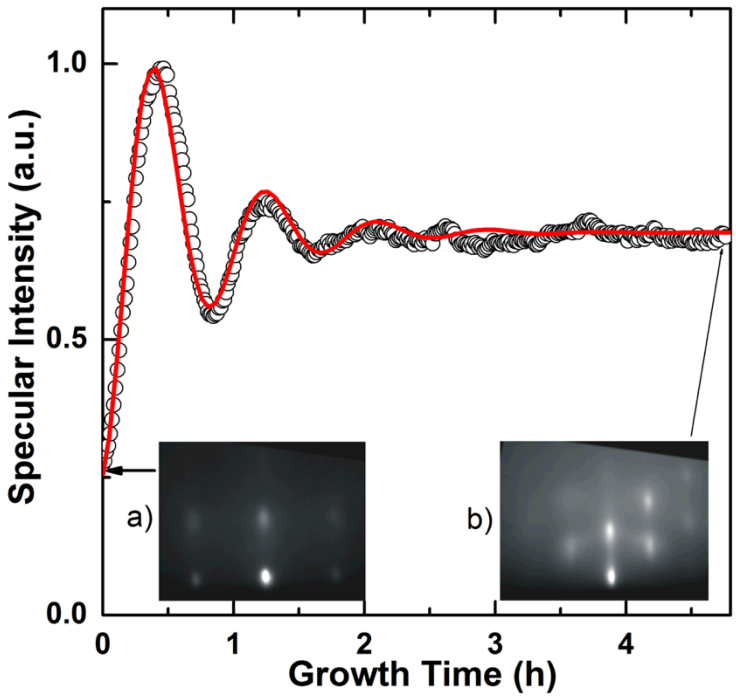

Figure 3-2. In-situ specular reflectivity at 488 nm of a Zn_3N_2 film. The calculated reflectivity (red line) is a best fit to the experimental spectrum (black circles) as discussed in the text. Insets a) and b) are the RHEED patterns for a bare MgO (100) substrate and a growing film, respectively.

I fit the in-situ reflectivity of the growing Zn_3N_2 film with the expression in Equation (2-9) using the growth rate, g, extinction coefficient, k_1, and index of refraction, n_1, as adjustable parameters. In the model the refractive index of MgO is n_2=1.747 at 488nm, θ=36.5° is the laser incidence angle and λ=488nm is the wavelength of the laser. The best fit was achieved with n_1=2.65, k_1=0.53 (or $\alpha=7.0\times10^4$ cm^{-1}) and g=0.035 nm/s (0.13 μm/hr). The absorption coefficient obtained from the fit is in good agreement with our experimental data in figure 3-4, but somewhat smaller than the value $\alpha=10\times10^4$ cm^{-1} obtained from ellipsometry measurements by Nunez et al. [128]. The measured index of

refraction is larger than the value reported earlier (n_1=2.3) [128].

Insets (a) and (b) in figure 3-2 show the RHEED patterns for the bare MgO substrate and a growing film respectively. The electron beam is incident along the $[1\bar{1}0]$ direction of the MgO substrate. The distinct elliptical spots in figure 3-2 (b) shows that the deposited Zn_3N_2 film are ordered in the plane of the substrate and those spots pattern suggests that the Zn_3N_2 film is a single crystal film.

3.2 Properties of Zn_3N_2 Films

3.2.1 X-Ray Diffraction

The $\omega/2\theta$ scans in figure 3-3(a) show (400) Zn_3N_2 peaks for 450nm Zn_3N_2 /Al_2O_3 and 400nm Zn_3N_2 /MgO structures with no indication of any other phases or crystal orientations. The RHEED spots for the Zn_3N_2 films on the sapphire substrates were not as clear and sharp as for the films on the MgO substrates. Figure 3-3(b) shows a reciprocal space map of the Zn_3N_2 (400) and MgO (200) peaks. Q_x and Q_y refer to the in-plane and out-of-plane directions, respectively. The FWHM of the (400) Zn_3N_2 peaks on sapphire and MgO were 0.133° and 0.125° respectively (θ width), indicating slightly better structural quality on MgO.

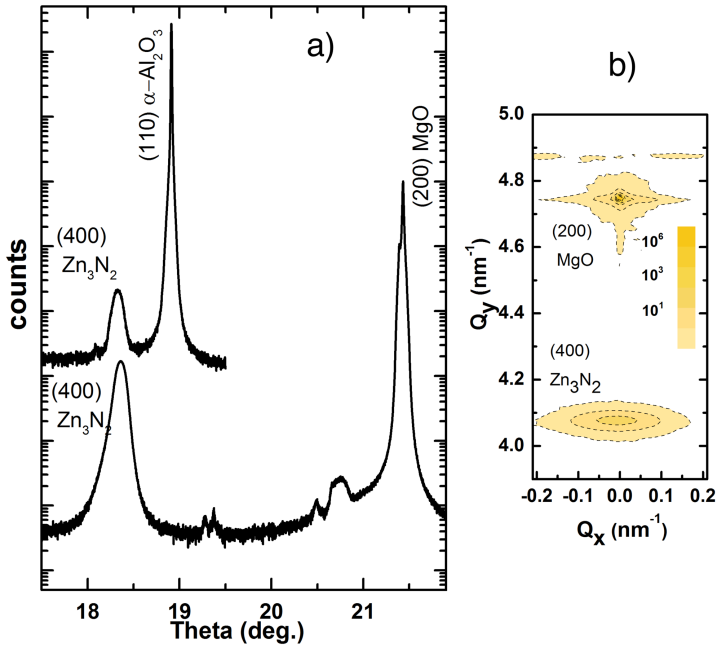

Figure 3-3. High resolution XRD θ-2θ scans for a 450 nm Zn_3N_2 film on Al_2O_3 and 400 nm Zn_3N_2 film on a MgO substrate. Scans are offset vertically for clarity. The inset shows a reciprocal space map for the 400 nm Zn_3N_2 film on the MgO substrate. The small peaks between θ=19° and 21° are diffractometer artifacts and are not associated with the film.

3.2.2 Optical Transmission Measurements

Figure 3-4 shows optical transmission spectra for four different Zn_3N_2 films. A sharp absorption onset is observed below about 1000 nm. The long wavelength transmission is consistent with the calculated reflectivity of the Zn_3N_2/MgO and Zn_3N_2/Al_2O_3 structures using the refractive index from figure 3-2. The calculated reflectivity for a thick Zn_3N_2 film on MgO, neglecting interference oscillations, is 22% which is consistent with the measured ~70-80% transmittance of the Zn_3N_2 films above

1000 nm. The oscillatory wavelength dependence of the transmission at long wavelengths is due to thin film interference. The transmittance of Zn_3N_2 films on double polished MgO substrates is 8% higher than on the single polished sapphire substrates due to scattering from the rough back surface of the sapphire substrates.

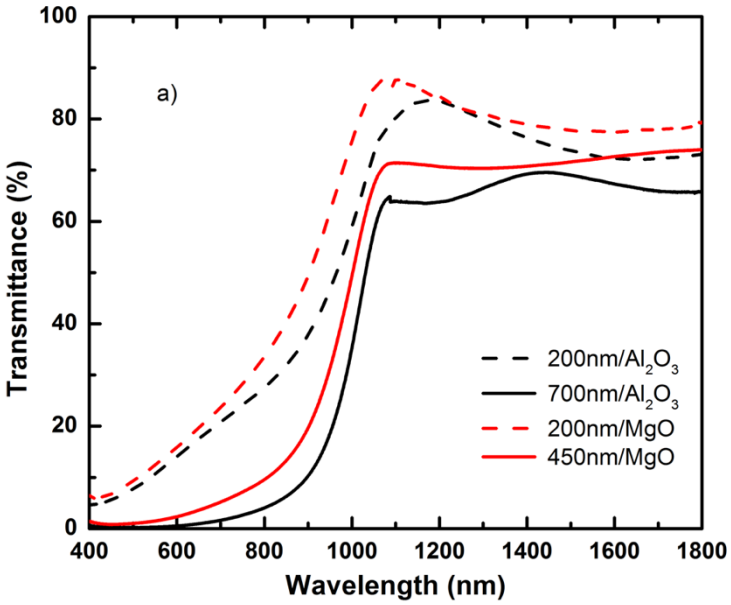

Figure 3-4. Room temperature optical transmission spectra of Zn_3N_2 thin films with the film thicknesses and substrates indicated on the figure.

If I ignore the reflectivity R, the absorption coefficient, α, is equal to $-\frac{1}{d}\ln\left(\frac{1-R}{T}\right)$, where d is the layer thickness, and T is the transmittance. Figure 3-5 shows the absorption spectra of the as-grown Zn_3N_2 films in the energy range 0.8-3.0 eV. There is a sharp transition between weak absorption at low photon energies and high absorption at high energies, which I interpret to be associated with the bandgap of the material. For a direct bandgap semiconductor, in the vicinity of the bandgap, the absorption coefficient as a

function of photon energy $h\upsilon$ is given by equation (2-20). Assuming Zn_3N_2 is a direct bandgap semiconductor, the bandgap transition dependent exponent, p value is ½ as discussed in chapter 2.

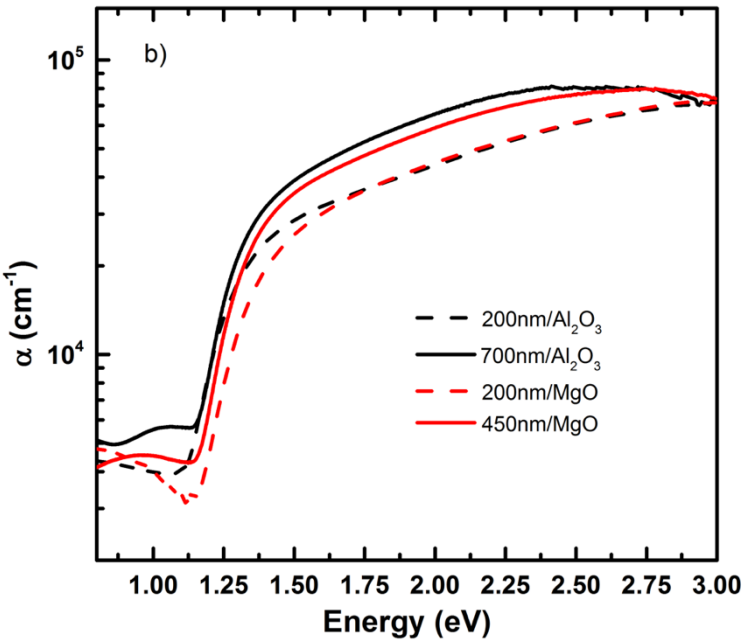

Figure 3-5. Absorption coefficient α as a function of photon energy for the same Zn_3N_2 thin films as in figure 3-4.

Therefore, a plot of $(\alpha h\upsilon)^2$ vs. photon energy should extrapolate linearly to zero at the bandgap, E_g. Figure 3-6 shows how this extrapolation of the experimental data can be used to determine the bandgap, which is found to be 1.25 eV and 1.28 eV for the 700 nm thick Zn_3N_2/Al_2O_3 sample and the 450 nm thick Zn_3N_2/MgO sample, respectively. These bandgap values are in good agreement with the bandgap of Zn_3N_2 made by reactive sputtering [22]. Attempts to detect photoluminescence (PL) of Zn_3N_2 thin films at room

temperature and low temperatures were not successful presumably due to the presence of excessive defects in the material that act as non-radiative recombination centers.

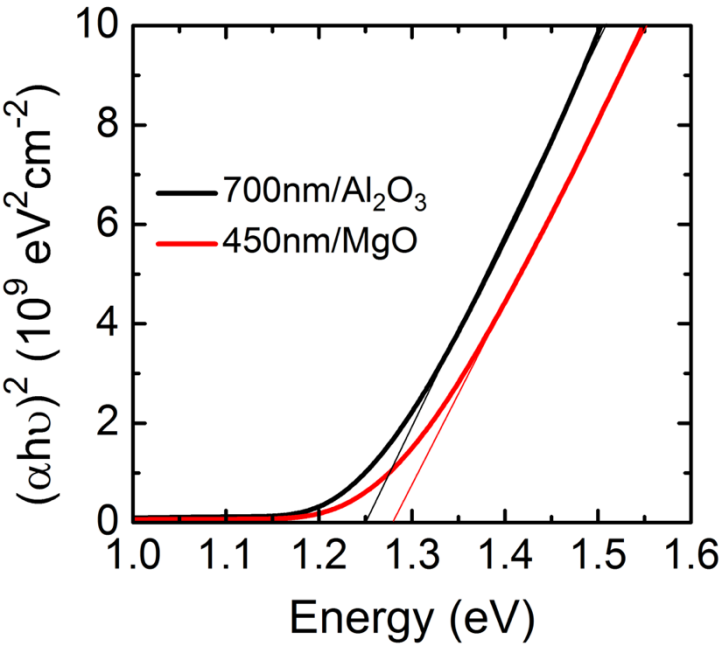

Figure 3-6. The inset is a plot of $(\alpha h\upsilon)^2$ vs. photon energy, which is used to determine the optical band gap.

H. Alimohammadi, one of my collaborators, performed the low temperature PL spectroscopy of Zn_3N_2 powder [129]. The resulting spectra have been analyzed in order to characterize several features of the crystal including its impurities and defects. The low temperature PL spectrum of Zn_3N_2 powder is shown in figure 3-7. As expected, by decreasing temperature from 250K to 10K, the peak intensity and the PL energy both increase. This result agrees with the conventional trend of increasing intensity at low temperature and shows the bandgap has shifted to higher energy by decreasing the temperature. The PL peak energy is in the 0.95-1.0 eV range somewhat lower than the

bandgap determined from the transmission measurements on thin films. Since the PL emission is broad (0.2 eV) the PL likely comes from defect states and provides a lower limit estimate for the bandgap. From the PL data on the powder sample we conclude that the room temperature bandgap is greater than about 1.1 eV, the high energy edge of the PL emission spectrum. This result is in reasonable agreement with the bandgap obtained from the transmission measurements on thin films.

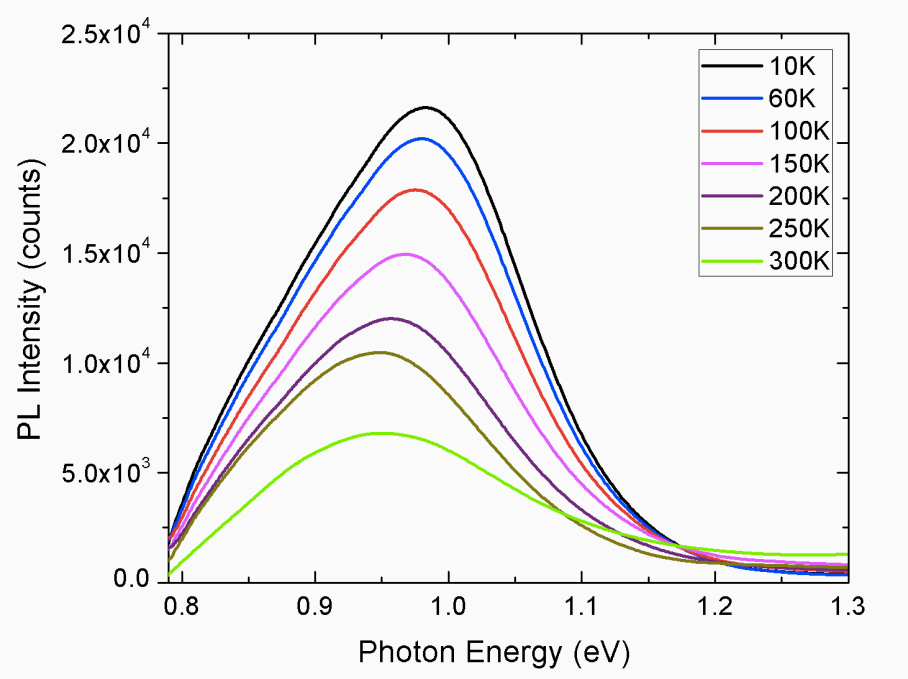

Figure 3-7. Temperature dependence of PL spectrum for Zn_3N_2 powder.

3.2.3 Spectroscopic Ellipsometry

Spectroscopic ellipsometry (SE) was carried out in order to determine the optical parameters of the films. The ellipsometry system was used to obtain the amplitude ratio Ψ and phase difference Δ of the layers as a function of the photon energy in the 1.4-3.1 eV range. These values were used to calculate *n* and *k* as a function of photon energy.

Figure 3-8 shows the results of the SE measurement. The experimental data shows the change in electric field amplitude and phase for *p*- and *s*-polarizations. For single crystal Zn_3N_2 thin film, the Ψ (black circles) and Δ (red circles) are well fitted by equation (2-29), and the optical constants, *n* and *k*, were derived from the fit.

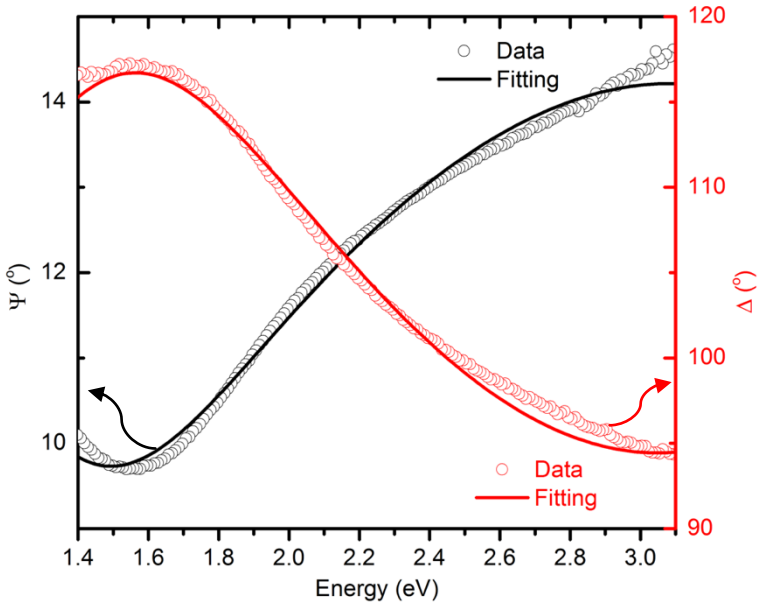

Figure 3-8. Ψ (black circles) and Δ (red circles) of Zn_3N_2 thin film. Solid lines represent the fitting curves of the equation (2-29).

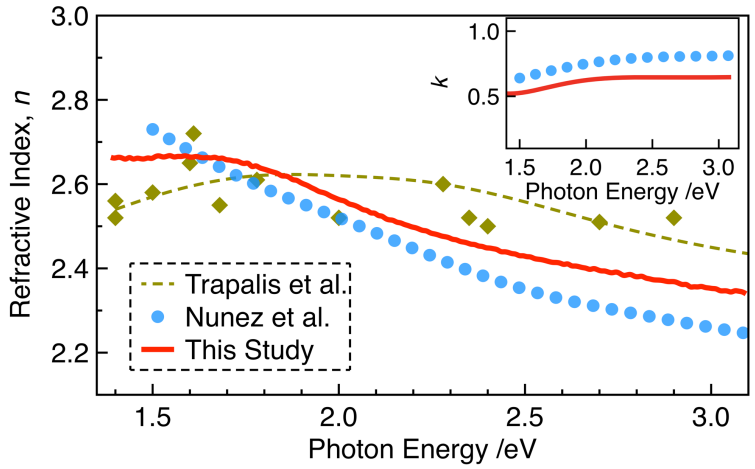

Figure 3-9. Optical constants of Zn_3N_2 as a function of the photon energy.

Figure 3-9 shows the optical constants of Zn_3N_2 thin films. The refractive index of the single crystal Zn_3N_2 from this work is higher than that of Nunez's report and lower than that of Trapalis's work [128][130]. Our Zn_3N_2 film shows a slightly lower extinction coefficient than the polycrystalline film reported by Nunez et al. Table 3-1 summarizes the refractive index and optical band gap of Zn_3N_2 films both from the literature and this study. This study is similar to the results of Nunez et al. and Trapalis et al. However, Ayouchi's and Simi's reports show a lower refractive index and larger bandgap. The wider band gap reported in the literature may be the result of unintentional oxidation rather than a difference in material quality. It is worth mentioning that Zn_3N_2 thin films show an unusual anomalous dispersion in the refractive index, namely, the refractive index decreases with increasing the photon energy above the bandgap. The reason for this anomalous dispersion is unknown.

Table 3-1. Refractive index and optical band gap of Zn_3N_2 films

Reference	Refractive index (1.5-3.1 eV)	Extinction coefficient (1.5-3.1 eV)	Optical band gap (eV)
This study	2.35-2.67	0.5-0.6	1.25-1.28
Nunez *et al*. [128]	2.3-2.73	0.6-0.75	< 1.5
Trapalis *et al*. [130]	2.45-2.6	___	1.31-1.48
Jiang *et al*. [131]	2.65-2.83	0.3-0.5	1.26
Simi *et al*. [89]	1.8-1.9	___	3.2-3.5
Ayouchi *et al*. [90]	1.85-2.4	___	3.2

3.2.4 van der Pauw measurement

Van der Pauw measurements were performed on several films, and the resistivity, carrier density, and the Hall mobility are presented in table 3-2. The resistivity of the Zn_3N_2 films is in the 0.004-0.006 Ω cm range. The carrier density is relatively low compared to the literature [28]. The mobility of the single crystal films on the sapphire substrates is ~100 cm^2 /Vs, which is lower than the mobility of the films on MgO substrates (~200 cm^2 /Vs). This result is consistent with discussion related to figure 3-2 and figure 3-3 namely that the structural order in the films grown on the MgO substrates is better than that of the films grown on the sapphire substrates. I also found a record high mobility of 395 cm^2 /Vs on a fresh 450 nm Zn_3N_2 film. The possible reason for the unintentional n-type conductivity is that nitrogen vacancies as the dominant donorlike native point defects in Zn_3N_2 films. The transport measurements are summarized in Table 3-2. The carrier density in this work is close to Cao's results but less than Suda's report. However, the mobility in this study is higher by approximately a factor of two than in Suda's and Cao's work. The higher mobility in the present samples may be due to the fact that the earlier samples were polycrystalline. There is a general trend towards high mobility with lower carrier concentration (see figure 3-10).

Table 3-2. Electrical transport measurements on several Zn_3N_2 films.

Resistivity (Ω cm)	Carrier density (cm^{-3})	Hall Mobility (cm^2 /Vs)	Thickness /substrate
0.0046	1.17×10^{19}	116	700 nm / Sapphire
0.0052	1.66×10^{19}	72	350 nm / Sapphire

0.0056	4.97×10^{18}	223	200 nm / MgO
0.0042	1.94×10^{18}	76	200 nm / MgO
0.005	5.42×10^{18}	232	400 nm / MgO
0.0058	5.84×10^{18}	185	470 nm / MgO
0.0062	4.28×10^{18}	230	400 nm / MgO
0.0052	3.11×10^{18}	395	450 nm / MgO
0.006	1.05×10^{19}	75	Cao et al. (Sputtering) [132]
--	$1.0\text{-}1.6 \times 10^{20}$	24-156	Suda et al. (MBE) [28]
--	$0.15\text{-}1.6\times 10^{20}$	8-118	Suda et al. (MOCVD) [28]

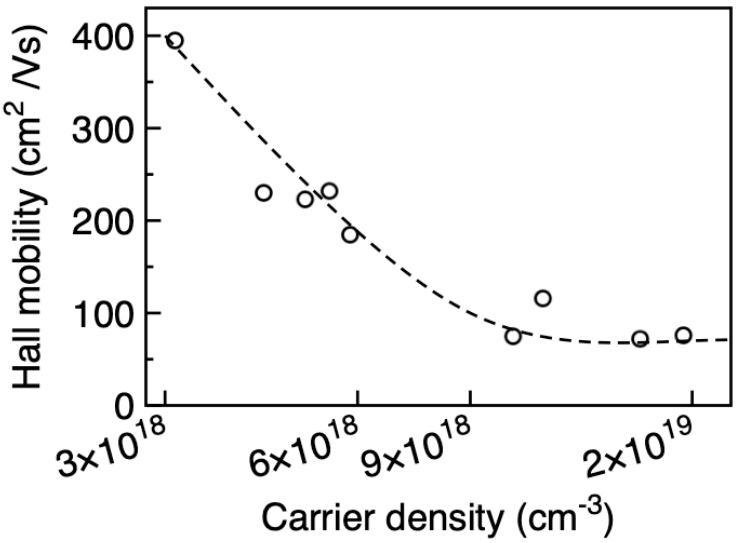

Figure 3-10. Hall mobility as a function of carrier density for Zn_3N_2 films.

Chapter 4 Single crystal Mg_3N_2 thin film growth and optical properties

Mg_3N_2 was first mentioned as a catalyst for the synthesis of cubic BN in 1979 [133][134]. From then on, there are no research articles on Mg_3N_2 until the year 1993: Murata et al. synthesized Mg_3N_2 powder by CVD [135]. The experimental investigation of Mg_3N_2 properties started from 2001 [136]: Toyoura et al. reported the electrochemical formation of Mg_3N_2 films as well as the band gap of 3.15 eV in 2005 [137]; Uenaka et al. presented a significant PL study of Mg_3N_2 in 2014 [138]. In reference [135], Murata et al. also pointed out that the Mg_3N_2 is a moisture sensitive material which makes a deep investigation of its properties challenging. Figure 4-1 shows the time evolution of the oxidation of a 500 nm Mg_3N_2 film which was exposed in air. The 500 nm film is totally oxidized in 30 seconds.

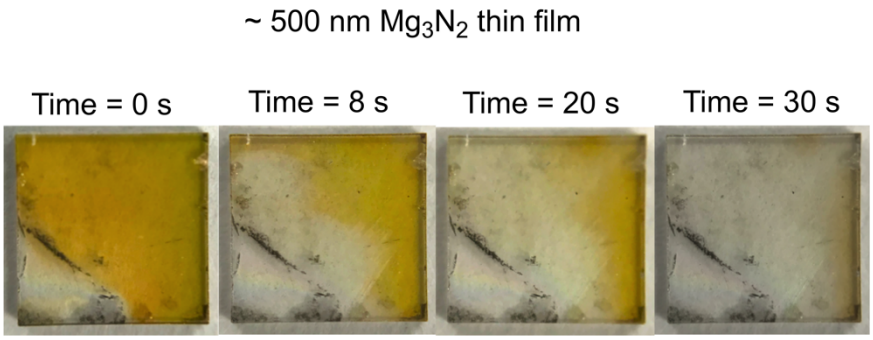

Figure 4-1. Dynamic oxidation of Mg_3N_2 thin film.

To address this issue, I developed a capping procedure in which the Mg_3N_2 film is covered with a protective oxide layer at the end of the plasma assisted MBE growth process, to protect the epilayer against oxidation.

4.1 Mg_3N_2 Thin Film Growth

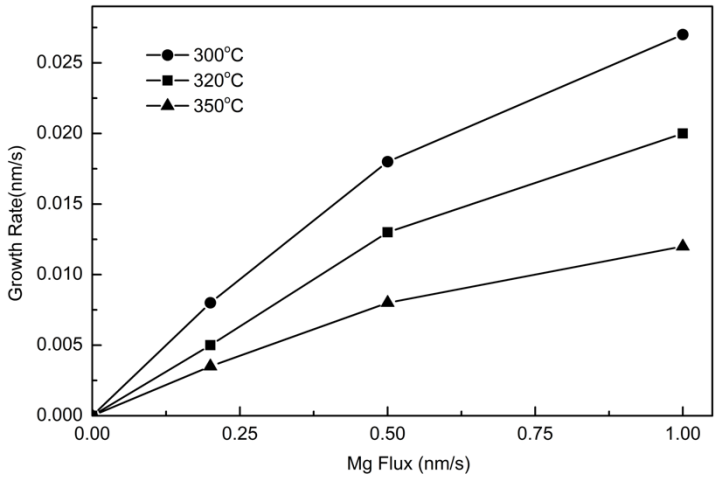

Figure 4-2. The growth rate of the Mg_3N_2 films as a function of substrate temperature.

By using high purity source materials (see table 2-1), I was able to grow the single crystal epitaxial Mg_3N_2 thin films with (100) orientation on (100) MgO substrates by plasma assisted MBE. Commercial MgO substrates were cleaned by annealing at 800°C for 9 hours in air, followed by boiling in acetone and then loaded into the MBE chamber for further outgassing and growth. During growth, high purity (99.9995%) nitrogen gas at a constant pressure of 4×10^{-5} Torr was introduced into the growth chamber through a plasma source energized with 300W of RF power at 13.56 MHz. The Mg source consisted of an effusion cell containing high purity metallic Mg (99.9999%) in a PBN crucible maintained at a constant temperature. Source temperature in the 360 °C to 390 °C range give Mg fluxes in the 0.3-1.0 nm s^{-1} range (in figure 2-10). Figure 4-2 shows the growth rate as a function of the Mg flux and substrate temperature. The growth rate

decreases with increasing substrate temperature from 300°C to 350°C at the same Mg flux, presumably due to re-evaporation of Mg from the substrate. When the Mg flux is low, the surface is nitrogen rich and the growth rate is limited by Mg availability. At high Mg fluxes, above approximately 0.5 nm s^{-1}, the growth rate tends to saturate and is limited by the reactive nitrogen flux which is constant in our experiments.

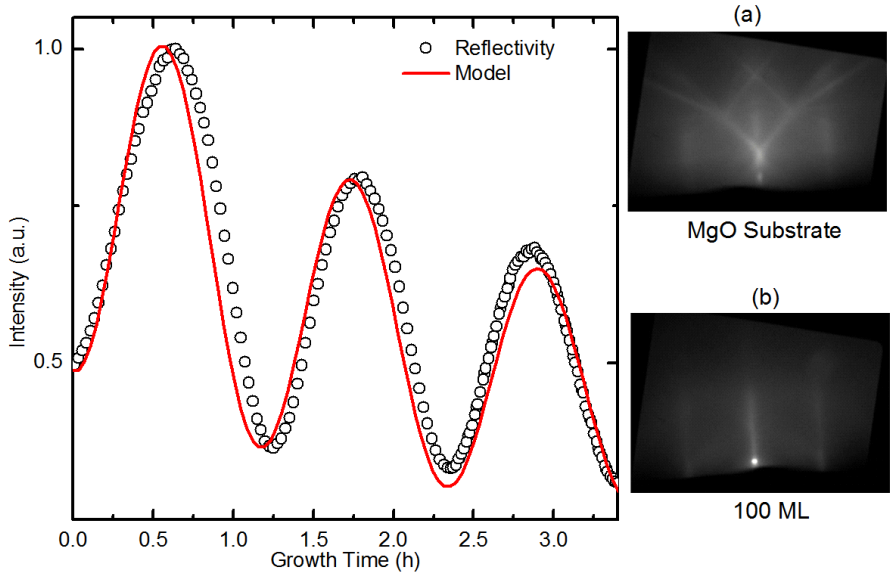

Figure 4-3. In-situ specular reflectivity at 488 nm of a Mg_3N_2 film. The calculated reflectivity (red line) is a best fit to the experimental spectrum (black circles) as discussed in the text. Insets a) and b) are the RHEED patterns for a bare MgO (100) substrate and a Mg_3N_2 film grown on a MgO substrate, respectively.

The surface of the film was monitored *in situ* by reflection high-energy electron diffraction (RHEED). Insets (a) and (b) in figure 4-3 show the RHEED patterns for the bare MgO substrate and a growing film, respectively. The electron beam is incident along the[110] direction of the MgO substrate, which is parallel to the edge of the square

substrates. When the growth of Mg_3N_2 starts on MgO, the Kikuchi lines change to a weak and diffuse background. After about 100 monolayers have been deposited (1 ML ≈ 0.53 nm) the RHEED pattern in figure 4-3 (b) shows sharp streaks indicating that the crystallographic planes of the deposited Mg_3N_2 film are aligned with the substrate lattice planes as expected in the case of epitaxial growth of single crystal films. The RHEED pattern of the deposited films was measured with the nitrogen gas flow turned off and the Mg shutter closed in order to reduce the chamber pressure below 10^{-7} Torr.

The growth rate was measured optically by specular reflection of a laser with wavelength 488 nm. Figure 4-3 shows both the specular and calculated reflectance at 488 nm as a function of time during film growth. As the thickness of the film increases, the amplitude of the interference oscillation decreases slightly indicating that the film either has a weak absorption at 488 nm or there is increasing surface roughness scattering. In addition, the magnitude of the reflectance gradually decreases with time, which indicates that the surface roughens during growth. The optical reflectance equation (2-9) was used to fit the experimental reflectivity data in figure 4-3 with a refractive index $n = 2.4$, an extinction coefficient $k = 0.08 \pm 0.01$ (absorption coefficient $\alpha = (2.05 \pm 0.25)\times10^4$ cm^{-1}), and a growth rate of 0.025 nm/s. In the optical model in figure 4-3 I multiplied the calculated reflectivity with a decaying exponential, $e^{-0.37t}$ with growth time t is measured in hours, to model the decrease in reflectivity associated with the increase in surface roughness scattering.

The as-grown films are yellow and air sensitive, converting spontaneously to $Mg(OH)_2$ and NH_3 in ambient air. Thereafter, the films were capped with a thin MgO layer about 10 nm thick, deposited in the MBE chamber by oxygen plasma MBE, and

then further coated by electron beam evaporation with a secondary CaF_2 layer after the samples were taken out of the MBE chamber. The capped samples are much less sensitive to air exposure for measurement and storage.

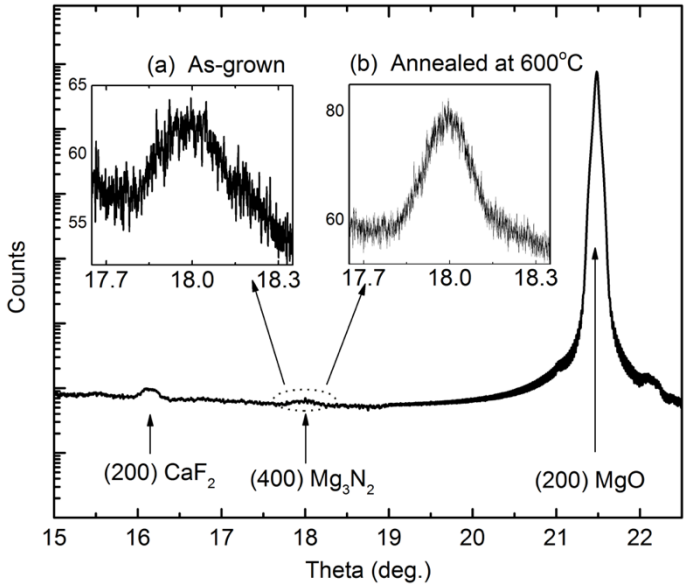

Figure 4-4. High resolution XRD θ-2θ scans for 800 nm Mg_3N_2 film on MgO substrates. The inset (a) is the epilayer peak and (b) is the epilayer peak annealed at 600°C for 1 min.

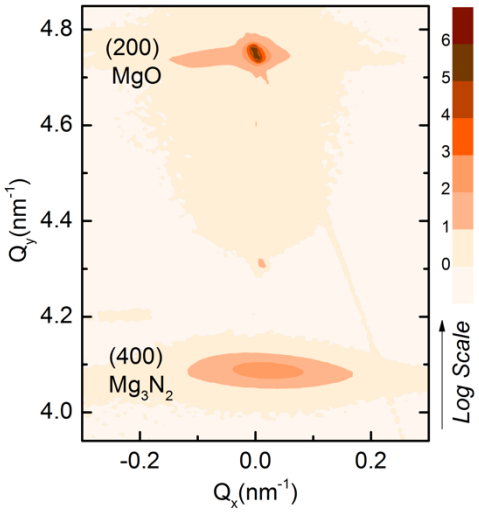

Figure 4-5. Reciprocal space map for a 800 nm Mg_3N_2 film on a MgO substrate.

4.2 Properties of Mg_3N_2 Films

4.2.1 X-Ray Diffraction

The structure of the Mg_3N_2 films was investigated by high resolution x-ray diffraction (HRXRD) with Cu K_α radiation. An x-ray θ-2θ scan is shown in figure 4-4 for an 800 nm Mg_3N_2 layer capped with 50 nm of MgO and 400 nm of CaF_2. This scan shows a strong (200) peak from the MgO substrate, and weak (400) and (200) peaks from the Mg_3N_2 film and the CaF_2 capping layers respectively. There is no indication of any other phases or crystal orientations. A zoom-in image of the Mg_3N_2 (400) peak is presented in the inset (a) in figure 4-4. After annealing in vacuum at 600 °C for 1 minute, the intensity of the (400) Mg_3N_2 peak increased by approximately a factor of three, and the width of the peak decreased indicating improved structural ordering following the anneal. The (400) Mg_3N_2

peak has a lower intensity than the (200) CaF_2 peak due to the smaller structure factor associated with the lighter elements making up Mg_3N_2. The intensity of the (200) CaF_2 and (400) Mg_3N_2 peaks, $I = |F(hkl)|^2$, were calculated from the structure factor $F(hkl) = \sum_{j=1}^{N} f e^{i2\pi(hx+ky+lz)}$, where f is the scattering factor (f_{Mg}=6.77, f_{Ca}=12.15, f_F=2, and f_N=2.85) [139][140], N is the number of atoms in the unit cell, (hkl) is a reciprocal lattice vector, and (xyz) is the coordinate of the j^{th} atom. The calculated intensities of the (200) CaF_2 and (400) Mg_3N_2 peaks are 8091 and 2662, respectively. The intensity of CaF_2 is higher by a factor of 3.8 than Mg_3N_2, in good agreement with the experimental data in figure 4-4.

Figure 4-5 shows a reciprocal space map of the Mg_3N_2 (400) and MgO (200) peaks. Q_x and Q_y refer to the in-plane and out-of-plane directions, respectively. The epilayer peak has a smaller Q_y value than the MgO substrate as in the θ-2θ scan. The Mg_3N_2 (400) peak in the inset is vertically aligned with the substrate peak indicating that the (400) planes are parallel with the substrate lattice planes. XRD data was also obtained for four Mg_3N_2 films with thicknesses of 180, 250, 450 and 800 nm. In the case of the thinner films, the Mg_3N_2 peak is barely detectable due to the weak diffraction intensity from the light elements Mg and N. For this reason only the data for the 800 nm film is presented here.

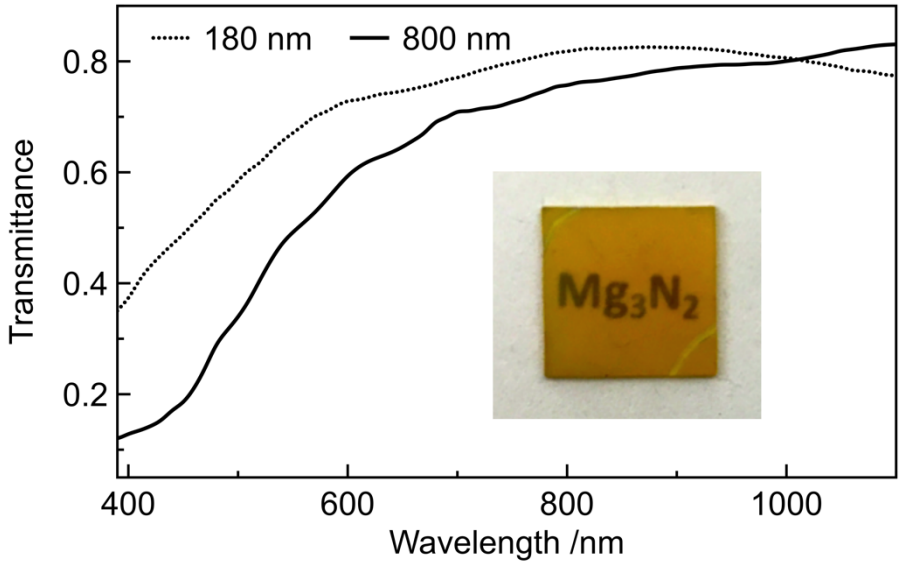

Figure 4-6. Room temperature optical transmission spectra of Mg_3N_2 thin films, with the films thicknesses indicated on the figure. The photograph is an 800 nm thick Mg_3N_2 sample on a piece of paper with the chemical formula printed on it.

4.2.2 Optical Transmission Measurements

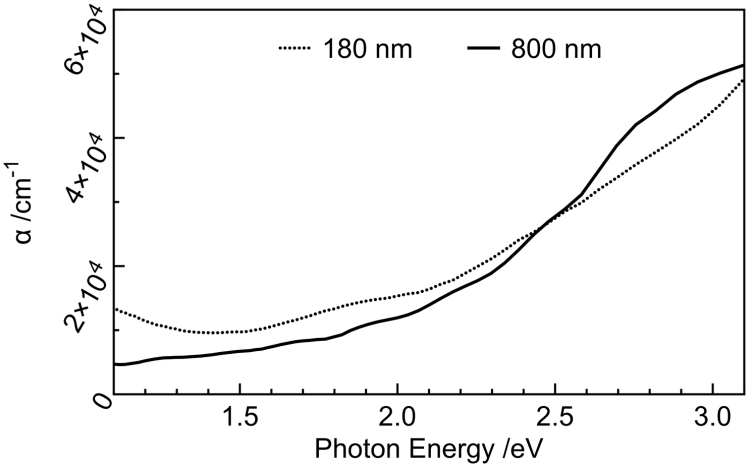

Figure 4-7. Absorption coefficient α as a function of photon energy for the same Mg_3N_2 thin films as in figure 4-6.

Optical transmission measurements were performed at room temperature on the capped Mg_3N_2 thin films. The samples were illuminated at normal incidence with monochromatic light from a chopped monochromatized tungsten-halogen lamp and a long pass filter to block the second order light. The transmitted light was detected using a Si photodetector which is connected to the lock-in amplifier. The samples were placed up against the detector in order to maximize the collection of specular and scattered light. The transmission spectrum of the Mg_3N_2 layer was obtained by dividing the signal transmitted through the sample by the transmission spectrum of an uncoated MgO substrate. Figure 4-6 shows the transmission spectra for two Mg_3N_2 films, one 180 nm thick, the other 800 nm thick. Weak interference oscillations are barely visible in both samples. The oscillations are weak due to the anti-reflection properties of the CaF_2 capping layer which has a lower index of refraction of 1.43. The samples begin to absorb at wavelengths below about 550 nm and the transmittance of the 180 nm film is higher than the thicker 800 nm film in the absorbing region as expected. The inset is a photograph of a Mg_3N_2 film showing the yellow color and easy visibility of the printed formula on the paper behind the film.

The optical absorption coefficient α and the bandgap E_g can be determined from the transmission data. The absorption coefficient is given by $-\frac{1}{d}\ln\left(\frac{1-R}{T}\right)$ where d is the layer thickness, T is the transmittance as a function of photon energy and R is the reflectivity was ignored in this case. Figure 4-7 shows the absorption spectra of the as-grown Mg_3N_2 films in the energy range 1.1-3.1 eV derived from the transmission data. According to band structure calculations [61][141][142], Mg_3N_2 has a direct bandgap, therefore I expect the absorption coefficient to have the following dependence on photon

energy hv: $(\alpha hv)^2 = C\,(h\nu - E_g)$, for photon energies just above the bandgap, where C is a constant. A plot of $(\alpha hv)^2$ versus photon energy will extrapolate linearly to zero at the bandgap energy, E_g.

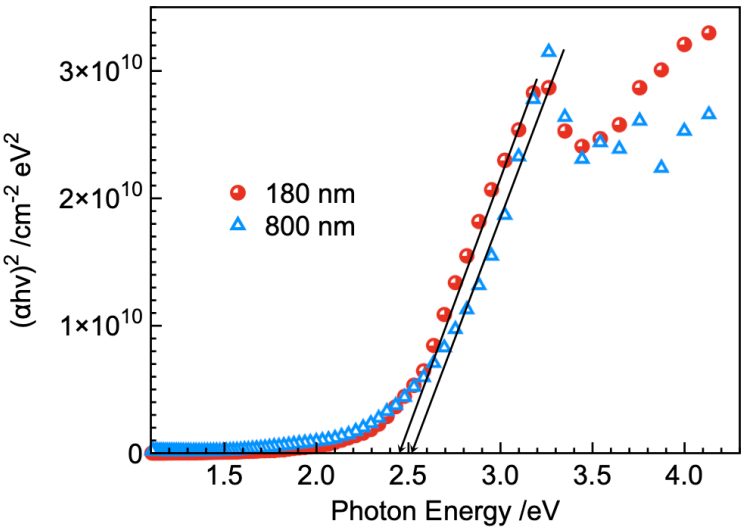

Figure 4-8. Tauc plot of $(\alpha hv)^2$ versus photon energy, which is used to determine the optical bandgap.

Figure 4-8 shows how this extrapolation of the experimental data can be used to determine the bandgap, which is found to be 2.46 and 2.50 eV for the 800 nm thick sample and the 180 nm thick sample, respectively. These bandgap values are less than the bandgap of 2.8-3.15 eV inferred for Mg_3N_2 powders from PL [138], and optical absorption obtained by the Kubelka-Munk method [137]. The reason for the difference in the bandgap reported here and the earlier results is not known, but could be caused by the different measurement techniques used or by a difference in material composition or structure. High pressure phases of Mg_3N_2 with lower bandgaps than the anti-bixbyite structure have been studied experimentally and theoretically [86][143][144]. The high-

pressure phase is unstable and transforms spontaneously back to the usual structure at ambient pressure.

4.2.3 Spectroscopic Ellipsometry Measurements

Spectroscopic ellipsometry measurements were carried out at room temperature with a J. A. Woollam Company Alpha-SE ellipsometer in the spectral range 0.38-0.9 μm in order to obtain the refractive index and extinction coefficient for Mg_3N_2. The angle of incidence relative to the surface normal was 70°, and the amplitude ratio Ψ and phase difference Δ for Mg_3N_2 layers in the 0.38-0.9 μm wavelength range was obtained with the ellipsometer. The Ψ and Δ parameters were used to calculate the refractive index, *n,* and extinction coefficient, *k,* as a function of wavelength. The Ψ (open circles) and Δ (open squares) parameters are well fitted by equation (2-29) as shown in figure 4-9.

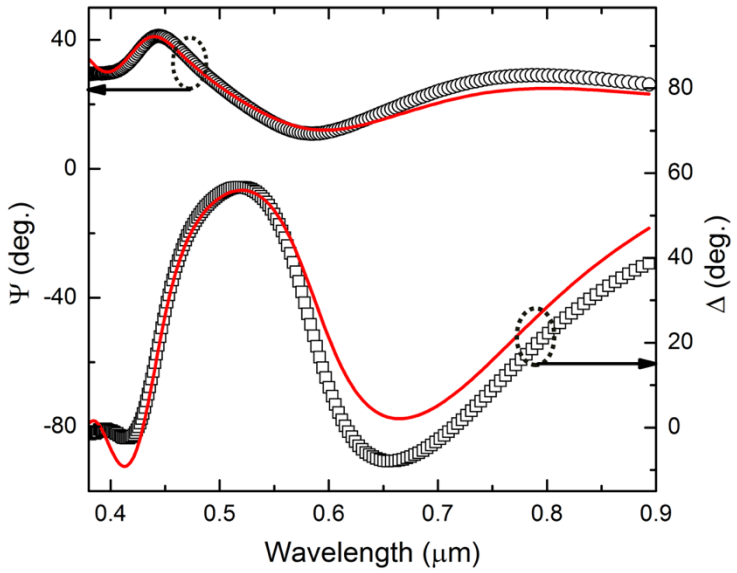

Figure 4-9. The experimental Ψ (open circle) and Δ (open square) of the thin film, respectively, and the data was fitted by equation (2-29) (red line).

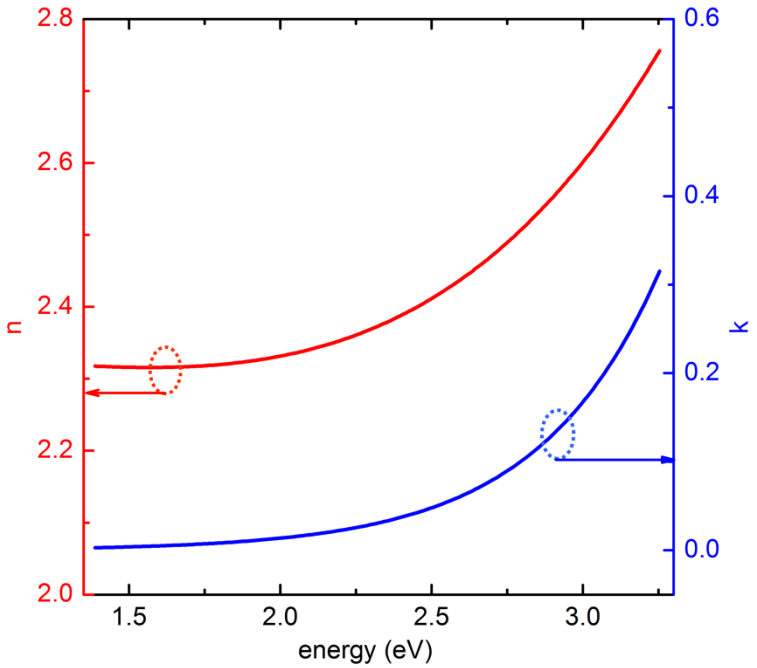

Figure 4-10. Optical constants of a Mg_3N_2 thin film as a function of photon energy, obtained from ellipsometry measurements.

Figure 4-10 shows the real and imaginary parts of the refractive index, *n* and *k,* derived from the ellipsometry data. The real part of the refractive index of single crystal Mg_3N_2 films increases from 2.3 to 2.75 over the energy range 1.4-3.2 eV. The refractive index *n* at the photon energy 2.54 eV is 2.4, in agreement with the *in-situ* results in figure 4-3. The extinction coefficient from the ellipsometry data is 0.0524 at the same energy, reasonably close to the extinction coefficient of 0.08±0.01 obtained from the *in-situ* measurements.

Because of the moisture sensitivity of Mg_3N_2, Hall measurements are challenging. My proposal for addressing this issue will be presented in chapter 6.

Chapter 5 Bandgap Tunable $Zn_{3-3x}Mg_{3x}N_2$ Alloys

In this chapter, the bandgap tunability of the novel $Zn_{3-3x}Mg_{3x}N_2$ alloy system is described. I show that E_g can be tuned from 1.2 eV to 2.1 eV by varying x from 0-0.59: the ideal E_g value of 1.4 eV for photovoltaic devices was obtained at $x = 0.18$. Furthermore, n-type $Zn_{3-3x}Mg_{3x}N_2$ with $x = 0.18$ was found to exhibit an electron mobility as high as 46.7 $cm^2 V^{-1} s^{-1}$. These results suggest that $Zn_{3-3x}Mg_{3x}N_2$ is an attractive candidate for an earth-abundant photovoltaic absorber material.

5.1 Sputtering Growth

$Zn_{3-3x}Mg_{3x}N_2$ epitaxial films were grown on yttria stabilized zirconia (YSZ) (100) single crystal substrates heated at ~140 ºC by reactive sputtering in a sputter-deposition system equipped with two RF cathodes one for Zn and another for Mg. The Mg content (x) was controlled by varying RF power (0-40 W) applied to each cathode. The growth was conducted in a 1:4 mixture of Ar and N_2 gas, at a total pressure of ~0.015 Torr. A base pressure less than 4×10^{-8} Torr was established, prior to film growth. Although I grew Mg_3N_2 films, Mg_3N_2 was so reactive with water vapor in air that the as-grown films immediately oxidized when the films were exposed to air. Accordingly, Mg-rich films are also expected to be unstable in air. Thus, I focused on the relatively air-stable $Zn_{3-3x}Mg_{3x}N_2$ layers with $x < 0.6$.

5.2 Properties of $Zn_{3-3x}Mg_{3x}N_2$ Alloys

5.2.1 X-Ray Photoelectron Spectroscopy

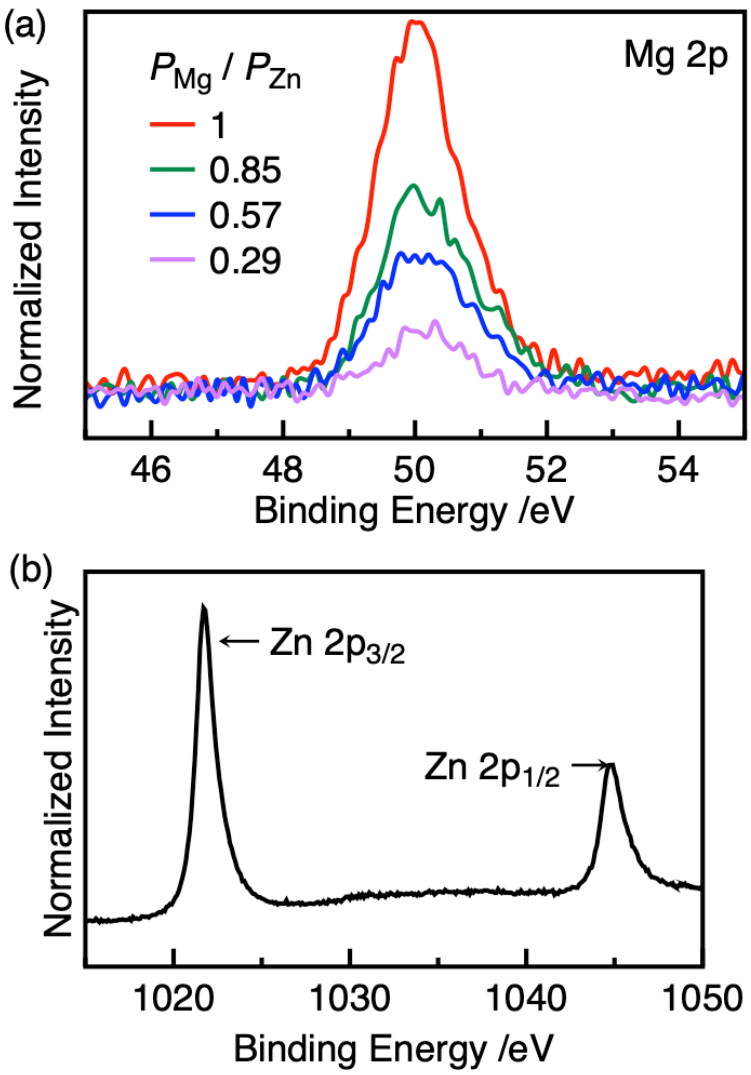

Figure 5-1. (a) XPS Mg 2p spectra of $Zn_{3-3x}Mg_{3x}N_2$ films grown at various P_{Mg} / P_{Zn}, and (b) XPS Zn 2p spectra of $Zn_{3-3x}Mg_{3x}N_2$ films grown at P_{Mg} / P_{Zn} =1.

X-ray photoelectron spectroscopy (XPS) using monochromated Al Kα radiation (PHI Versa Probe) was employed for examining the concentration of Mg and oxygen in the films. XPS is a surface sensitive technique because only those electrons generated near

the surface escape and are detected. The photoelectrons of interest have relatively low kinetic energy. Due to inelastic collisions within the sample's atomic structure, photoelectrons originating more than 2-5 nm below the surface cannot escape with sufficient energy to be detected.

The elemental composition was determined using X-ray photoelectron spectroscopy (XPS): the measurements were done on a sampled depth of 20 nm surface. Figure 5-1 shows the Mg 2p spectra of the $Zn_{3-3x}Mg_{3x}N_2$ films grown at different P_{Mg} / P_{Zn}, where P_{Mg} and P_{Zn} represent the target power of Mg and Zn, respectively. The Mg *2p* peak assigned to $Zn_{3-3x}Mg_{3x}N_2$ alloys appeared at ~50 eV which is in good agreement with those reported literature, such as Mg, Mg_2Cu, Mg_3Bi_2, MgF_2, $Mg(OH)_2$, and $MgAl_2O$. The spectra were normalized to the peak intensities of the Zn $2p_{3/2}$ peaks. The intensity of Mg 2p peak increased in parallel with the increase in P_{Mg} / P_{Zn}, implying the increase in x. Hence, I estimated x values using the relative sensitivity factor (RSF) method (equation (2-37)). Figure 5-2 shows the Mg content x in the as-grown films versus the ratio of rf powers applied to the targets, P_{Mg} / P_{Zn}. The applied rf power on the Mg target range from 15 W to 30 W, and the power on the Zn target varied from 30 W to 40 W. The Mg content in the epilayers increased linearly with the rf power ratio.

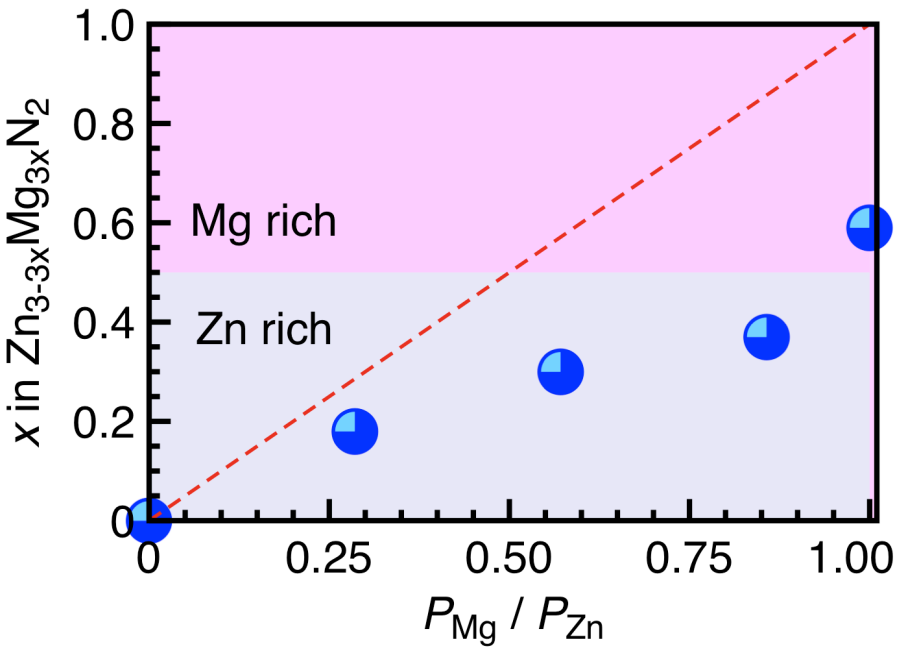

Figure 5-2. Mg content (x) in $Zn_{3-3x}Mg_{3x}N_2$ films as a function of P_{Mg} / P_{Zn}. The red dashed line represents the relationship $x = P_{Mg} / P_{Zn}$ for reference.

Unintentional oxygen incorporation into sputtering Zn_3N_2 thin films has frequently been reported so far [78]. The incorporated oxygen comes from water vapor in the residual gas present in the sputtering growth chamber. Similar to the previous reports, oxygen was detected in the $Zn_{3-3x}Mg_{3x}N_2$ layer in this study. Typical O 1s core spectrum is shown in Figure 5-3. This suggested that the nitrogen sublattice in the surface of the $Zn_{3-3x}Mg_{3x}N_2$ films was partially substituted by ~20% oxygen. The substitutional oxygen has been known to act as an electron donor. The unintentional oxygen incorporation brought n-type conductivity in the $Zn_{3-3x}Mg_{3x}N_2$ films as discussed later.

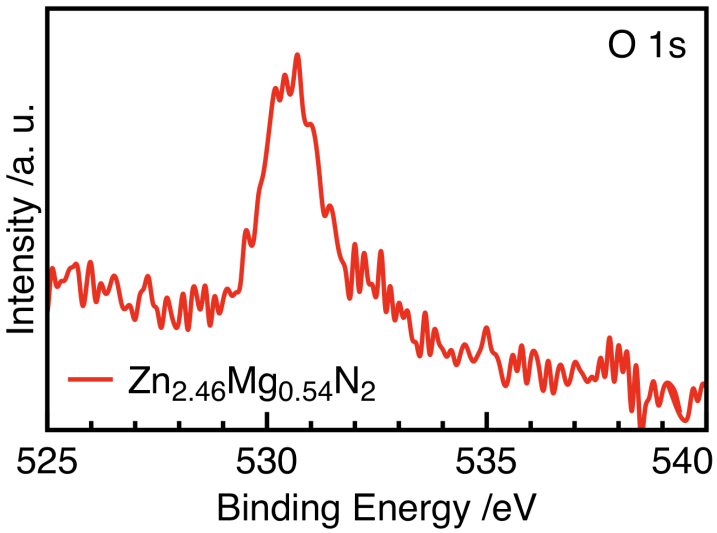

Figure 5-3. XPS O 1s spectrum of $Zn_{2.46}Mg_{0.54}N_2$.

5.2.2 XRD

A high-resolution X-ray diffractometer (Rigaku ATX-G) with Cu Kα radiation was employed to perform out-of-plane (θ-2θ) scans to evaluate the film structure. X-ray diffraction (XRD) analysis verified the growth of (001)-oriented single-phase epilayers having the anti-bixbyite structure regardless of x. The θ–2θ XRD patterns of the $Zn_{3-3x}Mg_{3x}N_2$ epilayers with x = 0, 0.18, 0.30, 0.37 and 0.59 are shown in Figure 5-4. For the $Zn_{3-3x}Mg_{3x}N_2$ with $x \leq 0.3$, <100>-oriented films were epitaxially grown. In contrast, no obvious diffraction peak from the films was detected for the $Zn_{3-3x}Mg_{3x}N_2$ with $x \geq 0.37$. The possible reason for this phenomenon is the degradation of the crystallinity with increasing x. The encapsulation layers which can prevent this degradation were not grown on top of alloys for the reason of the following Hall measurements.

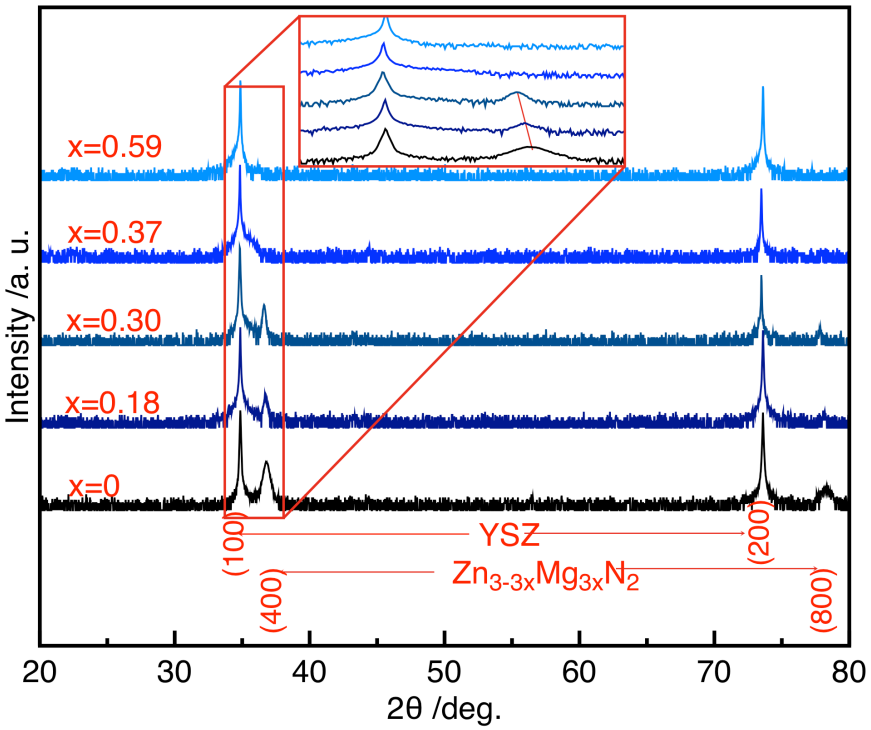

Figure 5-4. θ-2θ X-ray diffraction patterns of $Zn_{3-3x}Mg_{3x}N_2$ films on YSZ (100) substrates with different x values. The inset is a magnified view in the vicinity of 2θ = 33–38º.

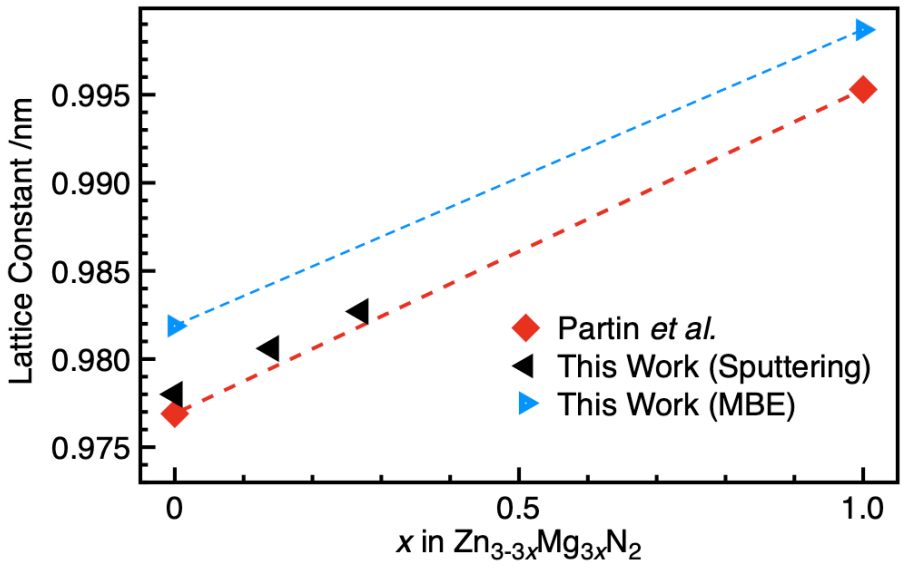

Figure 5-5. *x* dependence of the lattice constant of $Zn_{3-3x}Mg_{3x}N_2$ films.

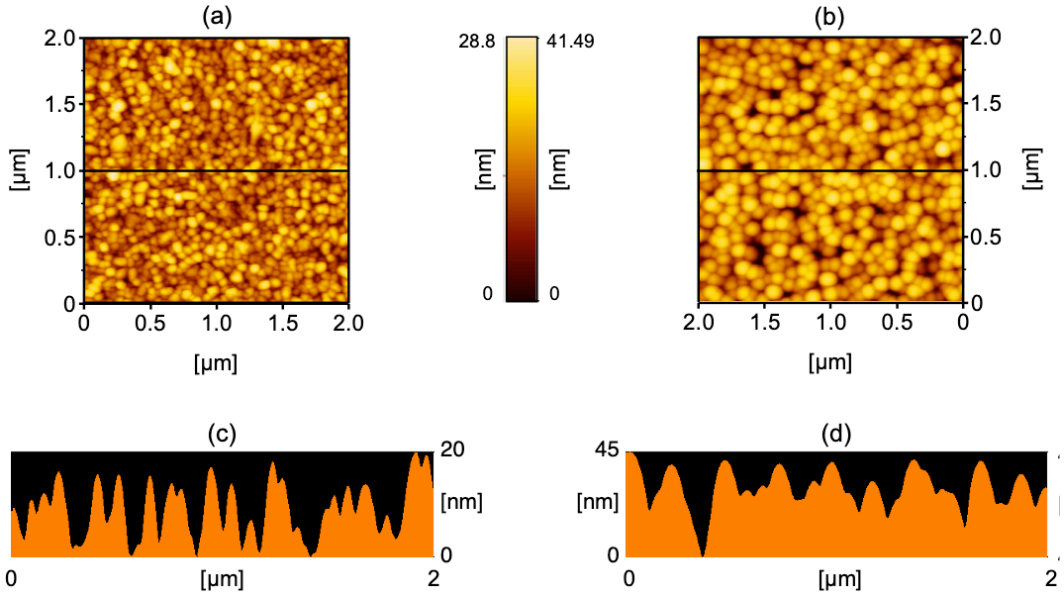

Figure 5-6. Atomic force microscopy topographic images of the surface of (a) Zn_3N_2 and (b) $Zn_{2.46}Mg_{0.54}N_2$ films. Cross-sectional views along the measurement lines in parts (a) and (b) are shown in parts (c) and (d), respectively.

The lattice constants (a) calculated from the 2θ angles of the 001 and 004 reflections are plotted as a function of x in Figure 5-5. The value of lattice constants a systematically increased from 0.978 nm at $x = 0$ to 0.9827 nm at $x = 0.3$, obeying the Vegard's law. The lattice expands with increasing x, consistent with the substitution of Mg for Zn, because the bond length of Mg-N in the Mg_3N_2 structure are larger than that in Zn_3N_2 [20]. The reason of the MBE films shown the relative larger lattice constants than those of the sputtered films is unknown. Unlike conventional semiconductors in which smaller lattice constants correspond to larger bandgaps, Mg_3N_2 shows a larger bandgap with a larger lattice constant compared with Zn_3N_2. Figure 5-7 summarises the bandgap of variety of nitrides as a function of lattice constant. Because of the weak structure factor of (400)

Mg_3N_2, the intensity of the epilayer peaks decreases with increasing *x*. The structure factors of (400) Mg_3N_2 and (400) Zn_3N_2 were calculated using the scattering factors of Mg and Zn at the x-ray energy (Appendix A). The theoretical intensity of (400) Zn_3N_2 is higher than that of Mg_3N_2 by a factor of 8. This result confirms that the higher the Mg concentration, the weaker the diffractive peak is. Atomic force microscopy (AFM) was performed on selected sputtered Zn_3N_2 and $Zn_{2.46}Mg_{0.54}N_2$ films (see figure 5-6). AFM observations suggest that the Zn_3N_2 and $Zn_{0.246}Mg_{0.54}N_2$ have a columnar morphology with column widths of 100 nm and 200 nm, respectively.

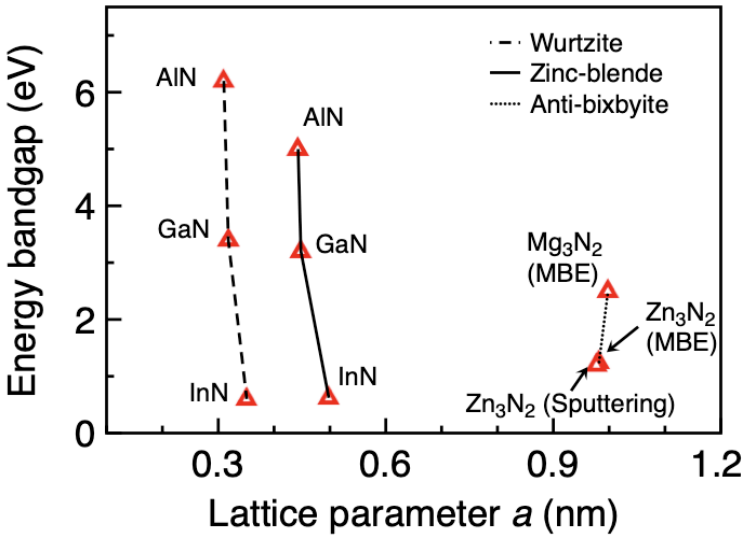

Figure 5-7. Energy bandgap of the nitrides as a function of lattice parameter *a*.

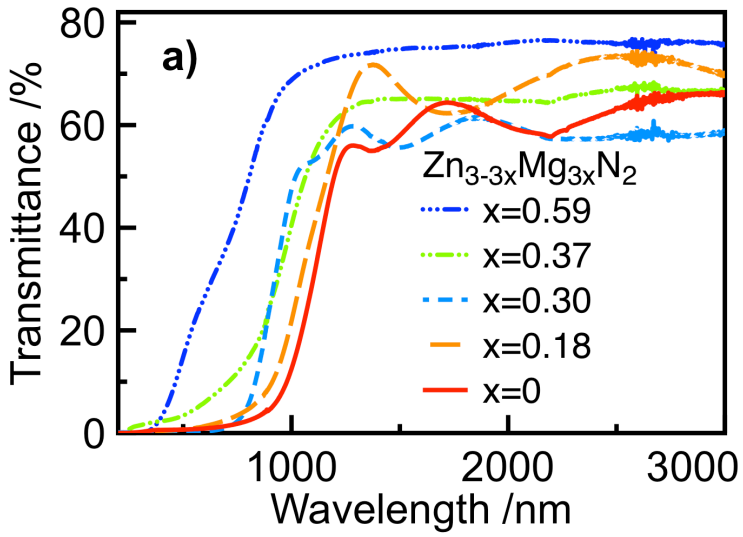

Figure 5-8. Specular transmittance spectra of $Zn_{3-3x}Mg_{3x}N_2$ films for various compositions.

5.3 Optical Measurements

5.3.1 Transmittance and Reflectance

Optical transmittance (T) at normal incidence and reflectance (R) at near-normal incidence (~5º) were collected between 300 and 3200 nm using a UV-Vis-NIR spectrophotometer (Shimadzu UV-3150). Figure 5-8 shows specular transmittance spectra of $Zn_{3-3x}Mg_{3x}N_2$ films in the visible to near-infrared region. As can be clearly seen from this figure, the absorption edge is shifted to shorter wavelengths (higher energy) with increasing x, suggesting an increase in E_g. As a result, the transmittance in the visible region is increased as the Mg content increases. Figure 5-9 shows the reflectance spectra of $Zn_{3-3x}Mg_{3x}N_2$ films with various x. The reflectance of the $Zn_{3-3x}Mg_{3x}N_2$ films was < 35% in the range of 300-3200 nm.

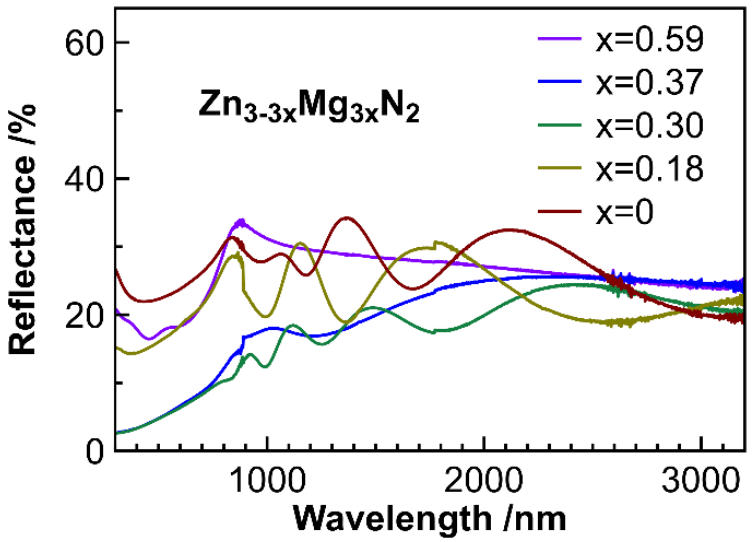

Figure 5-9. Reflectance spectra of $Zn_{3-3x}Mg_{3x}N_2$ films for various compositions.

5.3.2 Absorption coefficient

The optical absorption coefficient α and the bandgap E_g can be determined from the transmission data. The absorption coefficient α is given by $-\frac{1}{d}\ln\left(\frac{1-R}{T}\right)$ where d is the layer thickness, T is the transmittance and R is the reflectance. The absorption coefficient as a function of wavelength for $Zn_{3-3x}Mg_{3x}N_2$ with $x = 0.18$ ($E_g = 1.4$ eV) as well as the air-mass 1.5 solar spectrum are plotted in Figure 5-10. The absorption onset appears at the wavelength (λ) of ~890 nm (photon energy of $h\nu \approx 1.4$ eV), and α increases as λ becomes shorter ($h\nu$ becomes higher). Moreover, α is as high as 5×10^4 cm^{-1} at the bandgap, and thus the film can sufficiently absorb light even if the film is thin. Such a sharp absorption onset and high α are desirable properties for a photovoltaic absorber material. These desirable properties originate in the direct transition at the bandgap in $Zn_{3-3x}Mg_{3x}N_2$.

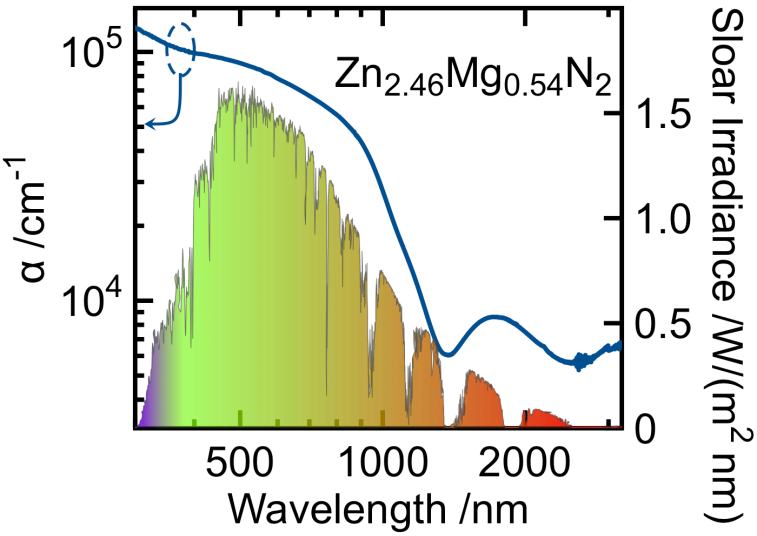

Figure 5-10. Absorption spectrum of $Zn_{2.46}Mg_{0.54}N_2$ film with E_g = 1.4 eV and air-mass 1.5 solar spectrum.

5.3.3 Optical Bandgap

Assuming that $Zn_{3-3x}Mg_{3x}N_2$ has a direct bandgap, the absorption coefficient has the following dependence on photon energy hv, $(\alpha hv)^2 = C\,(hv - E_g)$, for photon energies just above the bandgap, where C is a constant. A plot of $(\alpha hv)^2$ versus photon energy will extrapolate linearly to zero at the bandgap energy, E_g. Figure 5-11 shows how this extrapolation of the experimental data can be used to determine the bandgap, which is found to be 1.2 eV, 1.4 eV, 1.5 eV, 1.7 eV and 2.1 eV corresponding to x = 0, 0.18, 0.30, 0.37, and 0.59, respectively.

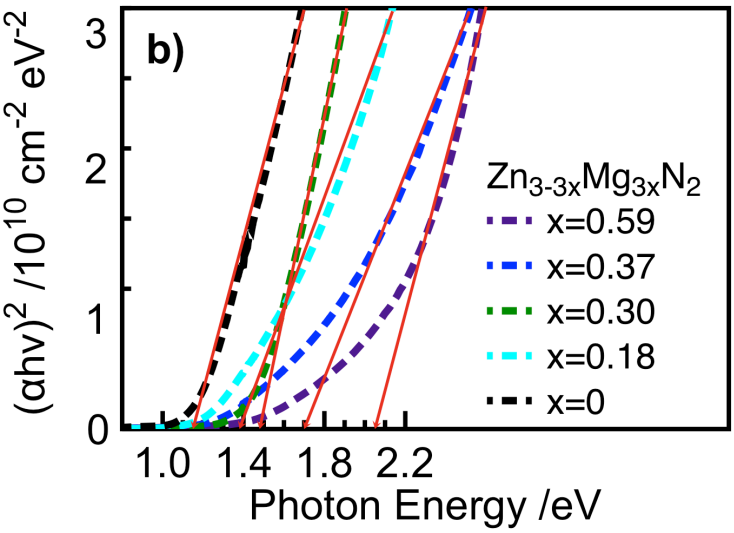

Figure 5-11. Tauc plots for $Zn_{3-3x}Mg_{3x}N_2$ films with various compositions.

Figure 5-10 shows E_g values of $Zn_{3-3x}Mg_{3x}N_2$ films as a function of x. As suggested in Figure 5-8, E_g monotonically increases from 1.2 eV to 2.1 eV with increasing x. This result clearly demonstrates that the bandgap of the $Zn_{3-3x}Mg_{3x}N_2$ alloy system is tunable over a wide range: $E_g \approx 1.4$ eV, ideal for photovoltaic absorbers, can be obtained at $x = 0.18$. In many semiconductor alloys, bandgap bowing has been reported in which there is a nonlinear relationship between E_g and x. However, the data for the $Zn_{3-3x}Mg_{3x}N_2$ alloy in figure 5-12 shows a linear dependence of bandgap E_g on composition x. Indeed, the bandgap widening can be readily confirmed from the photograph shown in figure 5-12: the black Zn_3N_2 becomes semi-transparent when alloyed with Mg_3N_2.

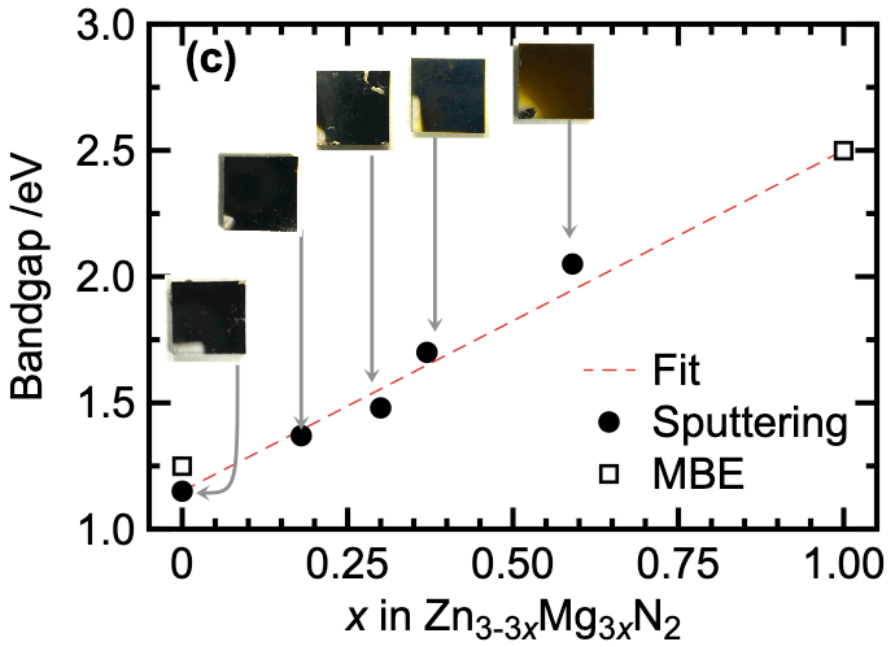

Figure 5-12. Bandgap (E_g) of $Zn_{3-3x}Mg_{3x}N_2$ films as a function of *x*. The closed circles represent the data in this study and the open squares show E_g for plasma assisted MBE Mg_3N_2 and Zn_3N_2 as discussed above. Photographs of $Zn_{3-3x}Mg_{3x}N_2$ films are also presented in the figure.

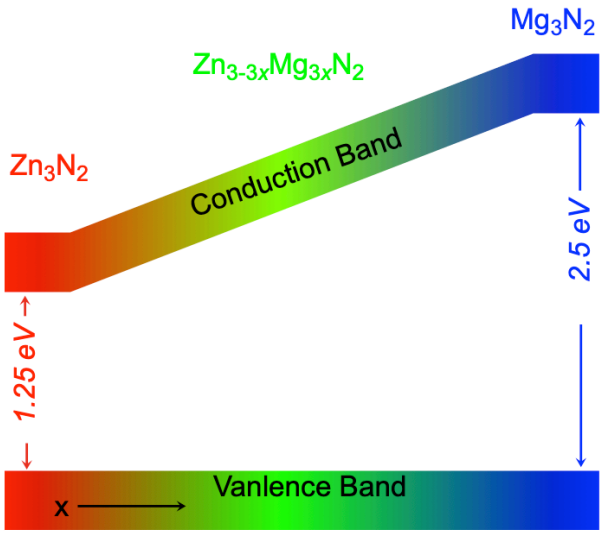

Figure 5-13. Schematic band diagrams of Zn_3N_2, $Zn_{3-3x}Mg_{3x}N_2$ and Mg_3N_2.

In both Zn_3N_2 and Mg_3N_2, the valence-band maxima are mainly composed of N 2*p* states. Accordingly, the valence-band offset between them should be small. Meanwhile, the main component of the conduction-band minimum (CBM) of Zn_3N_2 is the Zn 4*s* state, whereas the Mg 3*s* state chiefly constitutes the CBM of Mg_3N_2. The Mg 3*s* orbital energy is significantly higher than the Zn 4*s* orbital energy, and thus the CBM of Mg_3N_2 should be higher than that of Zn_3N_2. Therefore, I think that the bandgap variation with alloying results mainly from the shift in the position of the conduction band (see figure 5-13). Further study is needed to confirm this explanation.

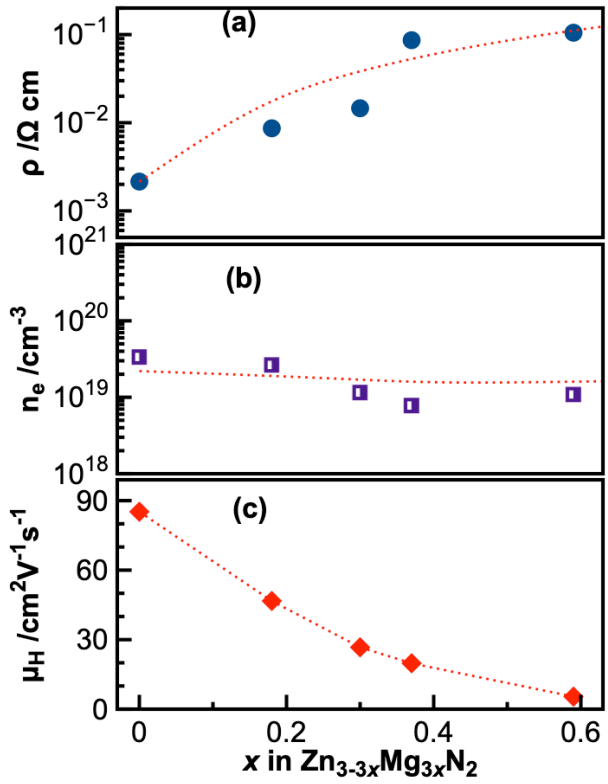

Figure 5-14. (a) Resistivity ρ, (b) electron density n_e, and (c) Hall mobility μ_H of $Zn_{3-3x}Mg_{3x}N_2$ films as a function of the Mg content *x*.

5.4 van de Pauw Measurement

The resistivity (ρ), carrier density (n_e), and hall mobility (μ_H) were determined at room temperature by Hall-effect measurements in the van der Pauw configuration (Toyo Corp. Resistest 8200). The n-type conductivity of $Zn_{3-3x}Mg_{3x}N_2$ mainly originated from nitrogen vacancies or unintentional incorporation of oxygen as mentioned earlier. Figure 5-13 shows the room temperature resistivity ρ, carrier density n_e, and Hall mobility μ_H as a function of the Mg content x in $Zn_{3-3x}Mg_{3x}N_2$. The film has a high conductivity with a resistivity of 10^{-3} Ω cm at $x = 0$ in figure 5-13(a). The resistivity dramatically increased with increasing Mg content to 10^{-1} Ω cm at $x = 0.59$. However, in figure 5-13(b), with increasing Mg concentration, the carrier density of the films did not show much change remaining close to ~10^{19} cm^{-3}. Consequently, the Hall mobility of the as-grown films decreases rapidly from 87 cm^2 $V^{-1}s^{-1}$ at $x = 0$ to 5.4 cm^2 $V^{-1}s^{-1}$ at $x = 0.59$. The decrease in mobility is probably due to cation-disorder scattering associated with alloying and/or to the degradation of crystallinity with increasing x. The film with the bandgap tuned to 1.4 eV still shows a mobility as high as 46.7 cm^2 $V^{-1}s^{-1}$.

Table 5-1 is a brief comparison of Hall measurements for Zn_3N_2 thin films. The mobility of the MBE film is higher than that of the polycrystalline sputtered film, possibly may result from defects such as N vacancies or oxygen contaminations.

Table 5-1. Hall measurement of Zn_3N_2 thin films

Material	Technique	Resistivity (Ω cm)	Carrier density (cm^{-3})	Hall Mobility (cm^2 /Vs)
Zn_3N_2	Sputtering	0.0025	2.50×10^{19}	87
	MBE	0.0052	3.11×10^{18}	395

Chapter 6 Conclusions and Future Work

The most important achievements of this thesis are (1) the demonstration that epitaxial single crystal Zn_3N_2 and Mg_3N_2 thin films can be grown by plasma-assisted MBE, (2) the measurement of the optical and electrical properties of these materials, and (3) that the bandgap of Zn_3N_2-Mg_3N_2 alloys varies linearly with composition.

6.1 Zn_3N_2 and Mg_3N_2

The II_3V_2 semiconductor are a little explored class of semiconductor materials which can be composed of environmentally-benign, earth-abundant elements, and have bandgaps in the visible and near infrared part of the spectrum. The crystal structure of these materials is relatively complex consisting of three interpenetrating fcc lattices, with one of the lattices half occupied. Epitaxial Zn_3N_2 and Mg_3N_2 thin films were grown on (110) sapphire and (200) MgO substrates by plasma-assisted molecular beam epitaxy with nitrogen gas. The Mg_3N_2 and Zn_3N_2 films were grown at temperatures of 300-350 ^oC and 140-180 ^oC, respectively. The RHEED pattern during growth and the x-ray $\theta/2\theta$ scans suggest that the films are epitaxial single crystals. In-situ optical reflectivity during growth was used to determine the growth rate as a function of the metal flux and the growth temperature. The in-situ reflectivity was simulated by an optical model from which we derived the growth rate (up to 0.05 nm/s) and the indices of refraction of the deposited Mg_3N_2 and Zn_3N_2 films at 488 nm (2.4 and 2.65 respectively). X-ray diffraction shows that the thin films were (400) oriented on both the (110) sapphire (Zn_3N_2 only) and (200) MgO substrates. The optical absorption coefficient was calculated

from the transmittance spectrum; the optical band gap of the Mg_3N_2 and Zn_3N_2 thin films were found to be 1.25 eV and 2.5 eV, respectively. Ellipsometry measurements show that the refractive index of Zn_3N_2 is 2.7 at the energy of 1.5 eV and gradually decreases to 2.3 with the energy increase to 3.1 eV, and the extinction coefficient increases from 0.5 to 0.7 in the energy range of 1.5-3.1 eV. The index of refraction of Zn_3N_2 has the unusual characteristic of decreasing with photon energy in the 1.5-3.1 eV range, whereas the index of Mg_3N_2 shows a normal dispersion with photon energy. The electron transport measurements show that the single crystal Zn_3N_2 has an electron mobility as high as 395 cm^2 /Vs, possibly due to Zn_3N_2 band structure with lager conduction band and no upper valleys. Both materials are air sensitive and uncapped films oxidize in room air, especially Mg_3N_2 films which oxidize fully in minutes. PL of the single crystal Mg_3N_2 and Zn_3N_2 films was not detected either at room or low temperature. The PL of Zn_3N_2 powder reveals that the optical band gap is ~ 1.1 eV [129].

6.2 Zn_3N_2-Mg_3N_2 alloy

$Zn_{3-3x}Mg_{3x}N_2$ layers were grown on the (100) plane of yttria-stabilized zirconia (YSZ) single-crystalline substrates by reactive co-sputtering from Zn and Mg targets. The elemental composition was determined by XPS with the relative sensitivity factor method. The Mg content in the $Zn_{3-3x}Mg_{3x}N_2$ layers linearly increased with increasing P_{Mg} / P_{Zn}, as expected. For the $Zn_{3-3x}Mg_{3x}N_2$ with $x \leq 0.3$, <100>-oriented films were epitaxially grown. In contrast, no obvious diffraction peaks from the films were detected for the $Zn_{3-3x}Mg_{3x}N_2$ with $x \geq 0.37$. There are two possible reasons for this phenomenon. One is the degradation of the crystallinity with increasing x. Maybe, the higher growth temperature is needed for the epitaxial growth of $Zn_{3-3x}Mg_{3x}N_2$ with high Mg content.

Another factor is the small x-ray atomic scattering factor of Mg. The 400 peaks of the films gradually shifted toward lower 2θ angles with increasing x up to 0.30. The value of lattice constant increased from 0.978 nm at $x = 0$ to 0.983 nm at $x = 0.30$, obeying Vegard's law. The AFM observation suggested that these films have a columnar structure with the columnar width of 100-200 nm.

The bandgaps were determined by $(\alpha h\nu)^2$ Tauc plot: E_g = 1.2, 1.4, 1.5, 1.7, and 2.1 eV for x = 0, 0.18, 0.30, 0.37, and 0.59, respectively. This result clearly demonstrated that the bandgap of the $Zn_{3-3x}Mg_{3x}N_2$ alloy system is tunable: $E_g \approx 1.4$ eV an ideal bandgap for photovoltaic absorbers can be obtained at $x = 0.18$. The bandgap of $Zn_{3-3x}Mg_{3x}N_2$ can be tuned linearly by changing x.

The resistivities ρ increased from 2×10^{-3} to 1×10^{-1} Ω cm with increasing x from 0 to 0.59. No obvious x dependence of n_e was observed, whereas there is a significant reduction in μ_H with increasing x, possibly due to alloy scattering. Thus, the positive correlation between ρ and x can be interpreted as a result of the suppression of μ_H with the increase in x. A high μ_H value of 87 $cm^2\ V^{-1}s^{-1}$ was obtained at $x = 0$, but it was suppressed down to 5.4 $cm^2\ V^{-1}s^{-1}$ at $x = 0.59$. However, the $Zn_{3-3x}Mg_{3x}N_2$ film with E_g = 1.4 eV ($x = 0.18$) still had a mobility as high as 47 $cm^2\ V^{-1}s^{-1}$.

6.4 Future Work

This study has shown the growth and basic properties of new semiconductor materials: Zn_3N_2, Mg_3N_2, and their alloys. Further studies are needed in several areas in order to fully examine and overcome the remaining difficulties prior to making devices.

In the case of Zn_3N_2, the connection between electrical properties and deposition conditions is not well understood. The possibility for controlling the microstructure of the thin film during growth, the nature of native defects in thin film, as well as finding ways to avoid undesired oxidation, need to be further explored and overcome. Low temperature characterization methods are other options that can provide more insight. Creating a Zn_3N_2 based solar cell is an obvious goal because the material has a suitable in bandgap and optical absorption.

In the case of Mg_3N_2, there are many possibilities for continuing this work, both from the basic research and technological applications. Firstly, exploring further the MBE growth technique and the anti-oxidation layer would be of interest. Furthermore, the electrical property has not been reported yet. It is a challenge to perform Hall measurements due to the moisture sensitivity of the thin film surface. I proposed the Mg_3N_2 sample preparation for Hall measurement in figure 6-1. After the four small Ohmic contacts are directly made on the substrate, the Mg_3N_2 thin film is grown on the prepared substrate, and then encapsulate the film with capping layer (MgO).

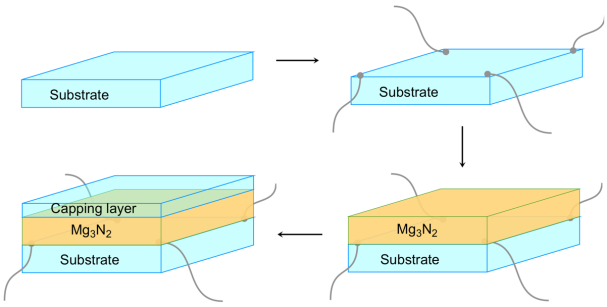

Figure 6-1. Schematic of the sample preparation for Hall measurement.

Ammonia-MBE growth of Zn_3N_2 and Mg_3N_2 thin films is worth exploring. In this system, the ammonia will be used as the N source. The films could be grown at higher temperature (~500^{o}C) using ammonia which may reduce the defect density and improve the structural quality, so that the material may show PL.

Because of the unequal bandgap between Zn_3N_2 and Mg_3N_2, it is worth exploring the heterojunctions and quantum wells of Zn_3N_2/Mg_3N_2 by plasma assisted MBE. Single crystal Zn_3N_2 and Mg_3N_2 thin films can also be grown on alternative substrates (e.g. Si).

In the case of Zn_3N_2-Mg_3N_2 alloys, the electron density n_e values in the present $Zn_{3-3x}Mg_{3x}N_2$ films were on the order of 10^{19} cm^{-3}, which is too high for photovoltaic devices. The high n_e value is attributed to the unintentional incorporation of oxygen or nitrogen vacancies which behave as electron donors. To reduce the electron density, the concentration of the unintentionally incorporated oxygen or nitrogen vacancies must be suppressed. In addition, suppressing the unintentional incorporation of oxygen and defect density will bring the beneficial enhancement of electron mobility as well. Hence, the growth of $Zn_{3-3x}Mg_{3x}N_2$ films with high purity and low defect density is a next challenge toward the developments of this alloy system as a photovoltaic absorber or transistor material. Zn_3N_2-Mg_3N_2 alloys can also be grown by plasma assisted MBE with two effusion cells.

Bibliography

[1] Semiconductor Physics and Devices: Basic Principle (3rd Edition), D. A. Neamen, McGraw-Hill Higher-Education (2003)

[2] Chemistry is Electric, M. E. Bowden, Chemical Heritage Foundation Publication, pp. 38 (1997)

[3] Coherent Light Emission from GaAs Junctions, R. N. Hall, G. E. Fenner, J. D. Kingsley, T. J. Soltys, and R. O. Carlson, Phys. Rev. Lett., 9, 366-369 (1962)

[4] An Introduction to Light-emitting Diodes, C. M. Bourget, HortScience, 43, 1944-1946 (2008)

[5] Tuning Optical Properties of GaN-Based Nanostructures by Charge Screening, A. D. Carlo, Phys. Status Solidi A, 183, 81-85 (2001)

[6] Energetic and electronic structure of stacking faults in AlN, GaN, and InN, C. Stampfl, C. G. Walle, Phys. Rev. B, 57, 52-55 (1998); High-pressure properties of wurtzite- and rocksalt-type aluminum nitride, P. E. V. Camp, V. E. V. Doren, J. T. Devreese, Phys. Rev. B, 44, 9055-9059 (1991)

[7] Physical Properties of Several II-V Semiconductors, W. J. Turner, A. S. Fischler, W. E. Reese, Phys. Rev., 121, 759-767 (1961)

[8] Electrical and optical properties of the II-V compounds, W. J. Turner, A. S. Fischler, W. E. Reese, J. Appl. Phys., 32, 2241-2245 (1996)

[9] Semiconducting $A^{II}B^{V}$ compounds, D. N. Nasledov, V. Y. Shevchenko, Phys. Status Solidi A, 15, 9-38 (1973)

[10] Crystal growth, characterization and application of II-V compounds, E. K. Arushanov, Prog. Cryst. Growth Charact., 13, 1-38 (1986)

[11] Two-dimensional wide-band-gap II-V semiconductors with a dilated graphene-like structure, X. J. Zhang, and B. G. Liu, Semicond. Sci. Technol., 31 125002-125008 (2016)

[12] Liquid phase epitaxial growth of II-V semiconductor compound Zn_3As_2, S. Sudhakar, V. Ganesh, I. Sulania, P. K. Kulriya, and K. Baskar, J. Phys. D: Appl. Phys., 40, 5071-5074 (2007)

[13] Electronic structure and chemical bonding of the electron-poor II-V semiconductors ZnSb and ZnAs, D. Benson, O. F. Sankey, and U. Häussermann, Phys. Rev. B, 84, 125211-125219 (2011)

[14] Synthesis, Structure, and Properties of the Electron-Poor II−V Semiconductor ZnAs, A. Fischer, D. Eklöf, D. E. Benson, Y. Wu, E. W. Scheidt, W. Scherer, and U. Häussermann, Inorg. Chem., 53, 8691−8699 (2014)

[15] Transport properties of the II-V semiconductor ZnSb, D. Eklöf, A. Fischer, Y. Wu, E. W. Scheidt, W. Scherer, and U. Häussermann, J. Mater. Chem. A, 1, 1407-1414 (2013)

[16] Inorganic Chemistry (3rd ed.), C. E. Housecroft, and A. G. Sharpe, Prentice Hall, pp. 305-306 (2008)

[17] Top ten of everything 2006, A. Russell, DK Publishing, pp.10 (2005)

[18] Nature's Building Blocks: An A-Z Guide to the Elements, J. Emsley, Oxford University Press, pp. 499-505 (2001)

[19] Über die Kristallstrukturen von Zn_3N_2, Cd_3N_2 und Ge_3N_4. Metallamide and Metallnitride. IX. Mitteilung, R. Juza, H. Hahn, Z., Anorg. Allg. Chem., 224, 125-133 (1940)

[20] The Crystal Structure of Mg_3N_2 and Zn_3N_2, D. E. Partin, D. J. Williams, M. O'Keeffe, J. Solid State Chem., 132, 56-59 (1997)

[21] Optical band gap of Zn_3N_2 films, K. Kuriyama, Yukimi Takahashi, F. Sunohara, Phys. Rev. B, 48, 2781–2782 (1993)

[22] Optical properties of Zinc oxynitride thin films, M. Futsuhara, K. Yoshioka, and O. Takai, Thin Solid Films, 317, 322-325 (1998)

[23] Optical properties and electrical characterization of *p*-type ZnO thin films prepared by thermally oxiding Zn_3N_2 thin films, B. S. Li, Y. C. Liu, Z. Z. Zhi, R. X. Mu and D. O. Henderson, J. Mater. Res., 18, 8-13 (2003)

[24] *p*-type ZnO thin films prepared by Zn_3N_2 thin films deposited by DC magnetron sputtering, C. Wang, Z. Ji, K. Liu, Y. Xiang, and Z. Ye, J. Cryst. Growth, 259, 279-281(2003)

[25] Preparation of metal nitride and oxide thin films using shielded reactive vacuum arc deposition, R. Miyano, K. Kimura, K. Izumi, H. Takikawa, and T. Sakakibara, Vacuum, 59, 159-167 (2000)

[26] Formation and control of zinc nitride in a molten LiCl-KCl-Li_3N system, T. Goto, K. Toyoura, H. Tsujimura, and Y. Ito, Mater. Sci. Eng. A, 380, 41-45 (2004)

[27] MOCVD of the Cubic Zinc Nitride Phase, Zn_3N_2, Using $Zn[N(SiMe_3)_2]_2$ and Ammonia as Precursors, E. Maile, and R. A. Fischer, Chem. Vap. Deposition, 11, 409-414 (2005)

[28] Band-gap energy and electron effective mass of polycrystalline Zn_3N_2, T. Suda, and K. Kakishita, J. Appl. Phys., 99, 076101-1-076101-3 (2006)

[29] Electrical characterization of *p*-type N-doped ZnO films prepared by thermal oxidation of sputtered Zn_3N_2 films, Y. Nakano, T. Morikawa, T. Ohwaki, and Y. Taga, Appl. Phys. Lett., 88, 172103-172103-3 (2006)

[30] (111)-oriented Zn_3N_2 growth on A-plane sapphire substrates by molecular beam epitaxy, T. Oshima and S. Fujita, Jpn. J. Appl. Phys., 45, 8653-8655 (2006)

[31] *p*-type N-doped ZnO: fabrication and characterization, E. Kaminska, A. Piotrowska, J. Kossut, R. Butkute, W. Dobrowolski, R. Lukasiewicz, A. Barcz, R. Jakiela, E. Dynowska, E. Przezdziecka, M. Aleszkiewicz, P. Wojnar, and E. Kowalczyk, Phys. Status Solidi C, 2, 1119-1124 (2005)

[32] The Electrochemistry of Zn_3N_2 and LiZnN: A lithium Reaction Mechanism for Metal Nitride Electrodes, N. Pereira, L. C. Klein, G. G. Amatucci, J. Electrochem. Soc., 149, A262-A271 (2002)

[33] Neutral molecular ZnX (X=O, OH, N) compounds in a molecular beam, D. Cannavo, G. Knopp, P. Radi, P. Beaud, M. Julej, P. Bodek, T. Gerber, and A. Wokaun, J. Mol. Struct., 782, 67-72 (2006)

[34] Optical prosperities of zinc nitride formed by molten salt electrochemical process, K. Toyoura, H. Tsujimura, T. Goto, K. Hachiya, R. Hagiwara, Y. Ito, Thin Solid Films, 492, 88-92 (2005)

[35] Zinc nitride thin films: basic properties and applications, A. R. Cubero, M. G. Castaño, C. G. Núñez, M. Domínguez, L. Vázquez, and J. L. Pau, Proc. SPIE, 10105, 101051B.1-101051.6 (2017)

[36] Synthesis of cubic boron nitride using Mg and pure M'-doped Li_3N, Ca_3N_2 and Mg_3N_2 with M'=Al, B, Si, Ti, G. Bocquillon, C. Loriers-Susse, and J. Loriers, J. Mater. Sci., 28, 3547-3556 (1993)

[37] Preparation of Magnesium Nitride Powder by low-Pressure Chemical Vapor Deposition, T. Murata, K. Itatani, F. S. Howell, A. Kishioka, and M. Kinoshita, J. Am. Ceram. Soc., 76, 2909-2911 (1993)

[38] Uniform MgO nanobelts formed from in situ Mg_3N_2 precursor, R. Ma, and Y. Bando, Chem. Phys. Lett., 370, 770-773 (2003)

[39] Solid state metathesis routes to Group IIIa nitrides: comparison of Li_3N, NaN_3, Ca_3N_2 and Mg_3N_2 as nitriding agents, I. P. Parkin, and A. M. Nartowski, Polyhedron, 17, 2617-2622 (1998)

[40] Design of shallow acceptors in ZnO: First-principles band-structure calculations, J. Li, S. H. Wei, S. S. Li, J. B. Xia, Phys. Rev. B, 74, 081201-081201-4 (2006)

[41] Synthesis of AlN/Al Alloy Composites by in situ Reaction between Mg_3N_2 and Aluminum, M. Kobashi, N. Okayama, and T. Choh, Mater. Trans., JIM, 38, 260-265 (1997)

[42] In situ synthesis of AlN particles in Mg-Al alloy by Mg_3N_2 addition, H. Z. Ye, X. Y. Liu, B. Luan, Mater. Lett., 58, 2361-2364 (2004)

[43] Theoretical investigation of the high-pressure structure, phase transition, and mechanical and electronic properties of Mg_3N_2, J. Li, C. Z. Fan, X. Dong, Y. Jin, and J. L. He, J. Phys. Chem. C, 118, 10238−10247 (2014)

[44] Hydrogen storage in nanostructure with physisorption, K. Bradley, P. G. Collins, J. C. P. Gabriel, Y. Kwon, S. Jhi, and G. Gruner, Patent US6672077, Nanomix Inc., (2003)

[45] Reversible hydrogen-storage functions for mixtures of Li_3N and Mg_3N_2, Y. Nakamori, G. Kitahara, K. Miwa, S. Towata, and S. Orimo, Appl. Phys. A: Mater. Sci. Process., 80, 1-3 (2005)

[46] Mechanism of Hydrogenation Reaction in the Li-Mg-N-H system, H. Leng, T. Ichikawa, S. Hino, T. Nakagawa, and H. Fujii, J. Phys. Chem. B, 109, 10744-10748 (2005)

[47] Recent development on hydrogen storage properties in metal-N-H systems, T. Ichikawa, H. Y. Lengs, S. Isobe, N. Hanada, and H. Fujii, J. Power Sources, 159, 126-131 (2006)

[48] Hydrogen storage of metal nitrides by a mechanochemical reaction, Y. Kojima, Y. Kawai, and N. Ohba, J. Power Sources, 159, 81-87 (2006)

[49] Light metal hydrides- Potential hydrogen storage materials, H. Woolf, I. Brown, M. Bowden, Curr. Appl. Phys., 8, 459-462 (2008)

[50] Effect of Al-based additives on the hydrogen storage performance of the $Mg(NH_2)_2$-2LiH system, H. Cao, Y. Zhang, J. Wang, Z. Xiong, G. Wu, J. Qiu, and P. Chen, Dalton Trans., 42, 5524-5531 (2013)

[51] A process for synthesizing the Li-Mg-N-H hydrogen storage system from Mg an $LiNH_2$, K. Okamotoa, K. Tokoyoda, T. Ichikawa, and H. Fujii, J. Alloys Compd., 432, 289-292 (2007)

[52] Superior hydrogen desorption kinetics of $Mg(NH_2)_2$ hollow nanospheres mixed with MgH_2 nanoparticles, L. Xie, Y. Li, R, Yang, Y. Liu, and X. Li, Appl. Phys. Lett., 92, 231910.1-231910.3 (2008)

[53] The vibrational spectra and decomposition of α-calcium nitride and magnesium nitride, A. M. Heyns, L. C. Prinsloo, K. J. Range, M. Stassen, J. Solid State Chem., 137, 33-41 (1998)

[54] Ab-initio band structure calculation of Mg_3N_2 and $MgSiN_2$, C. M. Fang, R. A. de Groot, R. J. Bruls, H. T. Hintzen, and G. de With, J. Phys.: Condens. Matter, 11, 4833-4842 (1999)

[55] Binary nitrides α-M_3N_2 (M=Be, Mg, Ca): a theoretical study, E. Orhan, S. Jobic, R. Brec, R. Marchand, and J. Y. Saillard, J. Mater. Chem., 12, 2475-2479 (2002)

[56] Structural and optical properties of magnesium nitride formed by a novel electrochemical process, K. Toyoura, T. Goto, K. Hachiya, and R. Hagiwara, Electrochim. Acta, 51 56-60 (2005)

[57] Carbon Nanotubes as Nanoreactors for Fabrication of Single-Crystalline Mg_3N_2 nanowires, J. Hu, Y. Bando, J. Zhan, C.Zhi, and D. Golberg, Nano Lett., 6, 1136-1140 (2006)

[58] Excitonic and Defect-Related Photoluminescence in Mg_3N_2, Y. Uenaka, and T, Uchino, J. Phys. Chem. C, 118, 11895-11901 (2014)

[59] Mg_3N_2-Ga: Nanoscale Semiconductor-Liquid Metal heterojunctions inside Graphitic Carbo Nanotubes, J. Hu, Y. Bando, J. Zhan, C. Li, and D. Golberg, Adv. Mater., 19, 1342-1346 (2007)

[60] Band structure features, chemical bonding and optical properties of Zn_3X_2 (X=N, P, As) compounds, M. Ullah, G. Murtaza, M. Yaseen, and S. A. Khan, J. Alloy. Compd., 728, 1226-1234 (2017)

[61] Structural, electronic, optical and thermoelectric properties of Mg_3X_2 (X = N, P, As, Sb, Bi) compounds, M. Ullah, G, Murtaza, S. M. Ramay, and A. Mahmood, Mater. Res. Bull., 91, 22-30 (2017).

[62] Detailed Balance limit of efficiency of p-n Junction Solar Cells, W. Shockley, and H. J. Queisser, J. Appl. Phys., 32, 510-519 (1961)

[63] Photoelectrochemical Cells, M. Grätzel, Nature, 414, 338-344 (2001)

[64] 27.6% conversion efficiency, a new record for single-junction solar cells under 1 sun illumination, B. M. Kayes, H. Nie, R. Twist, S. G. Spruytte, F. Reinhardt, I. C. Kizilyalli, G. S. Higashi, in Proc. of the 37th IEEE Photovoltaic Specialists Conference 000004-000008 (2011)

[65] Solar cell efficiency tables (version 50), M. A. Green, Y. Hishikawa, W. Warta, E. D. Dunlop, D. H. Levi, J. Hohl-Ebinger, A. W. H. Ho-Baillie, Prog. Photovoltaics, 25, 668-676 (2017)

[66] Band bowing and band alignment in InGaN alloys, P. G. Moses, C. G. Van de Walle, Appl. Phys. Lett., 96, 021908.1-021908.3 (2010)

[67] Carrier-Induced Band-Gap Variation and Point Defects in Zn_3N_2 from First Principles, Y. Kumagai, K. Harada, H. Akamatsu, K. Matsuzaki, F. Oba, Phys. Rev. Appl., 8, 014015.1-014015.12 (2017)

[68] Band-gap energy and electron effective mass of polycrystalline Zn_3N_2, T. Suda, K. Kakishita, J. Appl. Phys., 99, 07610.1-07610.3 (2006)

[69] Transparent Conducting Zinc Nitride films, N. Yamada, K. Watarai, T. Yamaguchi, A. Sato, Y. Ninomiya, Jpn. J. Appl. Phys., 53, 05FX01.1-05FX01.5 (2014)

[70] Optical band gap of the Zn_3N_2 films, K. Kuriyama, Y. Takahashi, F. Sunohara, Phys. Rev. B., 48, 2781-2782 (1993)

[71] RF- plasma assisted PLD growth of Zn_3N_2 thin films, R. Ayouchi, C. Casteleiro, L. Santos, and R. Schwarz, Phys. Status Solidi C., 7, 2294-2297 (2010)

[72] Structural properties and photoluminescence of zinc nitride nanowires, F. J. Zong, H. L. Ma, J. Ma, W. Du, X. J. Zhang, H. D. Xiao, F. Ji, C. S. Xue, Appl. Phys. Lett., 87, 233104.1- 233104.3 (2005)

[73] Atomic layer deposition of textured zinc nitride thin films, S. Sinha, S. K. Sarkar, RSC Adv., 4, 47177-47183 (2014)

[74] Structural, electrical and optical properties of zinc nitride thin films prepared by reactive rf magnetron sputtering, M. Futsuhara, K. Yoshioka, O. Takai, Thin Solid Films., 322, 274-281 (1998)

[75] Structural and optical properties of zinc nitride films prepared by rf magnetron sputtering, T. L. Yang, Z. S. Zhang, Y. H. Li, M. S. Lv, S. M. Song, Z. C. Wu, J. C. Yan, S. H. Han, Appl. Surf. Sci., 255, 3544-3547 (2009)

[76] Zinc nitride films prepared by reactive RF magnetron sputtering of Zinc in nitrogen containing atmosphere, N. K. Jiang, D. G. Georgiev, A. H. Jayatissa, R. W. Collins, J. Chen, E. McCullen, J. Phys. D: Appl. Phys., 45 135101.1-135101.9 (2012)

[77] On the zinc nitride properties and the unintentional incorporation of oxygen, C. G. Núñez, J. L. Pau, M. J. Hernández, M. Cervera, E. Ruiz, J. Piqueras, Thin Solid Films., 520, 1924-1929 (2012)

[78] Oxygen -doped zinc nitride as a high-mobility nitride-based semiconductor, X. Cao, A. Sato, Y. Ninomiya, N. Yamada, J. Phys. Chem. C, 119, 5327-5333 (2015)

[79] Structural, electrical, and optical characterization of as grown and oxidized zinc nitride thin films, A. Trapalis, J. Heffernan, I. Farrer, J. Sharman, A. Kean, J. Appl. Phys., 120, 205102.1-205102.9 (2016)

[80] Comparative study of electron transport mechanisms in epitaxial and polycrystalline zinc nitride films, X. Cao, Y. Yamaguchi, Y. Ninomiya, N. Yamada, J. Appl. Phys., 119, 025104.1-025104.11 (2016)

[81] Zinc nitride as a potential high mobility transparent conductor, X. Cao, Y. Ninomiya, N. Yamada, Phys. Status Solidi A, 214, 1600472.1-1600472.7 (2017)

[82] Transparent and conductive impurity-doped GaN thin films prepared by an electron cyclotron resonance plasma metalorganic chemical vapor deposition method, H. Sato, T. Minami, E. Yamada, M. Ishii, S. Takata, J. Appl. Phys., 75, 1405-1409 (1994)

[83] Low-Temperature Solution-Processed Flexible Solar Cells Based on (In,Ga)N Nanocubes, M. A. Qaeed, K. Ibrahim, K. M. A. Saron, M. A. Ahmed, N. K. Allam, ACS Appl. Mater. Interfaces, 6, 9925-9931 (2014)

[84] Widening of optical bandgap of polycrystalline InN with a few percent incorporation of oxygen, M. Yoshimoto, H. Yamamoto, W. Huang, H. Harima, J. Saraie, A. Chayahara, and Y. Horino, Appl. Phys. Lett., 83, 3480-3482 (2003)

[85] Excitonic and defected -related photoluminescence in Mg_3N_2, Y. Unekata, T. Uchino, J. Phys. Chem. C, 116, 11895-11901 (2014)

[86] Ca_3N_2 and Mg_3N_2: unpredicted high-pressure behavior of binary nitrides, C. Braun, S. L. Börger, T. D. Boyko, G. Miehe, H. Ehrenberg, P. Höhn, A. Moewes, W. Schnick, J. Am. Chem. Soc., 133, 4307-4315 (2011)

[87] III-nitrides for energy production: photovoltaic and thermoelectric applications, N. Lu, I. Ferguson, Semicond. Sci. Technol., 28, 074023.1-074021.11 (2013)

[88] N doping and Al-N co-doping in sol-gel ZnO films: studies of their structural, optical, and photoconductive properties, M. Dutta, T. Ghosh, and D. Basak, J. Elect. Mater., 38, 2335-2342 (2009)

[89] Pulsed laser ablation of zinc selenide in nitrogen ambience: Formation of zinc nitride films, S. Simi, I. Navas, R. Vinodkumar, S. R. Chalana, M. Gangrade, V. Ganesan, V. P. M. Pillai, Appl. Surf. Sci., 9269-9276 (2011)

[90] RF-plasma assisted PLD growth of Zn_3N_2 thin films, R. Ayouchi, C. Casteleiro, L. Santos, R. Schwarz, Phys. Status Solidi C, 7, 2294-2297 (2001)

[91] Structure and optical constants of electron beam deposition zinc nitride films, H. A. Mohamed, Eur. Phys. J. Appl. Phys., 48, 20504.1-20504.6 (2009)

[92] Comprehensive semiconductor science and technology, P. Frigeri, L. Seravalli, G. Trevisi, and S. Franchi, Elsevier, pp.481 (2011)

[93] Molecular beam epitaxy: fundamentals and current status, M. A. Herman, and H, Sitter, Springer Series in Material Science, 7 (1989)

[94] Nitrogen-plasma study for plasma-assisted MBE growth of 1.3 μm laser diodes, H. Carrere, A. Arnoult, A. Ricard, X. Marie, T. Amand, E. B. Pereira, Solid-State Electron., 47, 419-423 (2003)

[95] Nitride-based laser diodes by plasma-assisted MBE-from violet to green emission, C. Skierbiszewski, Z. R. Wasilewski, I. Grzegory, and S. Porowski, J. Cryst. Growth, 311, 1632-1639 (2009)

[96] The reinterpretation of wave mechanics, L. de Broglie, Found. Phys., 1, 5-15 (1970)

[97] Optical properties of Thin Solid Films, O. S. Heavens, London: Butterworth, pp 46-48, (1955)

[98] Spectral reflectance and transmittance prediction model for stacked transparency and paper both printed with halftone colors, J. Machizaud, and M. Hébert. J. Opt. Soc. Am., 29, 1537-1548 (2012)

[99] The effect of oxygen ratio on the crystallography and optical emission properties of reactive RF sputtered ZnO films, N. H. A. Hardan, M. J. Abdullah, A. A. Aziz, H. Ahmad, M. Rashid, Physica B Condens Matter., 405, 1081-1085 (2010)

[100] Molecular Beam Epitaxy: An Overview Comprehensive Semiconductor Science and Technology, P. Frigeri, L. Seravalli, G. Trevisi, and S. Franchi, Elsevier, 3, 484-485 (2011)

[101] Tables of Physical & Chemical Constants (16^{th} ed.), IUPAC (1991) Pure & Appl. Chem., 63, 976–1002. IUPAC (1992) Pure & Appl. Chem., 64, 1519–1534.

[102] Principles of physical vapor deposition of thin films, K. S. S. Harsha. Elsevier, pp. 400 (2006)

[103] Magnetron sputtering, S. Swann, Physics in Technology,19, 67-75 (1988)

[104] A quasi-direct-current sputtering technique for the deposition of dielectrics at enhanced rates, G. Estes, W. D. Westwood, J. Vac. Sci. Technol. A, 6. 1845-1848 (1988)

[105] Surface morphology of *c*-plane sapphire produced by high temperature anneal, F. Cuccureddu, S. Murphy, I. V. Shvets, M. Porcu, H. W. Zandbergen, N. S. Sidorov, S. I. Bozhko, Surf. Sci., 604, 1294-1299 (2010)

[106] Elements of X-ray diffraction (2^{nd} ed.), B. D. Cullity. Addison-Wesley, pp.84 (1978)

[107] X-ray diffraction of multilayers and superlattices, W. J. Bartels, J. Hornstra, D. J. W. Lobeek, Acta Cryst., 42, 539-545 (1986)

[108] X-ray diffraction of III-nitrides, M. A. Moram, and M. E. Vickers, Rep. Prog. Phys., 72, 036502-036546 (2009)

[109] High resolution x-ray scattering: from thin films to lateral nanostructures, U. Pietsch, V. Holy, and T. Baumbach, Springer, pp 63-74 (2004)

[110] Employing theories far beyond their limits-the case of the (Boguer-) Beer–Lambert law, G. T. Mayerhçfer, H. Mutschke, and J. Popp, ChemPhysChem, 17, 1948-1955 (2016)

[111] Atkins' physical chemistry, P. Atkins, J. de Paula, Oxford University Press, pp 103-109 (2014)

[112] Physical chemistry, T. Engel, P. J. Reid, W. Hehre, Pearson, pp. 780-791 (2013)

[113] Absorbance, absorption coefficient, and apparent quantum yield: A comment on common ambiguity in the use of these optical concepts, C. Hu, E. F. Muller-Karger, and R. G. Zepp. Limnol. Oceanogr., 47, 1261-1267 (2002)

[114] Fundamentals of semiconductors, M. Cardona, and P. Yu, Springer, 127-138 (2010)

[115] Optical properties and electronic structure of amorphous germanium, J. Tauc, R. Grigorovici, and A. Vancu, Phys. Status Solidi, 15, 627-637 (1966)

[116] Evaluation of the Tauc method for optical absorption edge determination: ZnO thin films as a model system, B. D. Viezbicke, S. Patel, B. E. Davis, and D. P. Birnie, Phys. Status Solidi B, 252, 1700-1710 (2015)

[117] Morphological, optical and DC conduction properties of GaSe semiconductor nanoparticle thin films, S. Kumar, M. A. Khan, J. Mater. Sci. Tech., 29, 1151-1155 (2013); Analysis of bandgap energy and refractive index of ferroelectric perovskite pbbatio, V. S. Vinila, J. Isac, Int. J. Eng. Sci. Invention, 7, 40-47 (2018)

[118] Fundamentals of semiconductor laser, T. Numai, Springer, pp. 23-40 (2015)

[119] Ellipsometry of functional organic surfaces and films, K. Hinrichs, K. J. Eichhorn, Springer, pp.15-16 (2014)

[120] Handbook of ellipsometry, H. G. Tompkins, E. A. Irene, William Andrew and Springer, pp. 161-163 (2005)

[121] Handbook of optical constants of solids, D. E. Aspnes, Academic Press, pp. 89-112 (1985)

[122] A method of measuring specific resistivity and Hall effect of discs of arbitrary shape, L. J. van der Pauw, Philips Res. Rep., 13, 1-9 (1958)

[123] A method of measuring specific resistivity and Hall coefficient on lamellae of arbitrary shape, L. J. van der Pauw, Philips Res. Rep., 20, 220-224 (1958)

[124] https://web.archive.org/web/20060525032823/http://www.eeel.nist.gov/812/meas.htm#defh

[125] Quantitative surface analysis by XPS: application to hydrotreating catalysts, P. Beccat, P. D. Silva, Y. Huiban, and S. Kasztelan, Oil & Gas Sci. Technol.-Rev. IFP, 54, 487-496 (1999)

[126] Handbook of X-ray photoelectron spectroscopy, L. E. Davis, C. D. Wagner, W. M. Riggd, and J. F. Moulder, Perkin Elmer, pp. 33-194 (1978)

[127] Empirical analysis atomic sensitivity factors for quantitative analysis by electron spectroscopy for chemical, C. D. Wagner, L. E. Davis, M. V. Zeller, J. A. Taylor, R. M. Raymond and L. H. Gale, Surf. Interface Anal., 3, 211-225 (1981)

[128] On the true optical properties of zinc nitride, C. G. Núñez, J. L. Pau, J. Hernandez, M. Cervera, and J. Piqueras, Appl. Phys. Lett., 99, 232112.1-232112.3 (2011)

[129] Effect of oxidation on the optical properties of Zn_3N_2 powders, Helaleh Alimohammadi, M.Sc thesis, University of Victoria (2017)

[130] Structural, electrical, and optical characterization of as grown and oxidized zinc nitride thin films, A. Trapalis, J. Heffernan, I. Farrer, J. Sharman, and A. Kean, J. Appl. Phys., 120, 205102.1- 205102.9 (2016)

[131] Zinc nitride films prepared by reactive RF magnetron sputtering of zinc in nitrogen containing atmosphere, N. Jiang, D. G. Georgiev, A. H. Jayatissa, R. W.

Collins, J. Chen, and E. McCullen, J. Phys. D: Appl. Phys., 45, 135101-135110 (2012)

[132] Zinc nitride as a potential high-mobility transparent conductor, X. Cao, Y. Ninomiya, and N. Yamada, Phys. Status Solidi A, 214, 1600472.1-1600472.7 (2017)

[133] Growth pressure-temperature region of cubic BN in the system BN-Mg, T. Endo, O. Fukunaga, M. Iwata, J. Mat. Sci., 14, 1375-1380 (1979)

[134] Precipitation mechanism of BN in the ternary system B-Mg-N, T. Endo, O. Fukunaga, M. Iwata, J. Mat. Sci., 14, 1676-1680 (1979)

[135] Preparation of magnesium nitride powder by low-pressure chemical vapor deposition, T. Murata, K. Itatani, F. Howell, A. Kishaoka, and A. Kinoshata, J. Am. Ceram. Soc., 76, 2909-2911 (1993)

[136] About binary and ternary alkaline earth metal nitrides, O. Reckeweg, and F. DiSalvo, Z. Anorg. Allg. Chem., 627, 371-377 (2001)

[137] Structural and optical properties of magnesium nitride formed by a novel electrochemical process, K. Toyoura, T. Goto, K. Hachiya, and R. Hagiwara, Electrochimica Acta, 51, 56-60 (2005)

[138] Excitonic and defect-related photoluminescence in Mg_3N_2, Y. Uenaka, and T. Uchino, J. Phys. Chem. C, 118, 11895-11901 (2014)

[139] Calculation of atomic scattering factors using Slater wave function: sodium to calcium, Y. Tomiie, and C. H. Stam, Acta Cryst. 11, 126-127 (1958)

[140] In international table for crystallography (Vol. C (Ed. E. Prince)), P. J. Brown, A. G. Fox, E. N. Maslen, M. A. O'Keefe, B. T. M. Willis, Wiley, p. 578 (2006)

[141] Ab-initio band structure calculation of Mg_3N_2 and $MgSiN_2$, C. M. Fang, R. A. de Groot, R. J. Bruls, H. T. Hintzen, and G. de With, J. Phys.: Condens. Matter, 11, 4833-4842 (1999)

[142] Binary nitride α-M_3N_2 (M=Be, Mg, Ca): a theoretical study, E. Orhan, S. Jobic, R. Brec, R. Marchand, and J. Y. Saillard, J. Mater. Chem., 12, 2475-2479 (2002)

[143] Theoretical Investigation of the High-Pressure Structure, Phase Transition, and Mechanical and Electronic Properties of Mg_3N_2, J. Li, C. Fan, X. Dong, Y. Jin, and J. He, J. Phys. Chem. C, 118, 10238-10247 (2014)

[144] Structural Phase Transformations of Mg_3N_2 at High Pressure: Experimental and Theoretical Studies, J. Hao, Y. Li, Q. Zhou, D. Liu, M. Li, F. Li, W. Lei, X. Chen, Y. Ma, Q. Cui, G. Zou, J. Liu, and X. Li, Inorg. Chem., 48, 9737-9741 (2009)

Appendix A: X-ray Atomic Scattering Factor

The X-ray atomic scattering factor is a function of $\sin\theta / \lambda$, i.e. $f(\sin\theta / \lambda)$, where θ and λ denote the incident angle and X-ray wavelength, respectively. In general, $f(\sin\theta / \lambda)$ is approximated by the following polynomial expression: [138]

$$f\left(\frac{\sin\theta}{\lambda}\right) = \sum_{i=1}^{4} a_i \exp\left(-\frac{b_i \sin^2\theta}{\lambda^2}\right) + c, \quad \text{(A1)}$$

where a_i, b_i, and c are constants depending on the atomic species. The values of a_i, b_i, and c for Zn and Mg are listed in literature.

We calculated $f(\sin\theta / \lambda)$ values for Zn(II) and Mg(II) using the values of a_i, b_i, c and λ = 1.5418Å (CuKα). Figure a1 shows the relationship between f $f(\sin\theta / \lambda)$ and θ. From these calculations, f = 19 and f = 7.0 were obtained for Zn(II) and Mg(II), respectively, at θ = 20º.

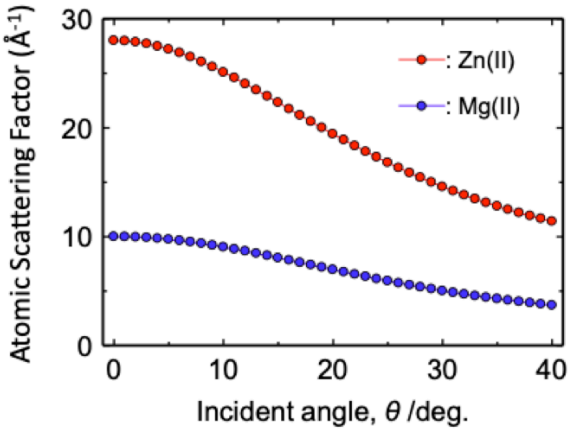

Figure A1. Atomic scattering factors of Zn(II) and Mg(II) as functions of incident angle θ.